

20000920249

(12)

SECURITY CLASSIFICATION OF T

REPORT DC

AD-A262 421

READ INSTRUCTIONS  
BEFORE COMPLETING FORM

1. REPORT NUMBER

GRL/9201



RECIPIENT'S CATALOG NUMBER

4. TITLE (and Subtitle)

PROOF OF THE FEASIBILITY OF  
COHERENT AND INCOHERENT SCHEMES  
FOR PUMPING A GAMMA-RAY LASER

TYPE OF REPORT &amp; PERIOD COVERED

Annual Letter Report  
12/24/91 - 12/23/92

6. PERFORMING ORG. REPORT NUMBER

7. AUTHOR(s)

C. B. Collins

8. CONTRACT OR GRANT NUMBER(s)

N00014-90-K-2001

9. PERFORMING ORGANIZATION NAME AND ADDRESS

University of Texas at Dallas  
Center for Quantum Electronics  
P. O. Box 830688  
Richardson, TX 75083-068810. PROGRAM ELEMENT, PROJECT, TASK  
AREA & WORK UNIT NUMBERS

11. CONTROLLING OFFICE NAME AND ADDRESS

INNOVATIVE SCIENCE AND TECHNOLOGY DIRECTORATE  
OF STRATEGIC DEFENSE INITIATIVE ORGANIZATION

12. REPORT DATE

12/31/92

13. NUMBER OF PAGES

166

14. MONITORING AGENCY NAME &amp; ADDRESS (if different from Controlling Office)

Dr. Paul Kepple  
Naval Research Laboratory  
4555 Overlook Ave., S.W.  
Washington, D. C. 20375-5000  
Attn: Code 4720

15. SECURITY CLASS. (of this report)

Unclassified

15a. DECLASSIFICATION/DOWNGRADING  
SCHEDULE

16. DISTRIBUTION STATEMENT (of this Report)

This document has been approved for public release and sale;  
its distribution is unlimited.

17. DISTRIBUTION STATEMENT (of the abstract entered in Block 20, if different from Report)

DTIC  
ELECTE  
MAR 12 1993  
S C D

18. SUPPLEMENTARY NOTES

19. KEY WORDS (Continue on reverse side if necessary and identify by block number)

Gamma-ray laser, Ultrashort wavelength laser

419801  
93-05201  
16688

20. ABSTRACT (Continue on reverse side if necessary and identify by block number)

The most productive approaches to the problem of the gamma-ray laser have focused upon upconversion techniques in which metastable nuclei are pumped with long wavelength radiation. At the nuclear level the storage of energy can approach tera-Joules ( $10^{12}$ J) per liter for thousands of years. However, any plan to use such a resource for a gamma-ray laser poses problems of a broad interdisciplinary nature requiring the fusion of concepts taken from relatively unrelated fields of physics. Our research group has described

(continued on next page)

DD FORM 1 JAN 75 1473

EDITION OF 1 NOV 68 IS OBSOLETE  
S/N 0102-LF-014-6601

SECURITY CLASSIFICATION OF THIS PAGE (When Data Entered)

Reproduced From  
Best Available Copy

98 3 11 036

## 20. Abstract (continued)

several means through which this energy might be coupled to radiation fields with cross sections for stimulated emission that could reach  $10^{-17}$  cm<sup>2</sup>. Such a stimulated release could lead to output powers as great as  $3 \times 10^{21}$  Watts/liter. Since 1978 we have pursued an approach for the upconversion of longer wavelength radiation incident upon isomeric nuclear populations that can avoid many of the difficulties encountered with traditional concepts of single photon pumping. Experiments have confirmed the general theory and have indicated that a gamma-ray laser is feasible if the right combination of energy levels and branching ratios exists in some real material. Of the 1,886 distinguishable nuclear materials, the present state-of-the-art has been adequate to identify 29 first-class candidates, but further evaluation cannot proceed without remeasurements of nuclear properties with higher precision. A laser-grade database of nuclear properties does not yet exist, but the techniques for constructing one have been developed and utilized under this contract. Resolution of the question of the feasibility of a gamma-ray laser now rests upon the determination of: 1) the identity of the best candidate, 2) the threshold level of laser output, and 3) the upconversion driver for that material.

This annual report focuses upon our approach that is the nuclear analog to the ruby laser. It embodies the simplest concepts for a gamma-ray laser and not surprisingly, the greatest rate of achievement in the quest for a subAngstrom laser was realized in that direction. For ruby the identification and exploitation of a bandwidth funnel were the critical keys in the development of the first laser. There was a broad absorption band linked through efficient cascading to the narrow laser level.

In 1987 we reported a major milestone which showed that comparable structure existed at the nuclear scale in the first of the 29 candidate isomers available for testing, <sup>180</sup>Ta<sup>m</sup>. Populations of the isomer were successfully pumped down with flashes of x-rays absorbed through an astonishingly large cross section of 40,000 on the usual scale ( $10^{-29}$  cm<sup>2</sup> keV) where 10 describes a fully allowed process. This corresponded to a partial width for useful absorption of 0.5 eV, even better than what had been assumed for idealized nuclei. Subsequently, we discovered that the giant pumping resonances occurred with a gratifying frequency throughout the table of nuclides, reaching optimal size and strength in the mass region where the better candidates lie. Nineteen isomers were successfully pumped with the bremsstrahlung from both a 4 MeV linac and a 6 MeV linac. The giant resonances for pumping the candidate isomers <sup>180</sup>Ta<sup>m</sup> and <sup>123</sup>Te<sup>m</sup> were found to open at gateway energies well below 4 MeV. These candidates have the largest integrated cross sections for pumping with x-rays ever found below 4 MeV in any nuclei. These two poorest of the 29 candidates are the only ones available for testing and they continue to outperform even the most optimistic expectations. The likelihood for the full feasibility of one of the better candidates continues to be raised by the successes enjoyed with the least attractive of the 29 candidates.

During the current reporting we focused upon the extension of these achievements in pumping nuclei to those having laser-like transitions with microsecond lifetimes. For the test cases of Ta-181 and Hf-176 giant resonances were found for the pumping of fluorescence from levels with lifetimes of 18 and 10 microseconds, respectively. Those nuclei were pumped with the Texas-X linear accelerator installed in our facility this year for the dedicated use in gamma ray laser research. The importance of these first results are that the particular nuclei studied are very close neighbors in the sense of nuclear structure to the still unavailable first class candidate nuclei for a gamma ray laser. Such favorable results with these close simulations argue strongly for analogous successes with the actual candidate nuclei.

## PREFACE

At first approach it would seem that the prospects for all ultrashort wavelength lasers would be vitiated by the basic  $\nu^3$  dependence of electron transition probabilities that drastically limits the storage of pump energies. However, there are some unique advantages of a gamma-ray laser that would accrue from its operation upon electromagnetic transitions of nucleons as opposed to electrons. First, the constant linking  $\nu^3$  with lifetime is more favorable by orders-of-magnitude because of the accessibility of a variety of transition moments. For example, nuclear transitions with 100 keV energies can have microsecond lifetimes so the effects pumped by an input pulse can be integrated up to larger values for longer times. Secondly, nuclear metastables store keV and even MeV for years. With upconversion schemes most of the pump power is input long before the time of use and triggering requirements are small. Nuclear transitions need not have thermal broadening and natural linewidths are routinely obtained. Without broadening, electromagnetic cross sections are large and values for  $1\text{ A}$  transitions typically exceed the cross section for the stimulation of Nd in YAG. Finally, working metastables can be concentrated to solid densities. As candidates for ultra short wavelength media, nuclear populations clearly offer some strong advantages.

The clear attractions notwithstanding, a decade ago the difficulties in realizing a gamma-ray laser were considered to be almost insurmountable. However, in 1982 we began to emphasize an interdisciplinary concept of upconversion which ultimately launched a renaissance in the field. The essential concept was the "optical" pumping of nuclei. In this case optical meant x rays, but the fundamentals were the same. Useful, resonant absorption of pump power would occur over short distances to produce high concentrations of excited nuclei while wasted wavelengths would be degraded to heat in much larger volumes. Of all the cases considered, the nuclear analog of the ruby laser embodied the simplest concepts for a gamma-ray laser. Not surprisingly, the greatest rate of achievement has been realized in that direction.

For ruby, the identification and exploitation of a bandwidth funnel were the critical keys in the development of the first laser. There was a broad absorption band linked through efficient cascading to the narrow laser level. Our model called for a nuclear analog of this structure which was unknown in 1986 when the first phase of experiments was started. Now, that theory has been confirmed.

The use of intense flashes of x rays to dump the stored energy of an isomer was first shown in 1988 for the rare nuclide  $^{180}\text{Ta}^m$  which exists naturally as 100% inverted. Then experiments with the unique superconducting linac at Darmstadt showed that populations of the isomer  $^{180}\text{Ta}^m$  are pumped down through two isolated resonances of extraordinary strength, about  $10^6$  times larger than expected for the excitation of nuclei by x rays. Subsequent experiments used four accelerators to survey 19 isotopes for the systematic occurrence of these giant pumping resonances.

Research conducted this past year has been focused upon the extension of the results to systems more nearly resembling actual laser materials. Fluorescent transitions with laser-like lifetimes of microseconds were found to be pumped with the same type of resonances having such extraordinary strengths. This major achievement was the synthesis of efforts to advance instrumentation, with an emphasis upon materials with microsecond lifetimes. The research was made possible by the successful installation of the Texas-X linear accelerator at our facility. Dedicated fully to this work it supported the study of these more difficult nuclei. The details of these achievements are reviewed in the following sections and are followed by preprints and reprints of those aspects selected for publication. Results this past year continue to enhance the feasibility of a gamma ray laser by further reducing demands upon potential pump systems.

## TABLE OF CONTENTS

THE GAMMA-RAY LASER: ISSUES AND PROGRESS IN 1992 . . . . .	1
INSTALLATION OF THE TEXAS-X RESEARCH LINEAR ACCELERATOR . . . . .	37
ABSOLUTE MEASUREMENT OF SPATIAL AND SPECTRAL CHARACTERISTICS OF BREMSSTRAHLUNG BY THE PHOTOEXCITATION OF NUCLEAR ISOMERS: CALIBRATION OF THE TEXAS-X . . . . .	64
AN EVALUATION OF NANOPHASE DIAMOND FILM DOPED WITH $^{57}\text{Fe}$ FOR USE AS A NUCLEAR TARGET . . . . .	94
APPENDIX A	
Reprints and preprints of other manuscripts which were published or submitted for publication during the reporting period . . . . .	111

THIS STATEMENT IS UNCLASSIFIED

Accession For	
NTIS CRA&I	<input checked="" type="checkbox"/>
DTIC TAB	<input type="checkbox"/>
Unannounced	<input type="checkbox"/>
Justification	
By	
Distribution /	
Availability Codes	
Dist	Avail and/or Special
A-1	

## THE GAMMA-RAY LASER: ISSUES AND PROGRESS IN 1992

J. J. Carroll, T. W. Sinor, K. N. Taylor, C. Hong, J. D. Standifird,  
D. G. Richmond, B. W. Johnson and C. B. Collins

### INTRODUCTION

Studies of the feasibility of a gamma-ray laser are readily motivated by the unique advantages presented by nuclear systems. Many nuclei possess exceptionally long-lived excited states called isomers with energies of keV to MeV. Populations of these metastable states can store tera-Joules per liter at solid densities for up to thousands of years so it would not be necessary to provide all the pump energy for a gamma-ray laser in situ. Electromagnetic transitions in nuclei provide a variety of transition moments for which the constant linking spontaneous lifetime with the  $\nu^3$  factor is orders-of-magnitude more favorable than might otherwise be expected for such short wavelengths. Thus lasing levels in nuclei can have lifetimes as long as  $\mu$ s and pump pulses can be integrated for much longer times than are characteristic of x-ray lasers. Another advantage is that gamma-ray transitions routinely have natural linewidths, as seen in Mössbauer spectra, and this would insure large cross sections for stimulated emission. Without broadening, values for 1 A nuclear transitions typically exceed the cross section for the stimulation of Nd in YAG.

Despite such a substantial impetus provided by the fundamental considerations, there was little real progress towards a gamma-ray laser before 1982. This was because traditional approaches were concentrated upon pumping nuclei with intense particle fluxes and then suddenly assembling a critical density to reach the threshold for stimulated emission. After a decade of study in the 1970's, the general impossibility of those brute force, single (output) photon

schemes was finally attributed to the unmanageable amounts of heat incidentally deposited in the host matrix as discussed in the encyclopedic review of Baldwin, et al.<sup>1</sup> That work marked the end of the traditional approaches to a gamma-ray laser and demonstrated that the critical test for any new scheme must be the efficacy of pumping to release the energy stored in isomers.

A new interdisciplinary approach<sup>2</sup> to a gamma-ray laser emerged in 1982 following precursive work<sup>3-10</sup> that appeared near the end of the first cycle of research. The basic plan<sup>11,12</sup> called for the "optical" pumping of nuclei using coherent or incoherent processes. Either multiphoton processes or multiple electromagnetic transitions would be used to release the energy stored in nuclear isomers while avoiding many of the problems encountered by the traditional approaches. In the most straightforward application,<sup>2</sup> incoherent pumping simply represented a nuclear analog to the ruby laser in which "optical" referred to x rays. A way was also indicated by which to manage wasted pump energy using a thin film of low Z material as a host matrix.

Driven by this blueprint for a gamma-ray laser which now appears in the textbooks,<sup>13</sup> in the past decade the main line project at the Center for Quantum Electronics has been rich with achievement. The fundamental concepts of coherent pumping have been demonstrated<sup>14-18</sup> but not surprisingly the greatest rate of progress has been realized in the simpler direction of incoherent pumping.<sup>19-29</sup> In fact the feasibility of a gamma-ray laser has been increased orders-of-magnitude by major breakthroughs in the pumping of nuclear isomers with bremsstrahlung.

At the present the most significant impediment to study of the feasibility of a gamma-ray laser continues to be the lack of suitable materials. Of the 1886 distinguishable isotopes,<sup>30,31</sup> 29 have been identified as first class candidates, but only the two poorest, <sup>180</sup>Ta and <sup>123</sup>Te were available in sufficient amounts for testing. Still the discovery of giant pumping resonances for these nuclides<sup>23-25</sup> and others<sup>26-28</sup> greatly strengthened the feasibility. It is upon such pumping

processes that the realization of a gamma-ray laser depends, rather than on refinements like superradiance which may simply serve to reduce threshold requirements.

In the absence of better candidates, research along the main line continues to focus upon the pumping of simulation isomers that teach the structure and systematics for these giant resonances. This study has also been recently extended with encouraging results to the pumping of laserlike states with lifetimes on the order of tens of  $\mu\text{s}$ . The present paper will review these developments and the major breakthroughs which have significantly increased the feasibility of a gamma-ray laser.

### CONCEPTS

The critical key to the development of the ruby laser was the identification and exploitation of a bandwidth funnel in which a broad absorption band was linked through efficient cascading to a narrow laser level. This is an essential element as well to the blueprint for a nuclear analog to the ruby laser and is depicted by the schematic diagram of Fig. 1. Whether the initial state being pumped is the ground state or an isomer, the principal figure of merit is the integrated cross section,  $\pi b_a b_o \sigma_0 \Gamma / 2$ , for populating the upper laser level through the absorption state. Only one such state, or gateway, is shown in the figure but there could be more. The probabilities that the gateway will decay directly back to the initial level and either directly or by cascade to the laser level are  $b_a$  and  $b_o$ , respectively. These quantities together with the natural width of the absorption level,  $\Gamma$  give the useful, partial width describing the transfer of population,  $b_a b_o \Gamma$ . The parameter  $\sigma_0$  is one half of the peak value of the Breit-Wigner cross section and is proportional to the square of the wavelength of the pump photon. This means that the cross section for useful absorption of pump energy will be much larger for photons



than for particles of the same energy. This is another crucial element to the feasibility of a gamma-ray laser as discussed in detail later.

Optical pumping processes like that depicted in Fig. 1 have been known in nuclear physics for more than 50 years<sup>32</sup> and are called  $(\gamma, \gamma')$  reactions where  $\gamma$  and  $\gamma'$  refer to the incident and scattered photons, respectively. Values of integrated cross section for these reactions typically range<sup>19-22,33</sup> from 1's to 10's in the usual units (uu.) of  $10^{-29} \text{ cm}^2 \text{ keV}$ . However, the need for intense photon sources in the study of these reactions led to practical difficulties in accurately calibrating the incident flux. In particular the most difficult sources of x rays to characterize proved to be radionuclides for which all intensity away from the spectral lines resulted from environmentally sensitive Compton scattering. Thus little quantitative agreement could be found in the literature between values of integrated cross section obtained in different experiments. Even as late as 1987 there were serious contentions<sup>34</sup> over the mechanism by which these reactions occurred and the way in which expected fluorescence yields were calculated. Still the qualitative analysis of  $(\gamma, \gamma')$  experiments clearly showed that bandwidth funneling did occur in nuclei.

The earliest challenge to the gamma-ray laser project was to place the optical pumping of nuclei on a firm quantitative basis, beginning with a model for the reaction. The time-integrated yield of final-state nuclei,  $N_f$  obtained by irradiating a population of initial-state nuclei,  $N_i$  with a continuum of photons extending up to a maximum "endpoint" energy,  $E_0$  is given by

$$N_f = N_i \Phi_0 \int_0^{E_0} \sigma(E) F(E, E_0) dE \quad (1)$$

where  $\Phi_0$  is the total flux of incident photons integrated over the lifetime of the final state,  $F(E, E_0)$  is the distribution of energies within the continuum and  $\sigma(E)$  is the energy-dependent cross section for the reaction. The distribution  $F(E, E_0)$  is normalized such that

$$\int_0^{E_0} F(E, E_0) dE = 1 \quad (2)$$

It is now well known that all  $(\gamma, \gamma')$  reactions occurring at energies below the threshold for photoneutron production resonantly excite discrete states like that shown in Fig. 1. Although the widths of these gateways may be large on the nuclear scale, at this level there is little structure to most incident photon continua. If the gateways are well-spaced compared to their widths Eq. 1 becomes

$$A_f(E_0) = N_f / (N_i \Phi_0) = \sum_j (\sigma \Gamma)_j F(E_j, E_0) \quad (3)$$

where the yield has been expressed as the fractional activation per unit photon flux,  $A_f(E_0)$  and  $(\sigma \Gamma)_j = (\pi b_a b_o \sigma_0 \Gamma / 2)_j$  is the cross section for population of the final state through the  $j^{\text{th}}$  gateway integrated over a Lorentzian lineshape. The Breit-Wigner formula gives

$$\sigma_0 = \frac{\lambda^2}{2\pi} \frac{2I_j + 1}{2I_g + 1} \frac{1}{\alpha_p + 1} \quad (4)$$

where  $\lambda$  is the wavelength of the pump photon,  $I_j$  and  $I_g$  are the angular momenta of the gateway and ground states, respectively, and  $\alpha_p$  is the internal conversion coefficient for the pump transition.

## MODEL VALIDATION

The model of Eq. 3 was validated by using bremsstrahlung from five different accelerators to irradiate targets containing the few isomeric nuclei for which reliable gateway data was available in the literature. These devices were: two nuclear simulators, DNA/PITHON and DNA/Aurora, two medical linacs and one research linac, the injector to the superconducting Darmstadt linear accelerator (S-DALINAC). This approach, rather than that of using radionuclides as x-ray sources, was chosen due to the relative insensitivity of the intense, broad continua of bremsstrahlung to Compton scattering. Also, due to the wide use of electron accelerators in a variety of fields well-established computer codes have been developed for the accurate calibration of their photon output from measured currents and target geometries.

Gram sized samples were exposed for times ranging from seconds to hours for the cw machines and to single flashes from the pulsed-power devices. The yield of isomers produced by each irradiation were obtained by detecting fluorescence photons emitted after transferring the samples to a quieter environment. Standard corrections were made for the isotopic abundance, isomer lifetime, detection and emission efficiencies, and transparency of the samples to the fluorescence. Photon spectra were calculated with the EGS4 electron/photon transport code<sup>35</sup> adapted for each experiment to give both  $\Phi_0$  and  $F(E, E_0)$ . In some cases  $\Phi_0$  was verified by in-line dosimetry.

The results of these experiments<sup>19-22,24</sup> were in excellent agreement with the predictions of Eq. 3 using traditional literature values<sup>30,31,33</sup> of gateway energies and integrated cross sections for the calibration isotopes  $^{79}\text{Br}$ ,  $^{77}\text{Se}$ ,  $^{115}\text{In}$  and  $^{87}\text{Sr}$ . These values are summarized in Table I. A typical example is given in Fig. 2 which shows a composite excitation function obtained for the calibration isomer  $^{87}\text{Sr}^m$  using the above mentioned accelerators<sup>24,26</sup> and the newly installed

Texas-X research linac at the University of Texas at Dallas. It is important to note that the yield of the  $^{87}\text{Sr}$  isomer was orders-of-magnitude enhanced by nuclear bandwidth funneling over that which could have been accounted for by direct excitation of the metastable level from the ground state.

An important consequence of the confidence level established by these experiments was the development of a new method<sup>36</sup> for selectively sampling the energy distribution of intense photon fluxes and providing absolute measurements using isomeric photoexcitation reactions. Even more important for the present work, *there could no longer be any reasonable doubt of the model or procedures for quantitatively measuring fluorescence efficiencies using bremsstrahlung.* This methodology was then applied to the examination of candidate nuclei for a gamma-ray laser.

#### GIANT PUMPING RESONANCES

Many of the candidate isotopes for a gamma-ray laser are deformed nuclei whose energy levels are built upon rotational bands like those of diatomic molecules. For a spheroidal nucleus an additional quantum must be conserved in reactions,  $K$  which is the projection of the total angular momentum,  $J$  on the major axis of symmetry. The selection rules for electromagnetic transitions are therefore  $|\Delta J| \leq M$  and  $|\Delta K| \leq M$  where  $M$  is the multipolarity of the transition. In general, isomeric levels of these deformed nuclei have quite long lifetimes since they lie in bands whose values of  $K$  differ greatly from those of bands containing lower-lying states to which they would otherwise be radiatively connected. Such isomers would be ideal as an initial state in the pumping of a gamma-ray laser since much energy is already stored in the nucleus. However, this same property means that a bandwidth funnel like that of Fig. 1 would have to span substantial  $\Delta K$  and the integrated cross section for such a transfer of population could have been expected to be very small.

From this perspective the nuclide  $^{180}\text{Ta}$  was considered to be among the poorest candidates since its isomer stores only 75 keV and requires the largest change in angular momentum,  $8\hbar$  for transitions to the ground state.<sup>30,31</sup> However, this isotope carries the distinction of being the only naturally occurring isomer in nature, having a lifetime in excess of  $10^{12}$  years while its ground state has a half-life of only 8.1 hours. Since a macroscopic sample was readily available,  $^{180}\text{Ta}^m$  became the first candidate tested.

An experiment was conducted<sup>23</sup> in 1987 in which 1.2 mg of  $^{180}\text{Ta}^m$  was irradiated with bremsstrahlung from a 6 MeV medical linac and a large fluorescence yield was observed. This was the first demonstration that the energy stored in a nuclear isomer could be dumped to freely-radiating states by a  $(\gamma, \gamma')$  reaction as needed for a gamma-ray laser. Simply the observation of any fluorescence from a mg sized target when grams of material were needed for the calibration isotopes was evidence of pumping of unexpected magnitude and analysis<sup>23</sup> of the data indicated that the partial width for the dumping of  $^{180}\text{Ta}^m$  was about 0.5 eV. This was much longer than the  $\mu\text{eV}$  widths measured for the population of the calibration isotopes of Table I.

The gateway excitation energies for this isomer were determined by a series of irradiations<sup>23</sup> made with the variable energy S-DALINAC. Fourteen different endpoints in the range from 2.0 MeV to 5.5 MeV were used to obtain the excitation function shown in Fig. 3. As in the case of the calibration isomer,  $^{87}\text{Sr}^m$ , sharp increases in the yield as a function of endpoint, called activation edges, were observed indicating the locations of the gateways. Using these locations and incident photon spectra computed with EGS4, the excitation function was iteratively fit with Eq. 3 and trial values for the  $(\sigma\Gamma)_i$ . The fitted gateway parameters are given in Table II. The lowest-lying gateway identified<sup>24</sup> for the dumping of the  $^{180}\text{Ta}$  isomer was at 2.8 MeV with an integrated cross section of 12000 uu. The demonstration that populations of

nuclear isomers can be dumped with bremsstrahlung, and with integrated cross sections  $10^4$  times larger than could have been expected stands as the first major breakthrough towards a gamma-ray laser and has enhanced its feasibility by four orders-of-magnitude.

These "giant pumping resonances" were also observed<sup>25</sup> for the second poorest candidate,  $^{123}\text{Te}$ . However, no other candidates were available in sufficient amounts for testing so research focused on the pumping of simulation isomers in order to learn more about the systematics and structure of these gateways. A preliminary survey<sup>26</sup> of the pumping of 19 isomeric simulation nuclei was conducted over a fairly coarse mesh of bremsstrahlung endpoints using the nuclear simulators and the medical linacs. Again, giant pumping resonances for transferring large  $\Delta K$  were observed for nuclei in a region of masses near  $A = 180$ . A refined survey<sup>27</sup> was obtained using the S-DALINAC and served to locate the gateways and measure integrated cross sections for four isotopes neighboring  $^{180}\text{Ta}$ . The results of these studies are shown in Fig. 4 which indicates that both the excitation energies and integrated cross sections for pumping isomers vary slowly between neighboring masses. The integrated cross sections were also correlated<sup>27</sup> with the ground state deformation, a property of the nuclear core.

The unexpected magnitudes measured for pumping resonances in the mass-180 region have been difficult to interpret in the single-particle model and the apparent ease with which such large  $\Delta K$  is transferred has been a mystery. However, an understanding of the basic principle has taken form which identifies these gateway locations with energies that excite collective oscillations of the nuclear core for which there would be no fixed shape by which  $K$  could be conserved. This would break the selection rule for  $K$  through strong admixtures of single-particle states. It is interesting to speculate that these giant pumping resonances may parallel the appearance of double minima shown to occur in the potential energy of heavy but nonfissile nuclei.<sup>37</sup> These minima are

expected to lie at excitation energies of a few MeV while the gateways identified in the mass-180 region lie between 2.5 MeV and 3 MeV.

Support for this idea comes not only from the systematics of the giant resonances for pumping isomers but also from experimental results that demonstrated<sup>38</sup> that the spontaneous electromagnetic decay of the isomer  $^{174}\text{Hf}^m$  proceeded through a level at 2.65 MeV which provided an even larger degree of K transfer,  $\Delta K = 14$ . As shown in Fig. 5 this is remarkably close to the energy of the K-mixing gateway at  $2.8 \pm 0.1$  MeV found for  $^{180}\text{Ta}$ . The understanding of giant pumping resonances as coupling to core oscillations means that the behavior of candidate isotopes lying near those nuclides tested can be reasonably be interpolated from the systematics data. Thus it can be expected that if an isomer starts with enough energy, little additional pump would be needed to reach a giant pumping resonance which lay 2.5 - 3.0 MeV above the ground state, but perhaps only a few hundred keV above the metastable state. This understanding constitutes a second breakthrough towards the feasibility of a gamma-ray laser.

The above described discoveries have significantly improved the feasibility of a gamma-ray laser by lowering pump requirements for a gamma-ray laser, primarily because of the large sizes of the integrated cross sections measured. However, the resolution of those experiments only permitted the gateways to be located to within  $\pm 0.1$  MeV as shown in Table II. The possibility was therefore left open that the reaction strength might not be concentrated in a few transitions with relatively large widths, but instead might be spread over a great number of closely spaced levels with considerably reduced widths. This was of particular concern for the nuclei favored in Fig. 4 which have large excited state densities, and even more so for  $^{180}\text{Ta}$  which is a rare odd-odd nucleus. Such behavior would seriously degrade the ratio of useful pump energy absorbed resonantly by the active nuclei to the energy absorbed nonresonantly, making the

management of waste heat more difficult. A series of experiments were performed to explore this possibility.

Isomeric excitation functions reflect only one specific reaction channel of the process depicted in Fig. 1, that is the strong absorption of incident photons in a transition from the ground state to the gateway followed by a decay cascade leading to the metastable level. However, another important channel is that of absorption followed by a direct decay of the gateway back to the ground state. From Fig. 1 it can be seen that a large  $(\sigma\Gamma)$  for the population of an isomer will be accompanied by elastic scattering of significant numbers of photons with an analogous integrated cross section,  $(\sigma\Gamma)_{el} = \pi b_0^2 \sigma_0 \Gamma / 2$ . The detection of these photons in real time during an irradiation permits the direct measurement of excitation energies and widths for nuclear transitions and forms the basis for nuclear resonance fluorescence (NRF) experiments.

An experimental arrangement<sup>39</sup> especially designed for NRF measurements was used to investigate<sup>28,29</sup> two isomeric nuclides, <sup>89</sup>Y and <sup>115</sup>In which were chosen for their large natural isotopic abundances and the degree to which their structure could be characterized within the unified model. Gram-sized samples were sandwiched between aluminum and boron calibration targets and were irradiated with well-collimated bremsstrahlung. Endpoint energies were used which permitted the observation of photons scattered by strong transitions with excitation energies in the range from 1.5 MeV to 4.5 MeV. These photons were measured with carefully shielded detectors placed off-axis and appeared in pulse-height spectra as peaks superimposed on a large Compton background. Isomeric excitation functions were also measured for these isotopes.

Detailed spectra are available in the literature<sup>28,29</sup> but the relevant points are illustrated in schematic form for <sup>115</sup>In in Fig. 6. As shown in Fig. 6a the excitation function data<sup>28</sup> indicated



two giant pumping resonances located at  $2.8 \pm 0.1$  MeV and  $3.2 \pm 0.1$  MeV. The striking discovery was in the NRF data which only exhibited the strong transitions of Fig. 6b with energies lying within the experimental resolution of the gateways. Thus these few levels, or a subset thereof, were responsible for the population of the isomer. This conclusion was confirmed by unified-model calculations which showed that the absorption strength was concentrated into a small number of E1 or E2 transitions with excitation energies near those measured. Similar results<sup>29</sup> were obtained for  $^{89}\text{Y}$ . Although a one-to-one correspondence was beyond the limits of the theoretical approach, the correlation between calculations and experiments clearly showed that the gateways in  $^{89}\text{Y}$  and  $^{115}\text{In}$  correspond to a small number of levels having relatively large partial widths. This is the third major breakthrough in the feasibility of a gamma-ray laser.

#### A LASER MODEL

The 1990's model for a gamma-ray laser is fundamentally identical to the nuclear analog of the ruby laser presented<sup>2</sup> in 1982. Isomeric nuclei would be doped into a thin, low-Z diluent and would be pumped by a flash of x rays. However, the discovery of giant pumping resonances has relaxed some of the original constraints, improving the feasibility of a gamma-ray laser by orders-of-magnitude over that originally projected. Thus it is instructive to recompute the model in terms of this new data. Of course the precise identity of the best nuclide to model is unknown so it is necessary to begin with certain assumptions:

- 1) There is a single pump transition with an excitation energy of  $E_j = 30$  keV.
- 2) The initial state is an isomer with a sufficiently high energy that 1) is possible.
- 3) The gateway is a giant pumping resonance having a partial width of  $b_p b_o \Gamma = 1$  eV.
- 4) The output transition is around 100 keV.

- 5) The active nuclei are implanted in a thin film of diamond.
- 6) The Borrmann effect enhances the ratio of resonant to nonresonant absorption by a factor of 10.

The most critical assumptions are those of 1) and 2). However, isomers can be found over a large range of excitation energies from 10's of keV to several MeV so there is only a statistical question whether a giant pumping resonance can be found within 30 keV of an isomer. The remaining conditions are based on recent discoveries, the present state-of-the-art technology for producing thin diamond films<sup>40</sup> and projections for the near future.

Following the development<sup>2</sup> of 1982, under small signal conditions the threshold for amplification in a single pass down the length of the film requires the fraction of active nuclei pumped to be  $N_i/N_t \geq \sigma_{NR}/\sigma_R$ . The  $\sigma_{NR}$  and  $\sigma_R$  are the cross sections for nonresonant and resonant absorption, respectively, of the 100 keV output photons. It can be shown<sup>1,41</sup> that with the assumed Borrmann enhancement a midrange value for this fraction is  $10^{-4}$  although even more favorable values are possible. It is also conceivable that refinement effects like superradiance may serve to reduce the threshold requirement further. Using the required pump fraction and the Breit-Wigner cross section of Eq. 4 for a 30 keV photon with  $I_i = I_o$  and  $\alpha_p = 0$ , Eq. 3 gives the needed spectral flux of  $\Phi_0 F(E_i, E_o) = 5.9 \times 10^{13} \text{ cm}^{-2} \text{ eV}^{-1}$ , or a spectral fluence of  $177 \text{ mJ cm}^{-2} \text{ eV}^{-1}$ . If edge filters or ablation layers are used prior to the doped layer the pump bandwidth could be limited to 3 keV, yielding a total fluence of  $530 \text{ J cm}^{-2}$ .

The essential concept for the management of the thermal economy of a gamma-ray laser is that the mean free path (MFP) for useful, resonant absorption of the 30 keV pump must be much smaller than the MFP for nonresonant, photoelectric absorption. Also the MFP for resonant absorption must be smaller than the MFP for any primary photoelectrons produced by

nonresonant events in the film. Primary photoelectrons are the dominant source of heating since relatively few conversion electrons will be produced by energetic gamma transitions in the pump cascade. These conditions can be met by doping a thin diamond film with a 10 % concentration of active nuclei. In order to maximize the absorption of the pump in this example, the thickness of the film is chosen to equal one MFP for 30 keV photons, that is 0.67  $\mu\text{m}$ .

In the case of isotopes which are rare earths or platinides, the 30 keV pump would lie below the K edge and about 15 keV above the L edge, giving primary photoelectrons with energies near 15 keV. In diamond the range of these electrons would be about 3.0  $\mu\text{m}$  so only 20% of the primaries would be stopped in the host film.<sup>41</sup> The fraction of the incident pump fluence which would be stopped in the laser medium by nonresonant absorption is  $2.4 \times 10^{-3}$  so the total fraction of input fluence which would be converted to heat would be  $4.8 \times 10^{-4}$ . The total fluence degraded to heat would then be 255  $\text{mJ cm}^{-2}$  and the thermal loading of the film would be 3.8  $\text{KJ cm}^{-3}$ . For comparison, the energy density due to useful, resonant absorption would be 2.6  $\text{KJ cm}^{-3}$ .

To have stimulated emission the host lattice must preserve the natural width of the output transition through the Mössbauer effect. The complex dependence of the recoil-free-fraction upon materials and gamma transition energies was discussed in Ref. 1 and it was shown that little degradation of this factor occurred for temperatures even as high as the Debye temperature,  $\Theta_D$ . In diamond the Debye temperature is  $\Theta_D = 2230 \text{ K}$  and the energy content of a film at a temperature  $T = \Theta_D$  is computed<sup>42</sup> to be about 11  $\text{KJ cm}^{-3}$ . Thus the estimated instantaneous thermal loading of 3.8  $\text{KJ cm}^{-3}$  gives a "safety factor" of nearly three for preserving the stimulated emission cross section. A similar calculation for a host film of beryllium gives comparable results.<sup>41</sup>

Much can be done to reduce the heating further since phonons can be transported across the 0.67 mm film in about 100 ps while lasing levels would have lifetimes ranging from 10's of ns to 10's of  $\mu$ s. Thus over the duration of the pump flash the cooling of the film could be improved significantly over that of the example above. However, the techniques available depend upon precise knowledge of the actual isotope and the absorption edges of the materials used. Still the model demonstrates that there is a large safety margin between likely amounts of thermal loading and the amounts which can be tolerated in stiff lattices like diamond or beryllium.

### RECENT DEVELOPMENTS

The feasibility of a gamma-ray laser has been greatly enhanced by the discovery of giant resonances for the pumping and dumping of nuclear isomers. Such a metastable state would be used as a high-lying storage level from which a modest pump would populate a lasing level. Thus the next step in the project has been to examine the pumping of more laserlike excited nuclear states with lifetimes on the order of  $\mu$ s, a task which is requiring new research tools and techniques.

A milestone for the gamma-ray laser project was reached in 1992 with the construction of an underground facility dedicated to the pumping of nuclear materials and the installation of the Texas-X research linear accelerator at the University of Texas at Dallas. This 4 MeV linac was designed to produce pulses of bremsstrahlung of 2.78  $\mu$ s duration with a repetition rate of up to 360 Hz, characteristics which were ideal for the study of the pumping of states with lifetimes greater than 1  $\mu$ s. After an initial emplacement and testing period, the output spectrum of the Texas-X was calibrated absolutely by photoactivation measurements.<sup>43</sup> A survey of previously tested isotopes was then conducted as a test of consistency. The agreement with earlier measurements was excellent as evidenced by the data for the calibration isomer  $^{87}\text{Sr}^m$  in Fig. 2.

To investigate the pumping of laserlike levels a new technique is being developed which allows the observation of fluorescence on a  $\mu\text{s}$  timescale. Since these lifetimes are too short to permit the physical transfer of irradiated samples it is necessary to detect fluorescence in situ. In developmental experiments this was accomplished by placing a heavily shielded CsF scintillator and its photomultiplier tube (PMT) within the linac chamber such that no direct exposure to bremsstrahlung could occur. The detector housing was located off the beam axis so photons coming from an irradiated sample could be viewed through a collimated opening. Samples were placed on axis in close proximity to the converter target which produced the bremsstrahlung in order to maximize the incident flux and thereby the amount of nuclear excitation. When operated at a repetition rate of 360 Hz the linac produced pulses of x rays which were separated by 2.78 ms. By gating the PMT off during each pulse it was possible to prevent the detector from being blinded by the large numbers of Compton photons present in real time. A stable high voltage to the PMT was then reestablished over a few  $\mu\text{s}$  to permit the detection of fluorescence from any excited states populated during the pulse. During the measurement period which extended until the next pulse a time-to-amplitude converter (TAC) was used to obtain decay spectra that were collected over a large number of gating cycles. The details of this technique are discussed in a later chapter.

Preliminary experiments were conducted with this emerging technology to study the excitation of  $\mu\text{s}$  states in the isotopes  $^{181}\text{Ta}$  and  $^{176}\text{Hf}$  which have natural abundances of 99.998% and 5.206%, respectively. The energetics of these nuclides are described by the schematic of Fig. 7. In one experiment a gram-sized sample of tantalum was irradiated and fluorescence was detected from the decay cascade of the 615 keV, 18  $\mu\text{s}$  state of  $^{181}\text{Ta}$ . The data are shown in Fig. 8a and excellent agreement was indicated between the measurements and the literature value for the lifetime of the state. An experiment conducted with a hafnium sample produced the

similar data of Fig. 8b. For this nucleus the level of 1.559 MeV feeds that at 1.333 MeV, resulting in a sequential decay. Again excellent agreement was obtained between the measurements and literature values for the half-lives. Evidence was also seen in Fig. 8b for the excitation of the 401  $\mu$ s level at 2.866 MeV.

The numbers of nuclei excited by a single pulse were calculated from the counts obtained over a specified time interval and from the detection efficiency determined with a  $^{57}\text{Co}$  calibration source placed at the sample position. Only photons in the cascade having energies greater than 250 keV were detected due to threshold settings of the electronics so a correction was made for the fraction of decay events which were observable. The analyses of the results of Fig. 8 using Eq. 3 provided lower bounds for the integrated cross sections for populating these laserlike levels which were comparable to those measured for the production of isomers. The values found were 650  $\mu$ b. and 1650  $\mu$ b. respectively for the excitation of the 18  $\mu$ s state of  $^{181}\text{Ta}$ , and both the 9.6  $\mu$ s and 9.9  $\mu$ s states of  $^{176}\text{Hf}$ . The measurement of such large integrated cross sections for laserlike levels greatly strengthens the feasibility of a gamma-ray laser optically pumped from an initial isomeric state. This technique also opens a new region of the parameter space shown in Fig. 9 for examination of the properties of nuclei of interest for a gamma-ray laser. Further efforts are underway to refine the technology and to proceed with extensive studies of new delayed scattering nuclei in the upper portion of Fig. 9.

Another recent development was the implantation by a local small business of isotopically pure  $^{57}\text{Fe}$  nuclei within a thin diamond film deposited on a titanium substrate. The sample represented a realistic simulation of a host material capable in principle of preserving a natural width for the stimulated-emission cross section, a necessary condition for a gamma-ray laser. In fact Mössbauer spectra showed this to be the case and the quality of the data obtained from the

4.5  $\mu\text{g}$  of  $^{57}\text{Fe}$  within the film was not significantly degraded from that obtained from a milligram enriched  $^{57}\text{Fe}$  sample. More details are discussed in a following chapter.

### CONCLUSIONS

The discovery of giant resonances for pumping and dumping isometric populations coupled with the development of the technology for producing thin diamond films have enhanced the feasibility of a gamma-ray laser by orders-of-magnitude over that projected in the blueprint of 1982. All of the component concepts have now been demonstrated experimentally and the persistent but false tenets of theoretical dogma which have historically inhibited the development of a gamma-ray laser have been eliminated. In particular it is not necessary to melt the host lattice in order to optically pump a nuclear system to threshold. *There are no a priori obstacles to the realization of a gamma-ray laser. A gamma-ray laser is feasible if the right combination of energy levels occurs in some real material.* The remaining question to resolve is whether or not one of the better candidates has its isomeric level located sufficiently close to a giant resonance for dumping angular momenta.

This work was supported by SDIO/TNI under the direction of NRL.

## REFERENCES

1. G. C. Baldwin, J. C. Solem and V. I. Goldanskii, Rev. Mod. Phys. 53, 687 (1981).
2. C. B. Collins, F. W. Lee, D. M. Shemwell, B. D. DePaola, S. Olariu and I. Popescu, J. Appl. Phys. 53, 4645 (1982).
3. V. S. Letokhov, Sov. J. Quant. Electron. 3, 360 (1974).
4. B. Arad, S. Eleizer and Y. Paiss, Phys. Lett. 74A, 395 (1979).
5. C. B. Collins, S. Olariu, M. Petrascu and I. Popescu, Phys. Rev. Lett. 42, 1397 (1979).
6. C. B. Collins, S. Olariu, M. Petrascu and I. Popescu, Phys. Rev. C 20, 1942 (1979).
7. S. Olariu, I. Popescu and C. B. Collins, Phys. Rev. C 23, 50 (1981).
8. S. Olariu, I. Popescu and C. B. Collins, Phys. Rev. C 23, 1007 (1981).
9. C. B. Collins, in Proceedings of the International Conference on Lasers '80, ed. C. B. Collins (STS Press, McLean, VA, 1981) p 524.
10. R. A. Rivlin, Kvantomya Elektron. (Moscow) 4, 676 [Sov. J. Quantum Electron. 7, 380 (1977)].
11. C. B. Collins, in Laser Technique for Extreme Ultraviolet Spectroscopy, ed. T. J. McIlrath and R. R. Freeman (AIP Conference Proceedings No. 90, New York, 1982) p 454.
12. C. B. Collins, in Proceedings of the International Conference on Lasers '81, ed. C. B. Collins (STS Press, McLean, VA, 1982) p 291.
13. C. B. Collins, in CRC Handbook of Laser Science and Technology, Supplement 1: Lasers, ed. by M. J. Weber (CRC Press, Boca Raton, FL, 1991) p 561.
14. B. D. DePaola and C. B. Collins, J. Opt. Soc. Am. B 1, 812 (1984).
15. C. B. Collins and B. D. DePaola, Optics Lett. 10, 25 (1985).
16. B. D. DePaola, S. S. Wagal and C. B. Collins, J. Opt. Soc. Am. B 2, 541 (1985).
17. B. D. DePaola and C. B. Collins, J. Opt. Soc. Am. B 1, 812 (1984).



18. T. W. Sinor, P. W. Reittinger and C. B. Collins, Phys. Rev. Lett. 62, 2547 (1989).
19. J. A. Anderson and C. B. Collins, Rev. Sci. Instrum. 58, 2157 (1987).
20. J. A. Anderson and C. B. Collins, Rev. Sci. Instrum. 59, 313 (1988).
21. C. B. Collins, J. A. Anderson, Y. Paiss, C.D. Eberhard, R.J. Peterson and W. L. Hodge, Phys. Rev. C 38, 1852 (1988).
22. J. A. Anderson, M. J. Byrd and C. B. Collins, Phys. Rev. C 38, 2833 (1988).
23. C. B. Collins, C. D. Eberhard, J. W. Glesener and J. A. Anderson, Phys. Rev. C 37, 2267 (1988).
24. C. B. Collins, J. J. Carroll, T. W. Sinor, M. J. Byrd, D. G. Richmond, K. N. Taylor, M. Huber, N. Huxel, P. v. Neumann-Cosel, A. Richter, C. Spieler and W. Ziegler, Phys. Rev. C 42, R1813 (1988).
25. J. J. Carroll, T. W. Sinor, D. G. Richmond, K. N. Taylor, C. B. Collins, M. Huber, N. Huxel, P. v. Neumann-Cosel, A. Richter, C. Spieler and W. Ziegler, Phys. Rev. C 43, 1238 (1991).
26. J. J. Carroll, M. J. Byrd, D. G. Richmond, T. W. Sinor, K. N. Taylor, W. L. Hodge, Y. Paiss, C. D. Eberhard, J. A. Anderson, C. B. Collins, E. C. Scarbrough, P. P. Antich, F. J. Agee, D. Davis, G. A. Huttlin, K. G. Kerris, M. S. Litz and D. A. Whittaker, Phys. Rev. C 43, 1238 (1991).
27. C. B. Collins, J. J. Carroll, K. N. Taylor, D. G. Richmond, T. W. Sinor, M. Huber, P. v. Neumann-Cosel, A. Richter and W. Ziegler, Phys. Rev. C 46, 952 (1992).
28. P. v. Neumann-Cosel, A. Richter, C. Spieler, W. Ziegler, J. J. Carroll, T. W. Sinor, D. G. Richmond, K. N. Taylor, C. B. Collins and K. Heyde, Phys. Lett. B266, 9 (1991).

29. M. Huber, P. v. Neumann-Cosel, A. Richter, C. Schlegel, R. Schulz, J. J. Carroll, K. N. Taylor, D. G. Richmond, T. W. Sinor, C. B. Collins and V. Y. Ponomarev, submitted to Nucl. Phys. (pending).
30. *Evaluated Nuclear Structure Data File* (Brookhaven National Laboratory, Upton, New York, 1986) and the Nuclear Data Sheets.
31. E. Browne and R. B. Firestone, Table of Radioactive Isotopes, ed. by V. S. Shirley (Wiley, New York, 1986).
32. B. Pontecorvo and A. Lazard, C. R. Acad. Sci. 208, 99 (1939).
33. E. C. Booth and J. Brownson, Nucl. Phys. A98, 529 (1967).
34. I. Bikit, J. Slivka, I. V. Anicin, L. Marinkov, A. Ruydic and W. D. Hamilton, Phys. Rev. C 35, 1943 (1987).
35. *The EGS4 Code System*, W. R. Nelson, H. Hirayama and D. W. O. Rogers, Stanford Linear Accelerator Center Report No. SLAC 265, 1985 (unpublished).
36. J. A. Anderson, C. D. Eberhard, K. N. Taylor, J. M. Carroll, J. J. Carroll, M. J. Byrd and C. B. Collins, IEEE Trans. Nucl. Sci. 36, 241 (1989).
37. M. Girod, J. P. Delaroche, D. Gogny and J. F. Berger, Phys. Rev. Lett. 65, 416 (1990).
38. P. M. Walker, F. Sletten, N. L. Gjørup, M. A. Bentley, J. Borggreen, B. Fabricius, A. Holm, D. Howe, J. Pedersen, J. W. Roberts and J. F. Sharpey-Schafer, Phys. Rev. Lett. 65, 416 (1990).
39. W. Ziegler, C. Rangacharyulu, A. Richter, and C. Spieler, Phys. Rev. Lett. 65, 2515 (1990).
40. C. B. Collins, F. Davanloo, T. J. Lee, J. H. You and H. Park, Am. Ceram. Soc. Bull. 10, 1535 (1992).

41. "Thermal Economy of a Gamma-Ray Laser," C. B. Collins in the Center for Quantum Electronics: The Gamma-Ray Laser, Final Technical Report 1986-1989, p 1 (unpublished).
42. C. Kittel, Introduction to Solid State Physics, 6th Edition (Wiley, New York, 1986) p 106.
43. J. J. Carroll, K. N. Taylor, T. W. Sinor, C. Hong, J. D. Standifird and C. B. Collins, to be submitted to Nucl. Inst. Meth.

Table I

Summary of the traditional literature values<sup>30,33</sup> of gateway parameters for the calibration isomers used to validate the model of Eq. 3.

Isomer	$E_i$ [MeV]	$(\sigma\Gamma)_i$ [uu.]	$b_i b_0 \Gamma$ [ $\mu$ eV]
<sup>79</sup> Br <sup>m</sup>	0.761	6.2	4.7
<sup>77</sup> Se <sup>m</sup>	0.250	0.20	~0.010
	0.480	0.87	0.10
	0.818	0.7	0.13
	1.005	30	0.0039
	1.078	20	63.2
<sup>87</sup> Sr <sup>m</sup>	1.22	8.5	~50
	1.88	16	~230
	2.67	380	~700

Table II

Recently measured values<sup>24</sup> of integrated cross sections,  $(\sigma\Gamma)_{ij}$  for the reaction  $^{180}\text{Ta}^m(\gamma,\gamma')^{180}\text{Ta}$ .

The gateway excitation energies  $E_j$  for these levels are given at the centers of the ranges of energies that could be resolved experimentally.

$E_j$ [MeV]	$\sigma\Gamma_j$ [uu.]	$b_a b_o \Gamma$ [eV]
$2.8 \pm 0.1$	$12000 \pm 2000$	$\sim 0.25$
$3.6 \pm 0.1$	$35000 \pm 5000$	$\sim 1.2$

## CAPTIONS

Figure 1: Schematic representation of the bandwidth funneling of population to a laser level through a gateway state with natural width  $\Gamma$ . The incident photon  $\gamma$  is absorbed with a cross section  $\sigma_0$  by the initial level which may be either a ground state or an isomer. The cascade from gateway to laser level is shown by the dotted line with promptly emitted photons being the  $\gamma'$ .

Figure 2: Fractional activations,  $A_f$  for the reaction  $^{87}\text{Sr}(\gamma, \gamma')^{87}\text{Sr}^m$  as a function of bremsstrahlung endpoint,  $E_0$  obtained with 5 different accelerators. The solid curve plots values computed from Eq. 3 using gateway parameters found in the literature<sup>24,33</sup> and calculated photon spectra. The agreement of these values with the measurements was excellent and validated the procedures.

Figure 3: Fractional activations,  $A_f$  for the reaction  $^{180}\text{Ta}^m(\gamma, \gamma')^{180}\text{Ta}$  as a function of bremsstrahlung endpoint,  $E_0$  obtained with the S-DALINAC. Gateway parameters were determined<sup>24</sup> by fitting the measured excitation function using Eq. 3 with trial values for the  $(\sigma\Gamma)_i$  which were found to be  $10^4$  larger than those usually measured for  $(\gamma, \gamma')$  reactions. These data demonstrated the dumping of an isomeric population with x rays.

Figure 4: Systematics for integrated cross sections and gateway locations for pumping nuclear isomers with photons. The groupings correspond to mass islands between magic numbers for neutrons and protons. The best candidates for a gamma-ray laser lie in the mass-180 island. Within this island the integrated cross sections and excitation energies, indicated by the X symbols plotted by the right-hand ordinate, vary only slowly with changing mass number, A.

Figure 5: Energetics for the spontaneous decay<sup>38</sup> of  $^{174}\text{Hf}^m$  through an intermediate state providing  $\Delta K = 14$  compared with those<sup>24</sup> for the dumping of  $^{180}\text{Ta}^m$  through a similar intermediate state. In the case of  $^{180}\text{Ta}^m$ , the dumping reaction provides  $\Delta K = 8$ . Both gateways are expected to be admixtures of single-particle states, thereby producing significant K mixing.

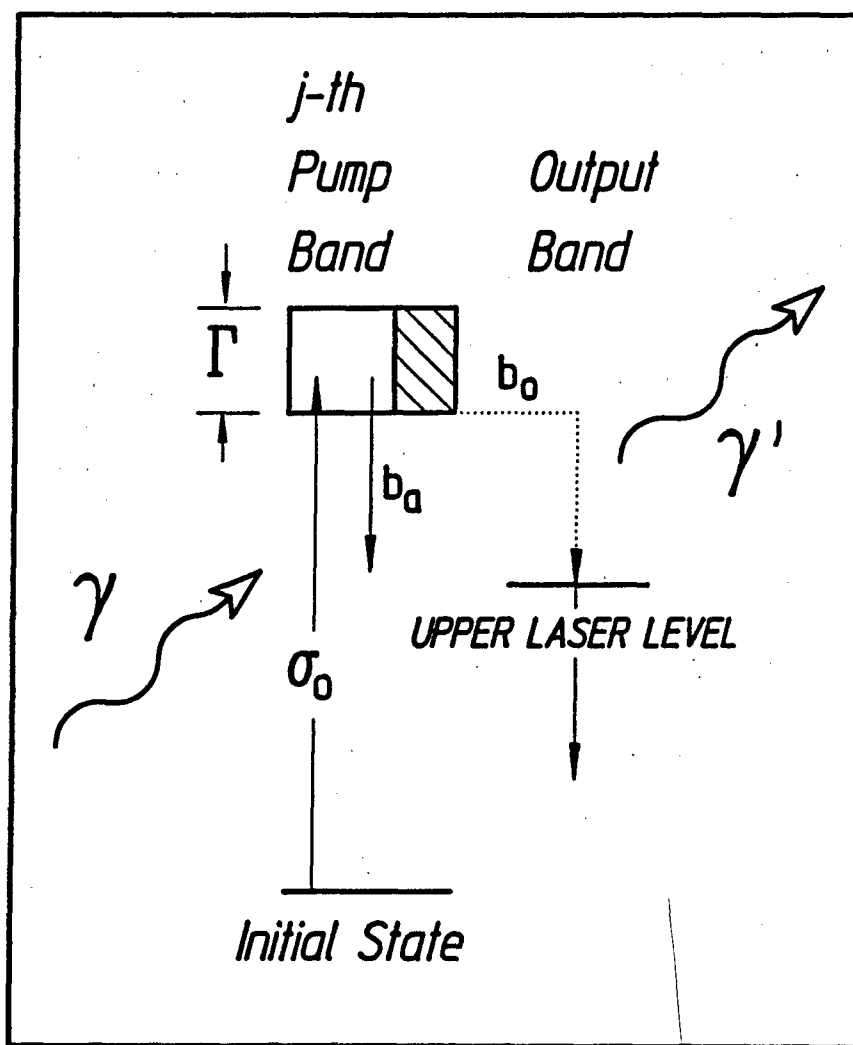
Figure 6: Schematic representing integrated cross sections<sup>28</sup> for a) population of the isomer  $^{115}\text{In}^m$  obtained from excitation function measurements and for b) elastic scattering by absorption transitions obtained from NRF measurements. Gateway locations of a) were determined only within  $\pm 0.1$  MeV and strongly scattering levels were only observed within these bands. Thus a subset of the transitions of b) are responsible for the population of the isomer. This was confirmed by unified model calculations.

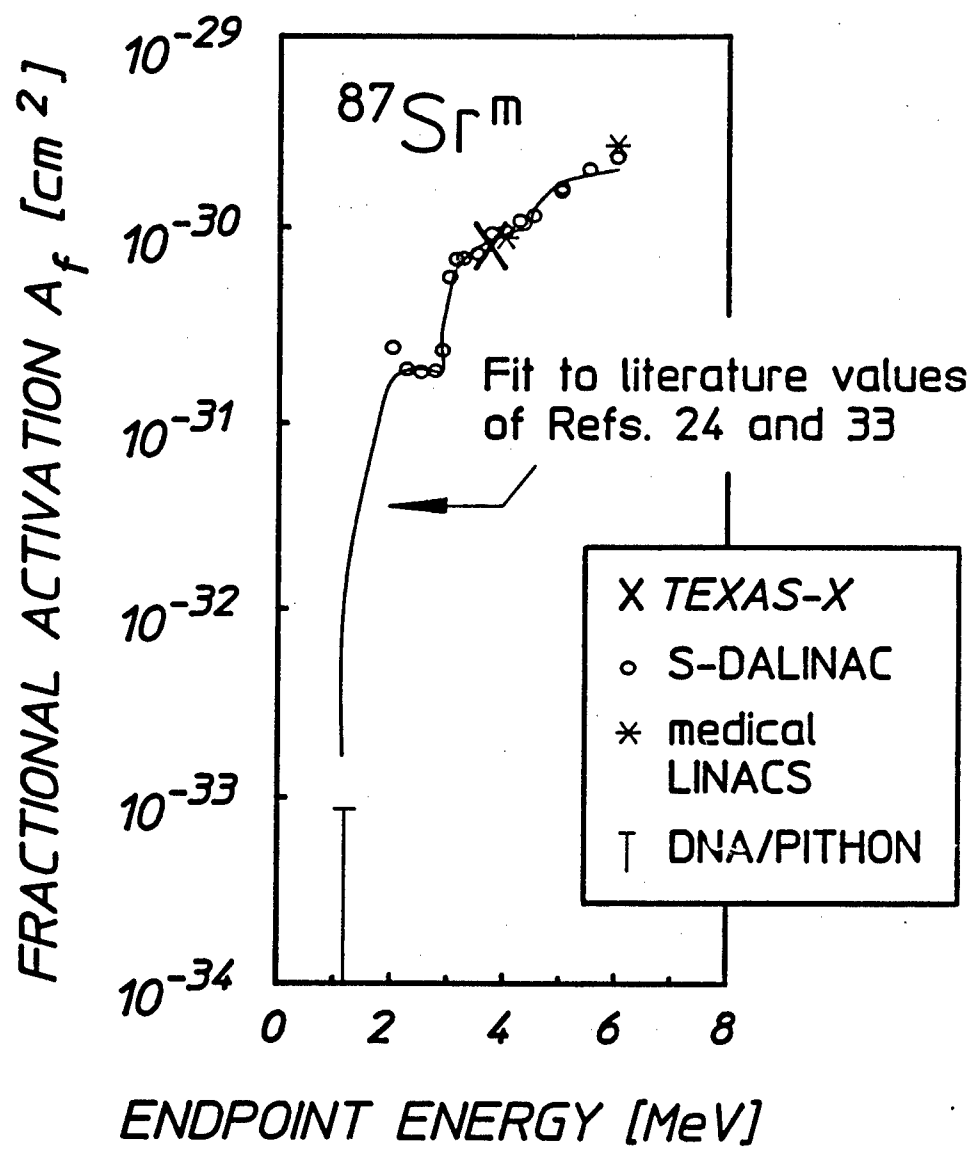
Figure 7: Energetics for the pumping of laserlike levels and decay cascades from those states for the nuclei a)  $^{181}\text{Ta}$  and b)  $^{176}\text{Hf}$ . Half-lives where known<sup>30,31</sup> are indicated to the right of the states. Heavy dashed arrows identify the transitions observable with the thresholds set for the detection electronics.

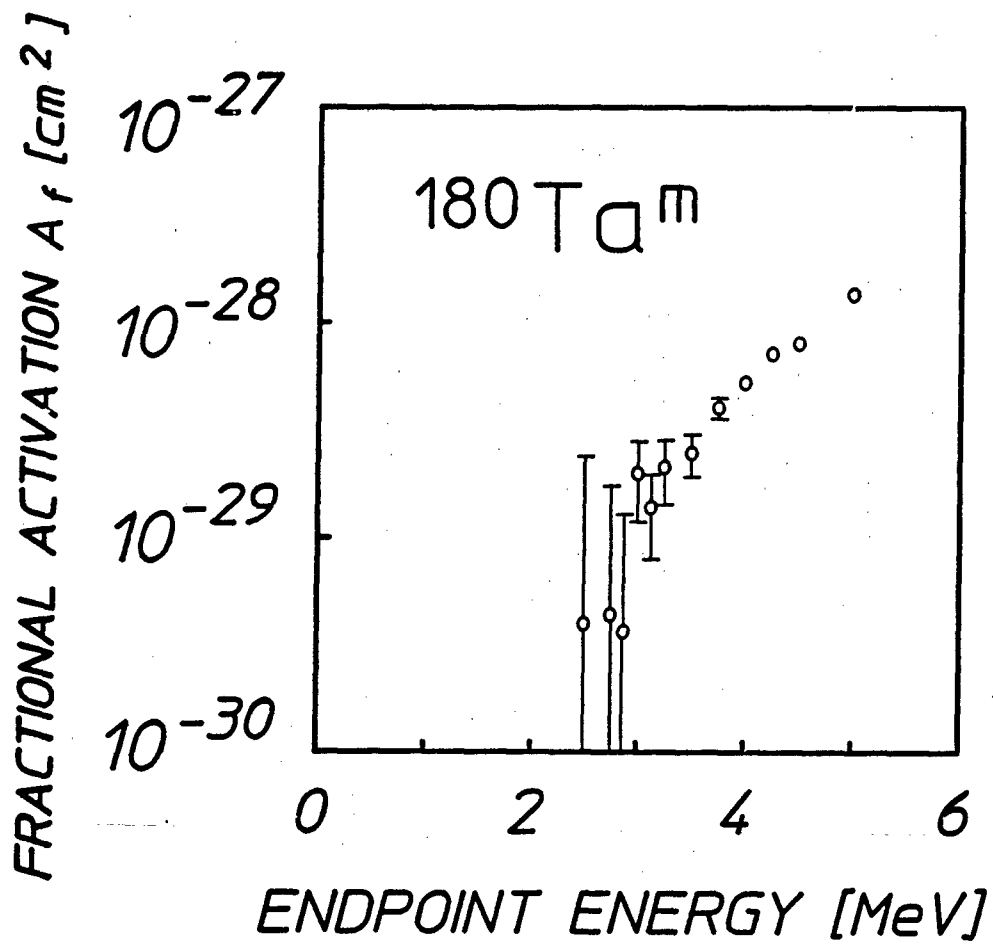
Figure 8: Pulse-height spectra obtained with a time-to-amplitude converter over multiple gating cycles for the excitation of  $\mu\text{s}$  lifetime states in a)  $^{181}\text{Ta}$  and b)  $^{176}\text{Hf}$ . The schematic indicates that data collection began when the CsF detector was gated on 8  $\mu\text{s}$  after the end of each x-ray pulse. The decay of the data gave excellent agreement between measured half-lives and those values available in the literature.<sup>30,31</sup> Analysis of these results indicated that lower bounds for the integrated cross sections for pumping were comparable to those previously obtained for the population of isomers.

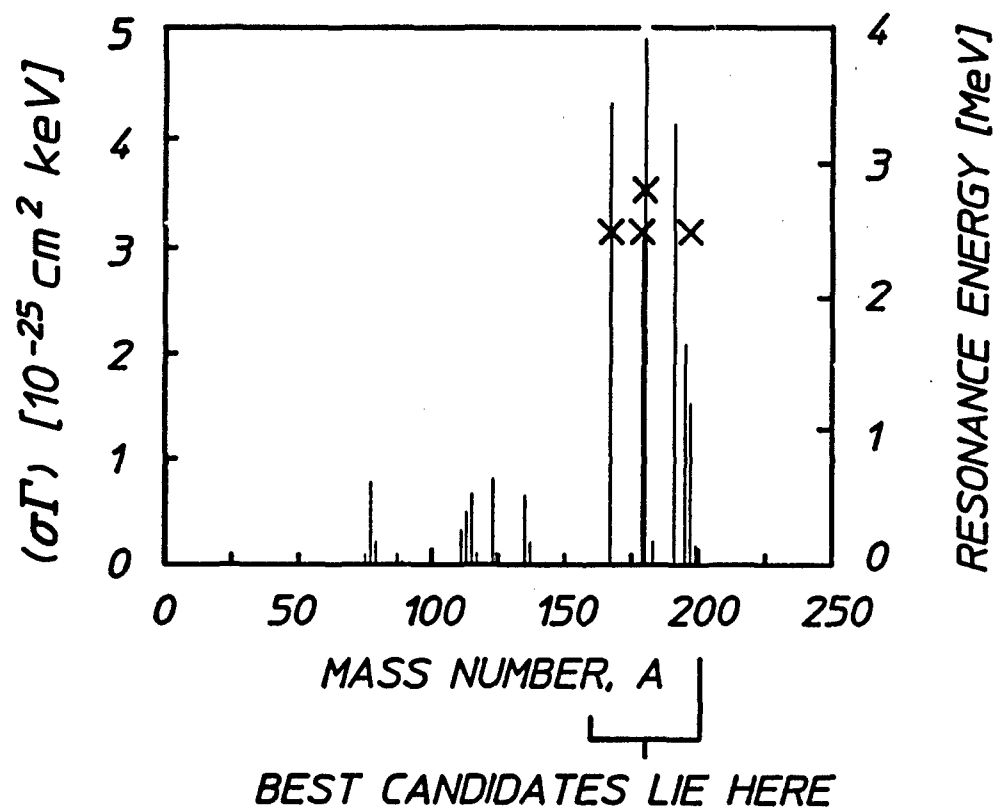
Figure 9: Plot of the parameter space for the description of the properties of nuclei of interest for a gamma-ray laser. Mössbauer nuclei are shown as circles, the simulation nuclei of Ref. 26 as squares and nuclides which require delayed scattering techniques for evaluation as triangles. Filled symbols indicate those for which fluorescence was successfully excited through giant pumping resonances. The two large triangles represent the isotopes  $^{181}\text{Ta}$  and  $^{176}\text{Hf}$  for which preliminary measurements were recently obtained.

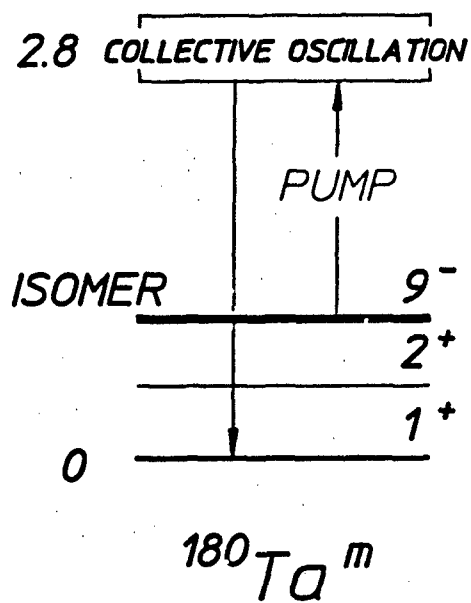
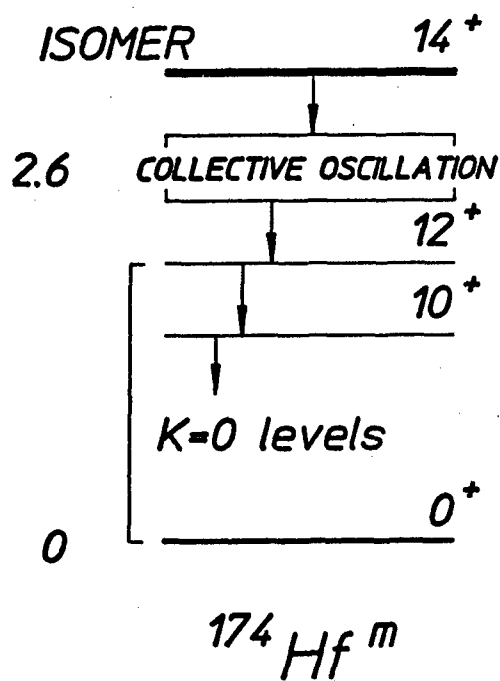


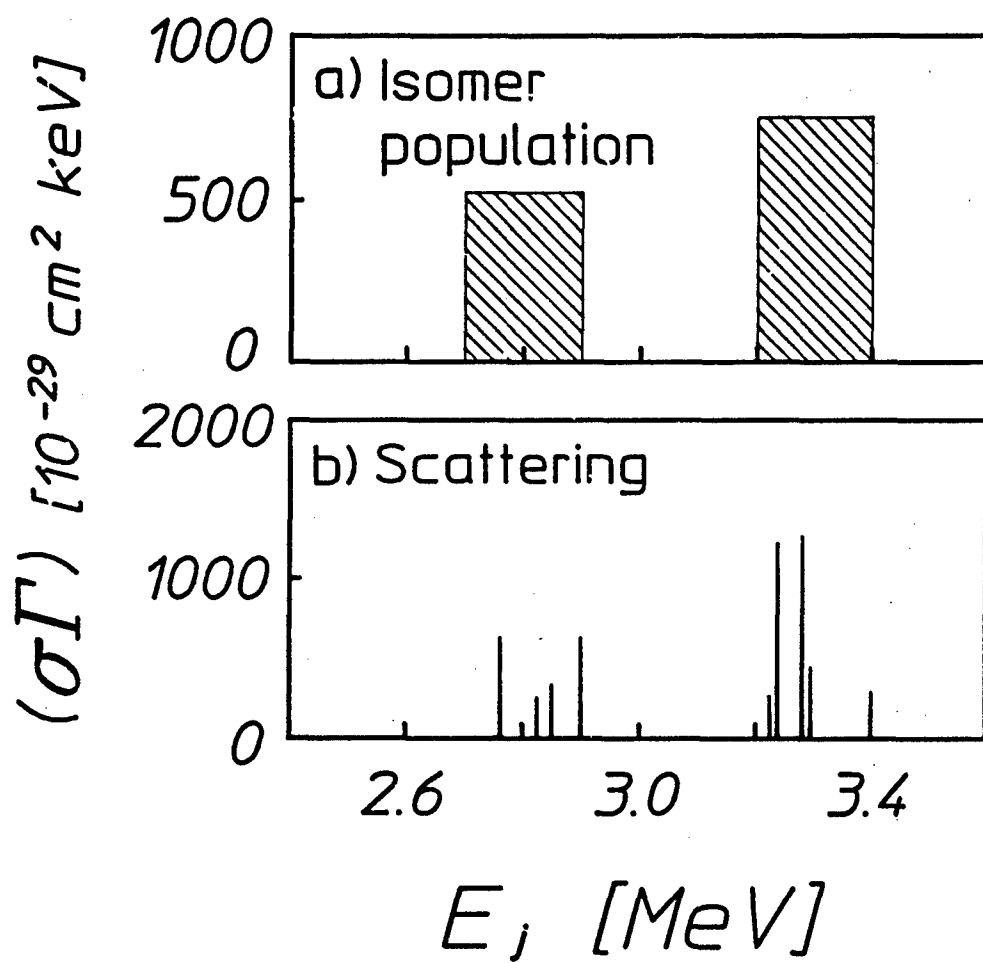


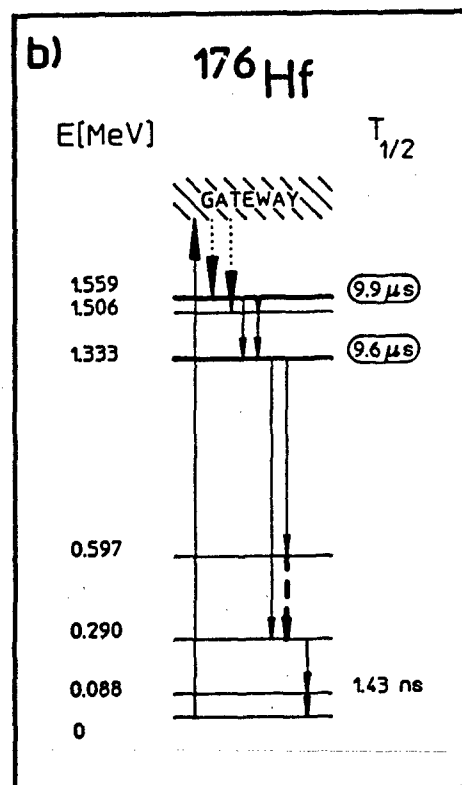
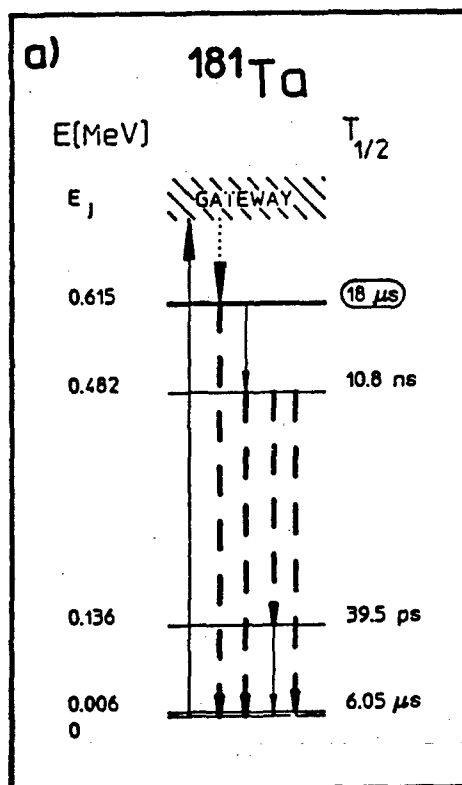


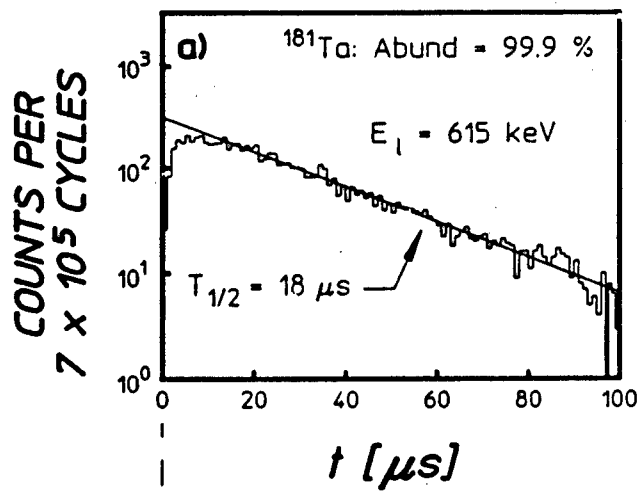




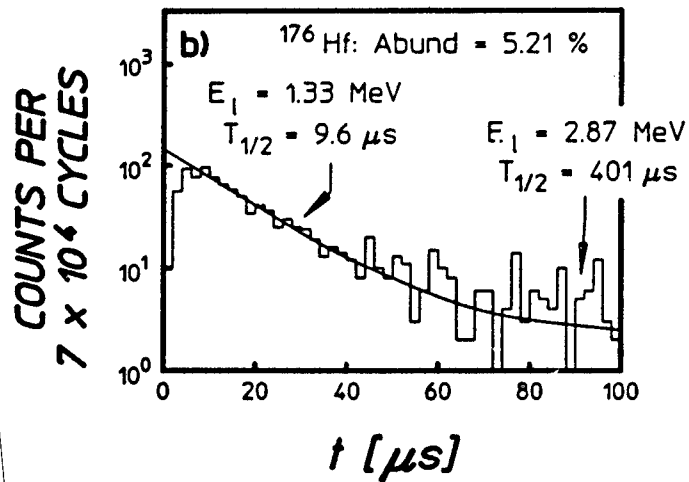
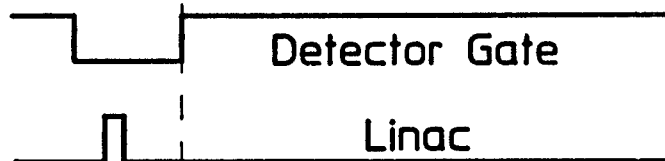




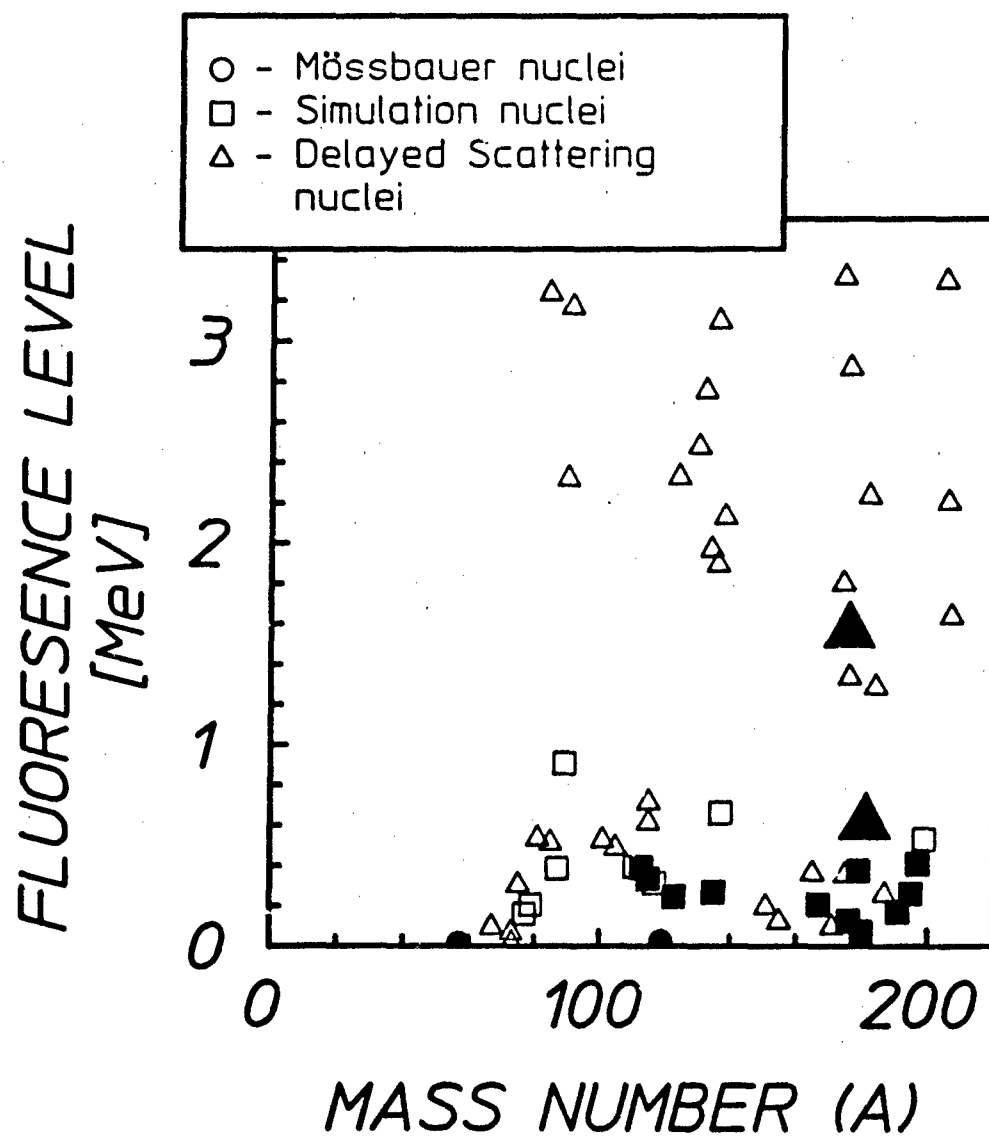




ON  
OFF  
ON  
OFF







## INSTALLATION OF THE TEXAS-X RESEARCH LINEAR ACCELERATOR

K. N. Taylor, C. Hong, T. W. Sinor, J. J. Carroll, J. D. Standifird,

B. W. Johnson, D. G. Richmond, and C. B. Collins

### INTRODUCTION

The previous chapter of this report reviewed the motivations and successes in studies conducted at the Center for Quantum Electronics on the feasibility of a gamma-ray laser. It was emphasized there that the next level of investigation would involve the study of isomers possessing laserlike nuclear states having lifetimes on the order of one to several microseconds and that this would be done with an in-house linac. The intent of the following material is to detail the various phases of the construction, installation, testing, optimizations and initial experiments that have gone into bringing the Texas-X research linear accelerator on line and into the fruitful research endeavors described here.

### UNDERGROUND FACILITIES AND INSTALLATION OF TEXAS-X

Preparations for installation and operation of the Texas-X linear accelerator began with construction of the dedicated shielding chamber which was designed for housing the device and constructed at university expense. Excavation for this construction began adjacent to the High Energy Laser Laboratory of the Center for Quantum Electronics on Nov. 7, 1991. Construction by a State of Texas agency is complex and highly regulated and the final designs for the building called for an underground facility that would derive its shielding capacity from both concrete and groundcover. With prevailing considerations of ground water and soil instability the foundation called for a pier and beam support structure reaching to bedrock (Figure 1). Following construction of the piers and a mud slab, the main floor, which was one foot thick and laced very heavily with reinforcement bars, was poured on Dec. 16, 1991. As seen in

Figs. 2 and 3, this was followed by construction of the walls, ceiling, and installation of conduits for power, accelerator control, and signal cables, etc. Toward the end of February 1992 soil had been moved into place about the walls and packed to attain proper densities for meeting the shielding specifications and temporary soil cover had been placed over the ceiling (Figs. 4 and 5). The final phases of construction occurred during March and early April of 1992. These included such items as electrical wiring, plumbing, installation of the air exchange system, heating and cooling devices, safety interlocks, and personnel safety alarms. Figure 6 shows an interior view of the chamber and also the future location of the accelerator (as demonstrated by the wooden simulation frame). Following sodding of the ground cover with bermuda grass, installation of a chain link fence enclosing the chamber was begun on April 10 (Figure 7). Tasks relating to cleanup and small oversights, etc., were completed in May, 1992.

Final acceptance of the accelerator system itself was completed during the spring and the device was shipped to the University of Texas at Dallas at the end of May 1992. Representatives from the manufacturer accompanied the system and supervised placement of its various components. As indicated in Fig. 8, the control console and modulator were separated from the underground accelerating unit and placed inside the main laboratory. The control unit was accessibly located inside the copper mesh screen room which also contains the controlling and processing electronics for the experiments. The modulator, which contains the power distribution system, switching elements and pulse forming network was placed near the door leading downstairs to the accelerator chamber. The cable run conducting the power pulses from the modulator to the linac is on the order of 50 feet. The process of installing, testing and adjusting the machine took approximately 3 to 4 weeks. The university began operation of the machine the last week of June. Characterization studies of its output began on June 23, 1992. Following these studies, as described below, an involved series of efforts was initiated to develop

an operating environment in which noise levels, and other concerns, permitted the observation of delayed nuclear emissions from target isomers possessing laserlike energy levels. This objective required the optimization, and even the development of technology, in three areas: the fluorescence detection system, EMI and RFI noise control, and data acquisition and processing.

### DETECTION SYSTEM

The critical core of the detection system for nuclear fluorescence was a fast scintillation crystal having a very low residual phosphorescence. After evaluating the many alternatives, the rather obscure CsF material was concluded to offer the best figure of merit when measured against these unusual requirements.

A CsF crystal having cylindrical dimensions of 2.5 cm diameter and length of 2.5 cm and coupled to an RCA 8850 photomultiplier tube served to detect the delayed fluorescent emissions from the target nuclei irradiated by the bremsstrahlung radiation from the linear accelerator. This combination of a fast scintillator and fast photomultiplier tube yielded a composite detector capable of fast speeds, good charge production and high gain.<sup>1</sup> Because of the typically short lifetimes concerned with in our work and, also, the expected high background count rates, CsF was chosen over the more popular, but slower NaI. The significant increase in count rate capability of CsF, whose principal decay constant<sup>2</sup> is 4.4 ns, over that of NaI (230 ns decay constant<sup>3</sup>) outweighed concerns over nearly commensurate losses in light output (CsF output<sup>2</sup> about 5 to 10 % of NaI). Furthermore, losses in energy resolution were of minor consideration due to the energy and temporal simplicity of the spectra being observed.

By far, the most intense emissions that the detection system had to contend with were those due to the nonresonant, Compton scattered photons produced during irradiation of the sample by the pumping x rays. Fortunately, the delayed nuclear fluorescence was temporally

resolved from the pumping pulse and a gating scheme designed to minimize the deleterious effects of the scattered radiation was implemented. Without gating the detector OFF during irradiation of the sample, the photomultiplier tube would be driven into saturation and premature deterioration of the photocathode would ensue. The scintillator itself cannot be gated, of course. Therefore, in order to minimize exposure of the scintillator to the scattered radiation a high degree of shielding and collimation was employed. These efforts helped minimize concerns about scintillator afterglow or phosphorescence<sup>4</sup> (another property for which CsF is superior to NaI).

The gating technique employed consisted of driving the focusing electrode of the photomultiplier tube into an OFF condition prior to each onset of a pumping pulse from the accelerator. At termination of the pulse, the operating potential of the focusing electrode was restored and normal operation of the photomultiplier tube resumed. This scheme is depicted in Fig. 9 in which it can be seen that an appropriately negative potential applied to the focusing electrode results in an effective OFF condition for the tube. Gating the focusing electrode<sup>5-10</sup> of an 8850 tube provides for a high contrast ratio (i.e., the quotient of the tube's ON gain to its OFF gain) and short gating transition times (on the order of 80 ns here).

An inherent drawback of gating a photomultiplier tube by direct switching of any of the electrode potentials is the generation of switching transients, caused by the capacitive coupling between the gated electrode and the anode of the tube, that may be inadvertently mistaken for signal photocurrents. In the case of an approximately rectangular gating pulse the corresponding transient output is a set of oppositely polarized spikes caused by differentiation of the original pulse. The precise shape of the transient output is, of course, determined by the shape of the gating pulse and the RC parameters of the differentiating output (which consists of the stray, coupling capacitance between the focusing electrode and the anode and the effective output

impedance of the detection system). Naturally, one seeks to minimize the effects of this output transient, and this can, in part, be done by adjusting, where possible, the parameters that influence its shape and magnitude. For fluorescent emissions sufficiently delayed, the gating transients do not present a problem.

### NOISE CONTROL

One of the most serious concerns to affect efforts directed toward detecting and measuring delayed fluorescent emissions is that of electrical interference<sup>11</sup> produced by the operation of the linear accelerator itself. This form of interference has directly influenced the nature of the processing electronics, the physical arrangement and nature of signal cables, and, in fact, all electrical elements involved in the collection, transmission and processing of the detected signal. The principal sources of electrical noise are the high current and high voltage pulses that propagate along transmission lines from the pulsed power source (i.e., the modulator) to the accelerator unit itself. These pulses are delivered into an unshielded network of wires and components adjacent to the accelerating section of the linac. It has not proven practical to provide individual shielding of the networks and a more tractable approach of shielding the signal collection system has been pursued.

Following efforts to minimize conductive interference via ground loops, etc., Fourier decomposition of the power pulses was undertaken and it was found that the principal spectral components had frequencies below several hundred kHz. Due to these relatively lower frequencies and the confining dimensions of the signal collection system the most significant propagated contributions to the electromagnetic noise were seen to result from the inductive components<sup>11,12</sup> rather than the radiative components of the field. These inductive components result from both magnetic and electric contributions. In an effort to identify the precise sources and

nature of this mode of interference the photomultiplier tube, which acts as a high impedance current source, was disconnected from the signal cable leading from the accelerator chamber to the processing electronics and replaced with a resistor across the input to the cable as shown in Fig. 10. Figure 11 shows the resulting peak noise amplitude detected at the processing end of the cable as the input impedance of the cable was increased. It is interesting to note that the signal does not extrapolate to zero for large input resistances but instead tends to a constant level. The nature of this dependence on impedance suggests that the primary concern with the photomultiplier tube connected to the system is electrostatic coupling.

An effective approach taken to decouple the signal system from the noise source was that of placing a large sheet of copper (5 ft. x 6 ft.) on the chamber wall from which the signal cables entered the room for connection to the detector output. With an appropriate aperture through which the cables could emerge, the sheet surrounded the terminating ends of the cables and thus presented a substantial baffle to interfering fields. A copper box was constructed over the aperture with bulkhead cable connectors mounted on it for connection to the cables from inside in the chamber. The thickness of the copper sheet (approximately 0.7 mm) was sufficient to account for the skin depths of the significant frequencies encountered in the noise spectrum. In addition to the electrostatic baffle, high quality, double shielded coaxial cable was employed for transmission of the signal. With the implementation of this scheme significant reduction of the noise could be demonstrated as seen in Fig. 12.

Further refinement of the signal received by the processing electronics was achieved by constructing and inserting a passive, 50 ohm bandstop filter having band edges at approximately 200 kHz and 1200 kHz (Figure 13). This filtering action enhanced the baseline restoration of the signal following termination of the accelerator power pulse and gating of the detector by removing contaminating components that contained little or no useful information.

The efforts described thus far have addressed the issues of enhancing the signal to noise ratio of the detector output by minimizing the rf noise contents of the signal. Another effort that tends toward the same end is to minimize contamination of the original photon signal by contributions from possible delayed, but unrelated, emissions from the sample itself or from environmental materials exposed to the bremsstrahlung pulse. As indicated in Fig. 14 the output of the accelerator was spatially defined by a collimator constructed of lead and having dimensions of 14 inches length and an exit aperture of 1 inch. The photomultiplier tube/CsF detector was contained inside a graded cylindrical housing constructed of copper, tin and lead. Radiation entering the photomultiplier tube housing was restricted by a 4-inch length of collimation that terminated at the face of the crystal. To minimize noise photons having energies less than about 200 keV a lead filter 1/16 inch thick was placed at the entrance to the detector collimator. The significance of this filter was that it could limit the input of low energy photons at all times and not just during the periods of signal input. This limitation would help minimize<sup>13</sup> any slightly residual effects of afterglow in the crystal due to the tremendous burst of scattered radiation occurring during the pumping phase of the cycle.

#### DATA ACQUISITION, CONTROL AND PROCESSING

The anode timing output from the 8850 tube was inserted into a double shielded coaxial cable that connected to the cover box on the chamber wall. This fed, in turn, to the double shielded 50 ohm cable mentioned earlier that led to the processing electronics housed in a copper mesh screen room. The pulse handling electronics were fast, 50 ohm devices designed for high pulse rate data sources (Fig. 15).

The block diagram shown in Fig. 15 illustrates both the logic layout for synchronizing and controlling the gating electronics and the signal processing and timing electronics used for



recording the timing spectrum of the decaying isomer. As seen in the diagram, the reference signal for initiating the gating process was derived from a synchronizing pulse provided at the modulator when the main thyatron was triggered into commutation. This analog pulse was converted to a TTL pulse with a nonretriggerable 74121 multivibrator chip. The TTL pulse then served as an external trigger for the DG 535 digital delay pulse generator. Two independent, logical outputs of the DG 535 were time-adjusted to initiate two independent sequences of events. The first of these events was that of triggering the HV pulse generator into producing a gating pulse for the focusing electrode of the photomultiplier. Upon arrival of this appropriately shaped negative pulse at the focusing electrode of the photomultiplier tube the ON bias at the electrode supplied by the dc power supply was canceled. The HV power supply maintained the normal +1800 V bias for the photomultiplier tube and the dc power supply biased the focusing electrode to an ON voltage of +650 V. The gating pulse was typically set to -820 V and had a typical width of 10 microseconds.

The second event triggered by the DG 535 output was the timing sequence for recording the decaying fluorescence spectrum being emitted by the irradiated sample. This timing sequence began with arrival of the START pulse from the DG 535 at the input of the time-to-amplitude converter (TAC). This signal was, of course, delayed until termination of the linac pulse and until any residual, nontractable noise had sufficiently decayed to acceptable levels. The TAC measured the time interval between arrival of the START pulse and a STOP pulse. The STOP pulse was derived from the processed signals coming from the detector output. With this technique only one timing count could be recorded per linac pulse. So the timing spectrum was accumulated over many cycles of linac operation. The output of the TAC (an analog signal whose amplitude is proportional to the measured timing interval) was fed into a multichannel analyzer whose response was calibrated to indicate time per channel. The method is similar to that of

delayed coincidence techniques except that here an artificial reference pulse, synchronized to the irradiation cycle, was used for initiating the timing sequence. The multichannel analyzer displayed counts vs time.

As indicated in the previous chapter, the success of the efforts, and the validity of the techniques described here have been beautifully demonstrated for the cases of  $^{181}\text{Ta}$  and  $^{176}\text{Hf}$ . Figure 16, reproduced from chapter one, demonstrates the delayed emissions obtained from the two isomers. The statistics and simplicity of the spectra were sufficient to allow derivation of the characteristic relaxation times by the straightforward slope technique frequently employed in delayed coincidence measurements.

#### ACCELERATOR MODIFICATIONS

Unfortunately, before isomers having shorter lifetimes could be studied, and prior to any further refinements of the data acquisition and processing systems, a sequence of severe waveguide problems which would eventually remove the accelerator from operation for a period of more than four months began to develop. Following approximately fifty hours of beam-time operation a loss of vacuum by the accelerator waveguide was incurred due to a failure of the electron beam exit window. This failure necessitated a return of the waveguide under warranty to the manufacturer for repair of the window. They elected to replace, as a normal course for such failures, the electron gun at the input end of the guide and to replace the previously .002 inch thick copper/beryllium exit window with .001 inch thick 310 stainless steel. Unfortunately, this window failed within one hour of operation following its return and installation. The machine was once again returned under warranty to the manufacturer. This time a major reconsideration of the failure modes of the exit windows was undertaken without cost to our contract. Following a substantial number of consultations with university personnel, outside

consultants contracted by the manufacturer, and their own staff, a reengineering effort was begun that would address three major issues relating to durability of the exit window. The first, and most significant of these, was the optimum thickness and material for the exit window. The second concerned the most practical cooling methods for the window and the third, which eventually involved reengineering the output, addressed the incorporation of a maintenance program in which the exit window could be replaced prior to failure.

The eventual selection of appropriate window material, and more importantly, window thickness was governed by failure modes that were critically dependent on the energy deposited in the window by the beam, by eddy currents driven by residual accelerating fields emanating from the resonant standing waveguide and by considerations of exit beam divergence caused by electron beam scattering within the window. The residual fields were removed from the drift space leading to the exit window by the incorporation of absorption pads designed for efficient operation at microwave frequencies. A more difficult problem to address was the dissipation of the excess energy deposited in the window by the pulsed electron beam. All three modes of heat transfer were considered as to their effectiveness in removing excess energy from the window. It was determined that efforts to maintain an oxide-free surface was very important for maintaining an optimum radiative component of heat transfer and that direct cooling of the surface with either water or a flow of compressed air was critical. The third method of heat transfer, viz., that of conduction, was perhaps the most significant in determining the optimum thickness of the window. Not surprisingly, opposing mechanisms strongly influenced the consideration of thickness. For example, the thicker the window, the greater the conductive removal of energy, but also the greater the deposition of energy by the electron beam.

After much consideration two proposals were presented to the university: (1) an exit window cooled by the direct flow of a 1 mm thick layer of water between two surfaces of

.002 inch thick layers of stainless steel and (2) a .003 inch thick copper/beryllium window cooled directly by a jet of compressed air and indirectly by a water cooled coil placed at the circumference of the window. The final selection from these two proposals was based on three considerations : (1) the effect on beam brightness (i.e., beam divergence), (2) the energy removed from the beam and (3) the final dose from the photon beam following energy conversion at the bremsstrahlung target. After tests performed on location at the manufacturing site in California by both the manufacturer and our university personnel the air cooled copper/beryllium window was chosen for final placement on the machine. This window was mounted on the reengineered output section of the guide that provided for routine maintenance of the accelerator by prescheduled replacement of the window.

As of this writing, shipment and reinstallation of the completed machine to the University of Texas at Dallas is imminent.

## REFERENCES

1. RCA 8850 Photomultiplier Tube Specifications Sheets (unpublished).
2. Introductory Nuclear Physics, First Edition, K. L. Krane (John Wiley & Sons, Inc., New York, 1988).
3. Harshaw/Filtrol Scintillation Phosphor Specifications Sheets (unpublished).
4. Scintillation Crystals Performance Specification Booklet (unpublished, Solon Tech. Inc.).
5. N. Klein and T. J. Rock, Rev. Sci. Instrum. 41, 1671 (1970).
6. D. G. Jameson and J. J. Martin, J. Phys. E. : Sci. Instrum. 8, 635 (1975).
7. T. M. Yoshida, T. M. Jovin and B. G. Barisas, Rev. Sci. Instrum. 60, 2924 (1989).
8. U. Fairnelli and R. Malvano, Rev. Sci. Instrum. 29, 699 (1958).
9. K. B. Keller and B. M. K. Nefkens, Rev. Sci. Instrum. 35, 1359 (1964).
10. B. L. Elphick, J. Phys. E. 2, 953 (1969).
11. Electrical Interference, Rocco F. Ficchi (Hayden Book Co. Inc., New York, 1964).
12. Principles of Electromagnetic Compatibility, Third Edition, Bernhard Keiser (Artech House Inc., 1987).
13. V. Ponomarev, A. P. Dubenskiy, V. P. Dubenskiy and E. A. Boykova, J. Phys. G. : Nucl. Part. Phys. 16, 1727 (1990).

## CAPTIONS

Figure 1: Pier drilling following excavation.

Figure 2: Installation of reinforcement bars for ceiling.

Figure 3: View of chamber from northeast with laser lab in left background.

Figure 4: Packed soil surrounding walls.

Figure 5: View from the east --- soil placed on top of chamber.

Figure 6: Simulation frame showing accelerator location inside chamber.

Figure 7: Posts installed for chain link fence.

Figure 8: Placement of accelerator system.

Figure 9: (a) PMT focusing electrode and dynode potentials in the ON and OFF states.  
(b) Corresponding gating voltage to focusing electrode.

Figure 10: Test arrangement for studying EMI.

Figure 11: Noise amplitude vs resistance for test system of Figure 10.

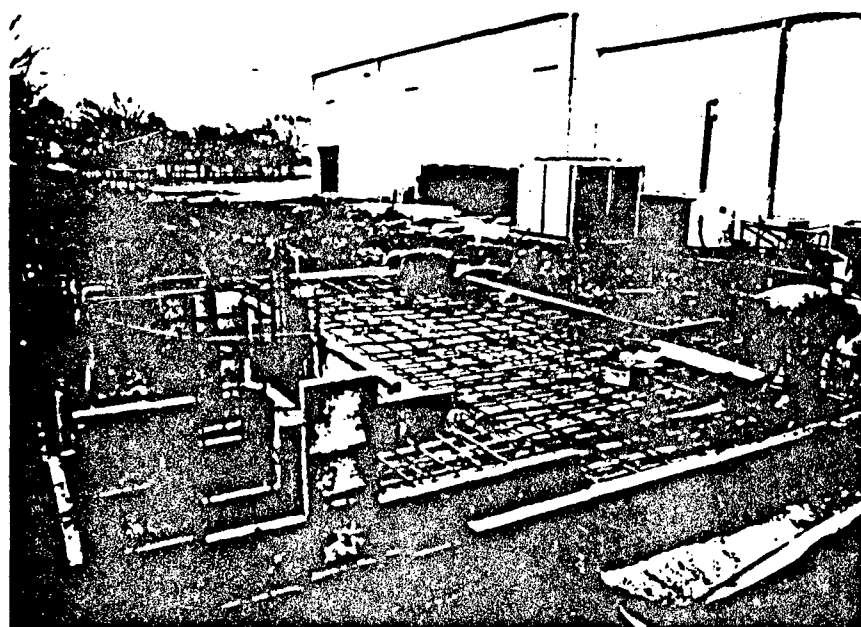
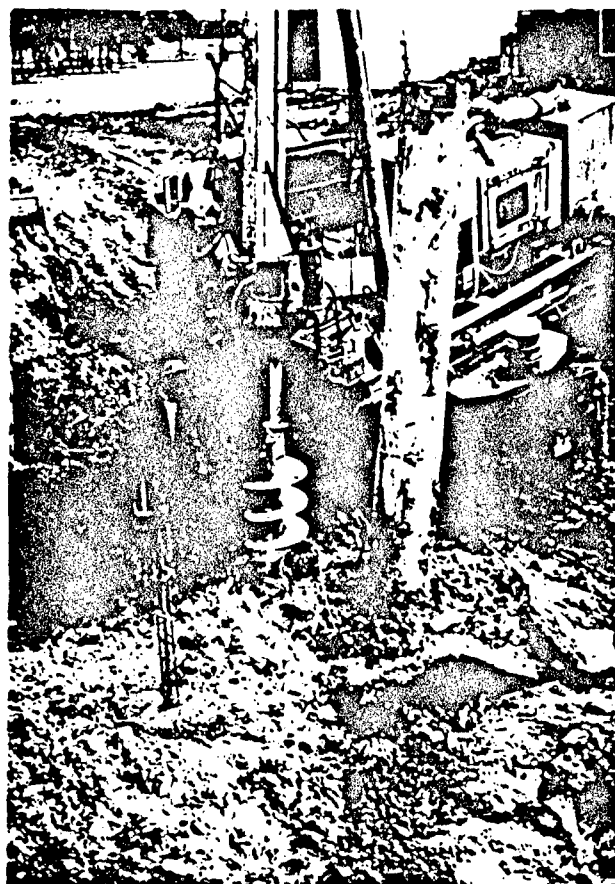
Figure 12: Noise levels into 50 ohm scope showing effectiveness of shielding. (a) Noise without copper sheet rf shielding and with common coaxial cable. (b) Noise without copper sheet rf shielding and with double shielded cable. (c) Noise with copper sheet rf shielding and with double shielded cable.

Figure 13: 50 ohm tee bandstop filter.

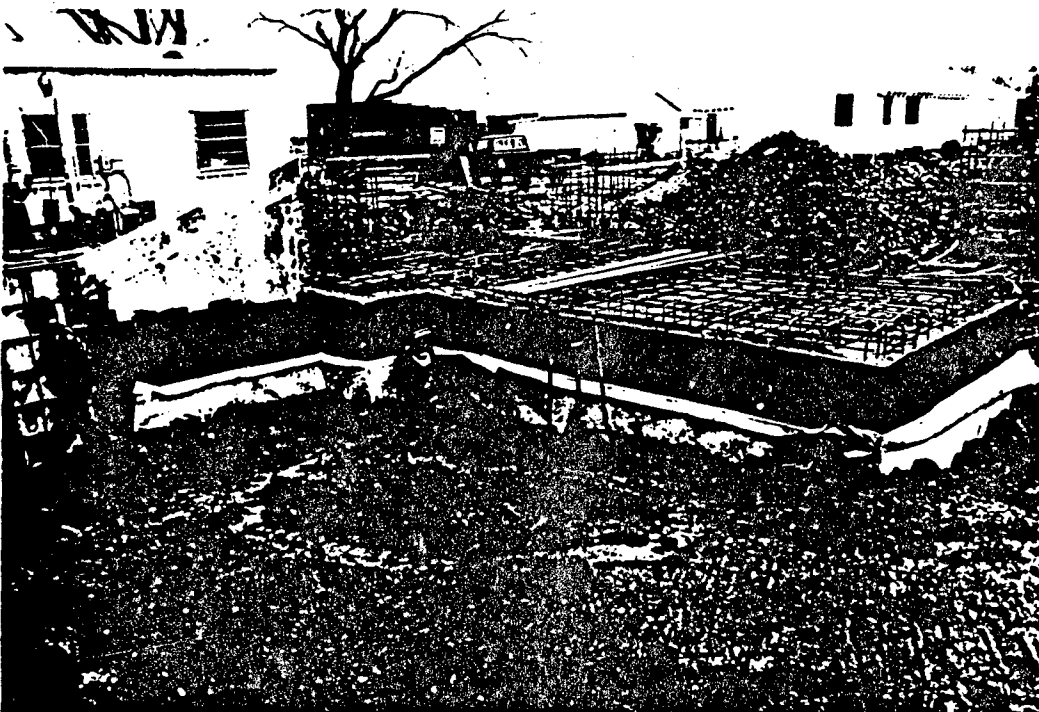
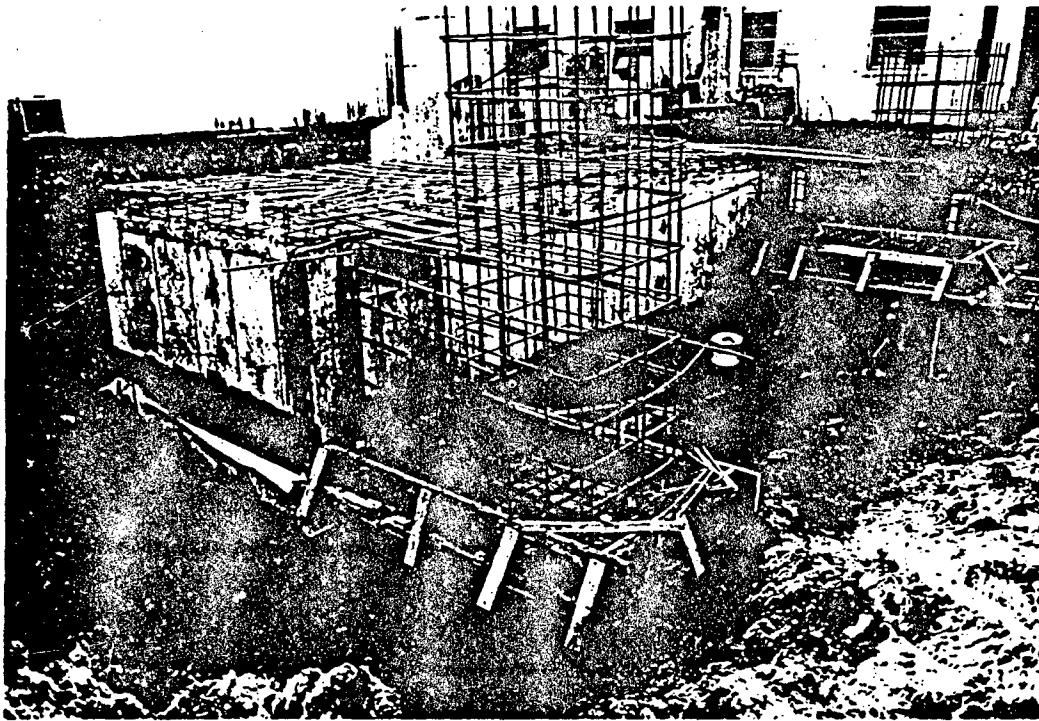
Figure 14: Experimental arrangement for detecting fluorescent emissions from irradiated sample.

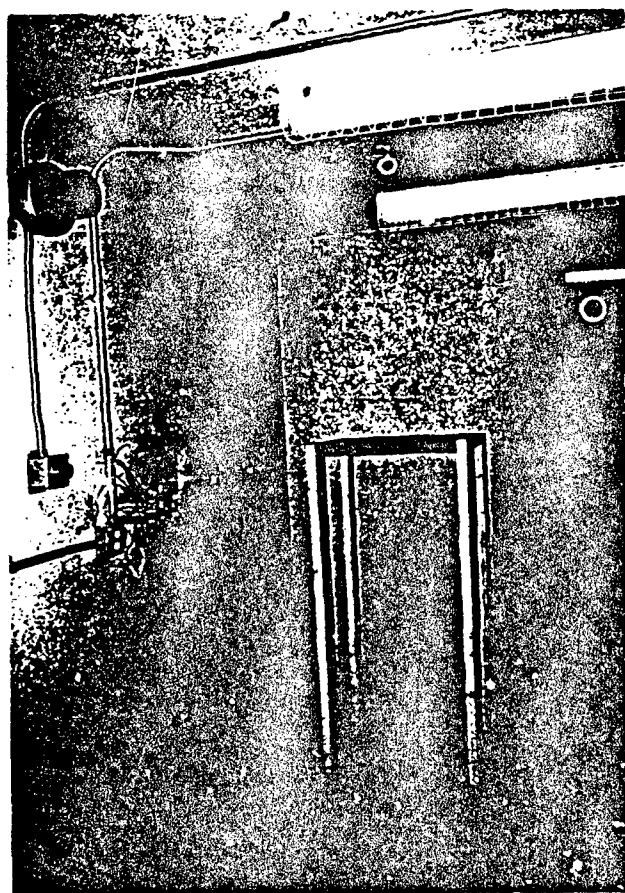
Figure 15: Block diagram for control and processing electronics.

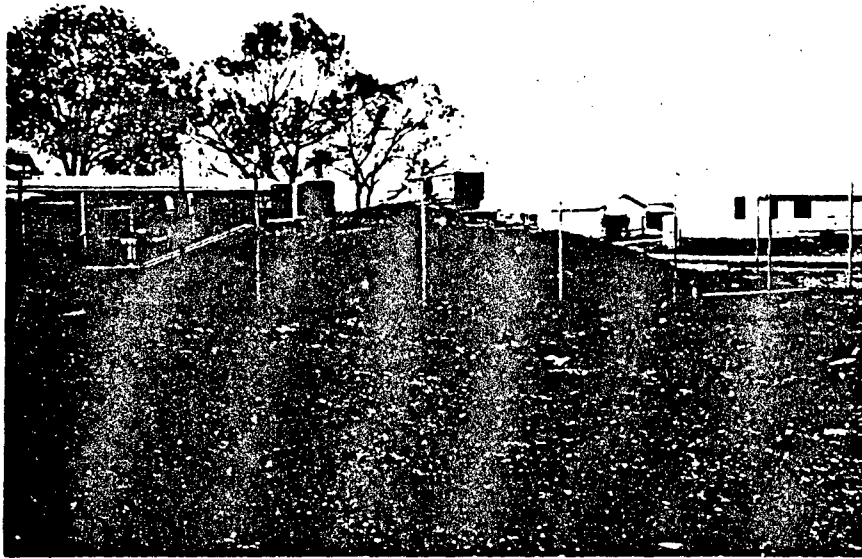
Figure 16: Timing spectra showing fluorescence from microsecond excited states of (a)  $^{181}\text{Ta}$  and (b)  $^{176}\text{Lu}$ .

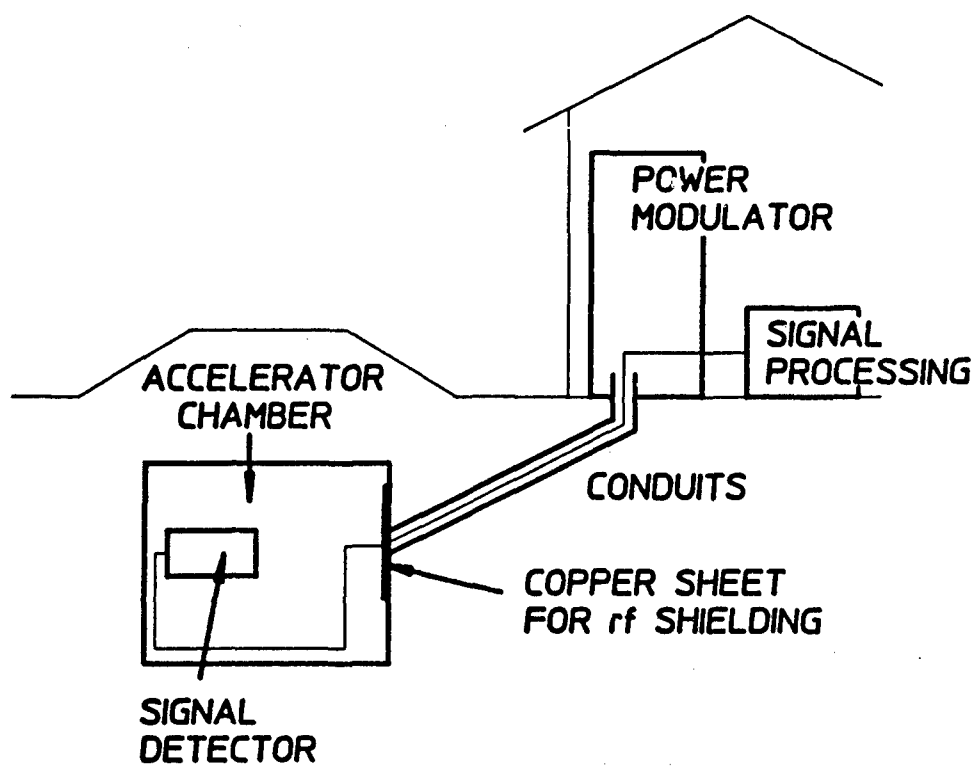


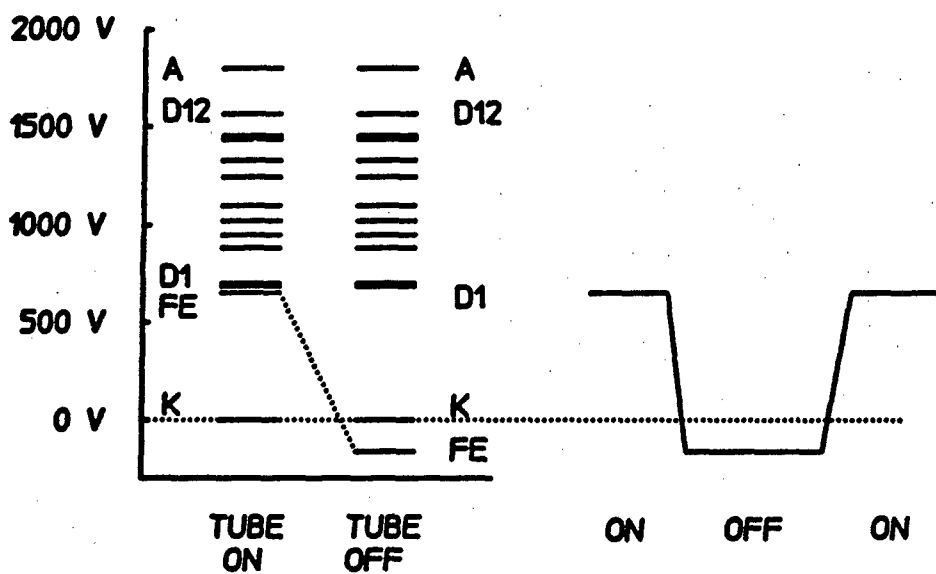






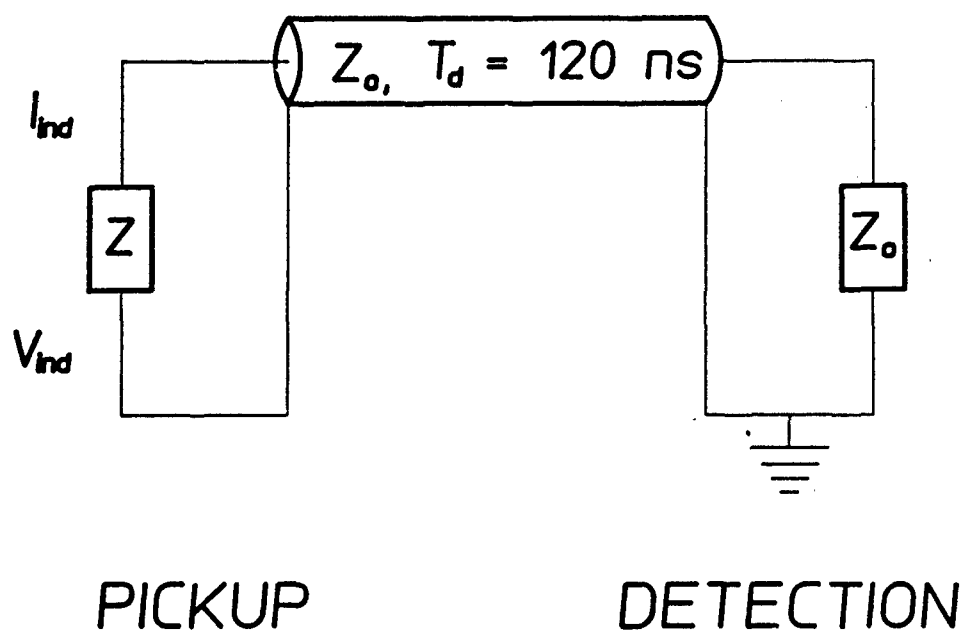


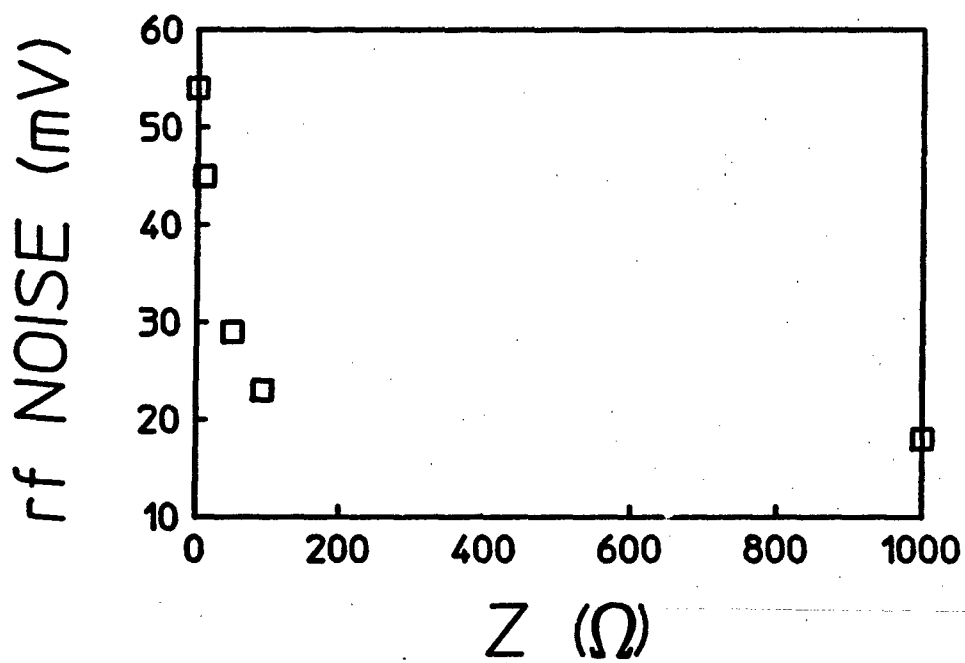


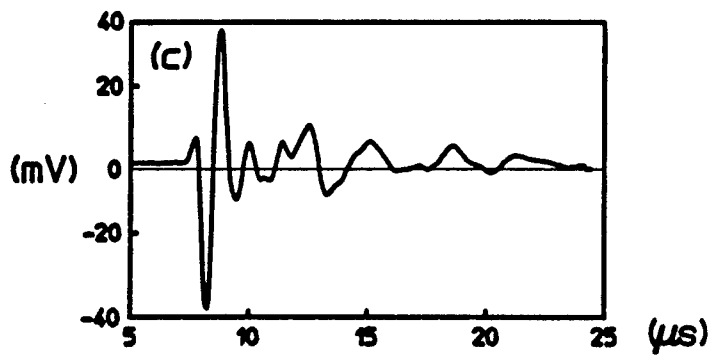
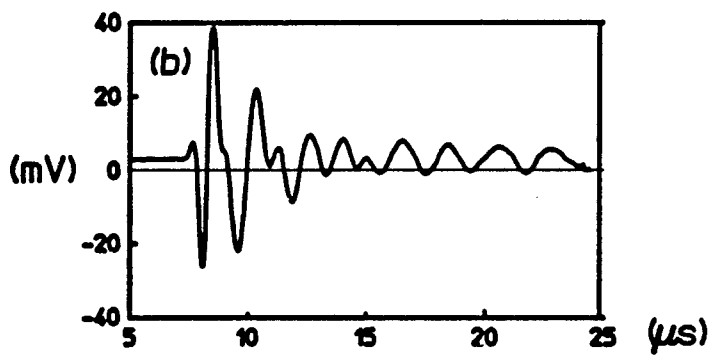
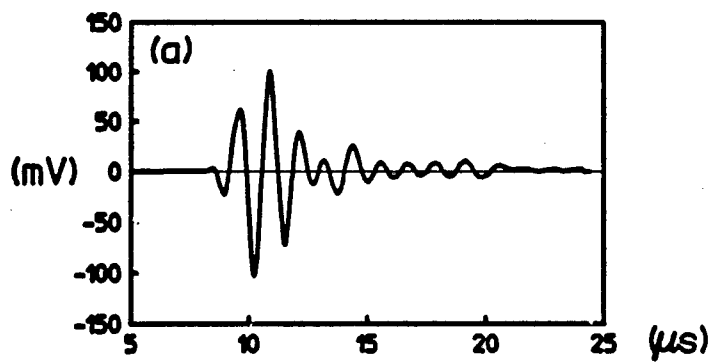


(a)

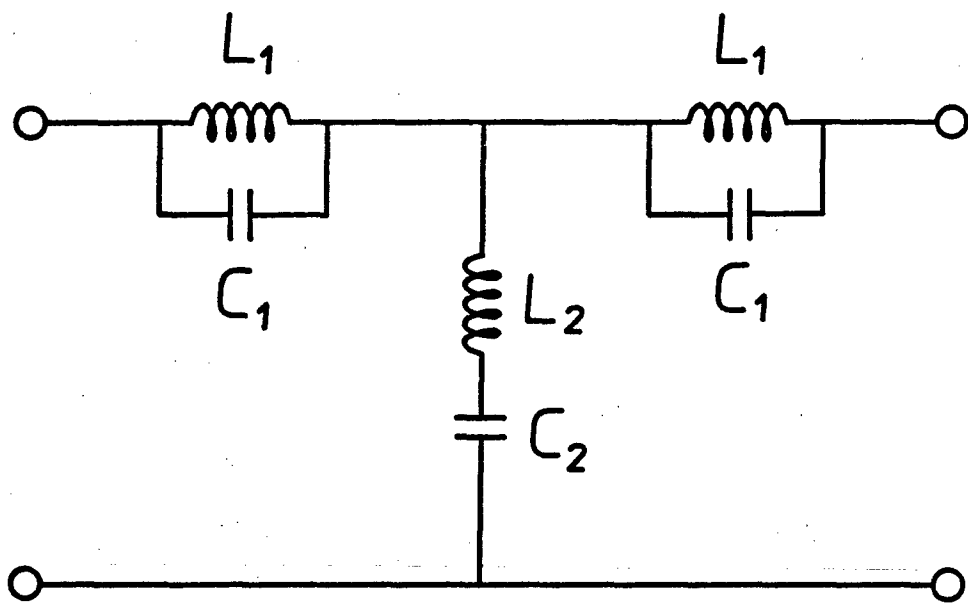
(b)

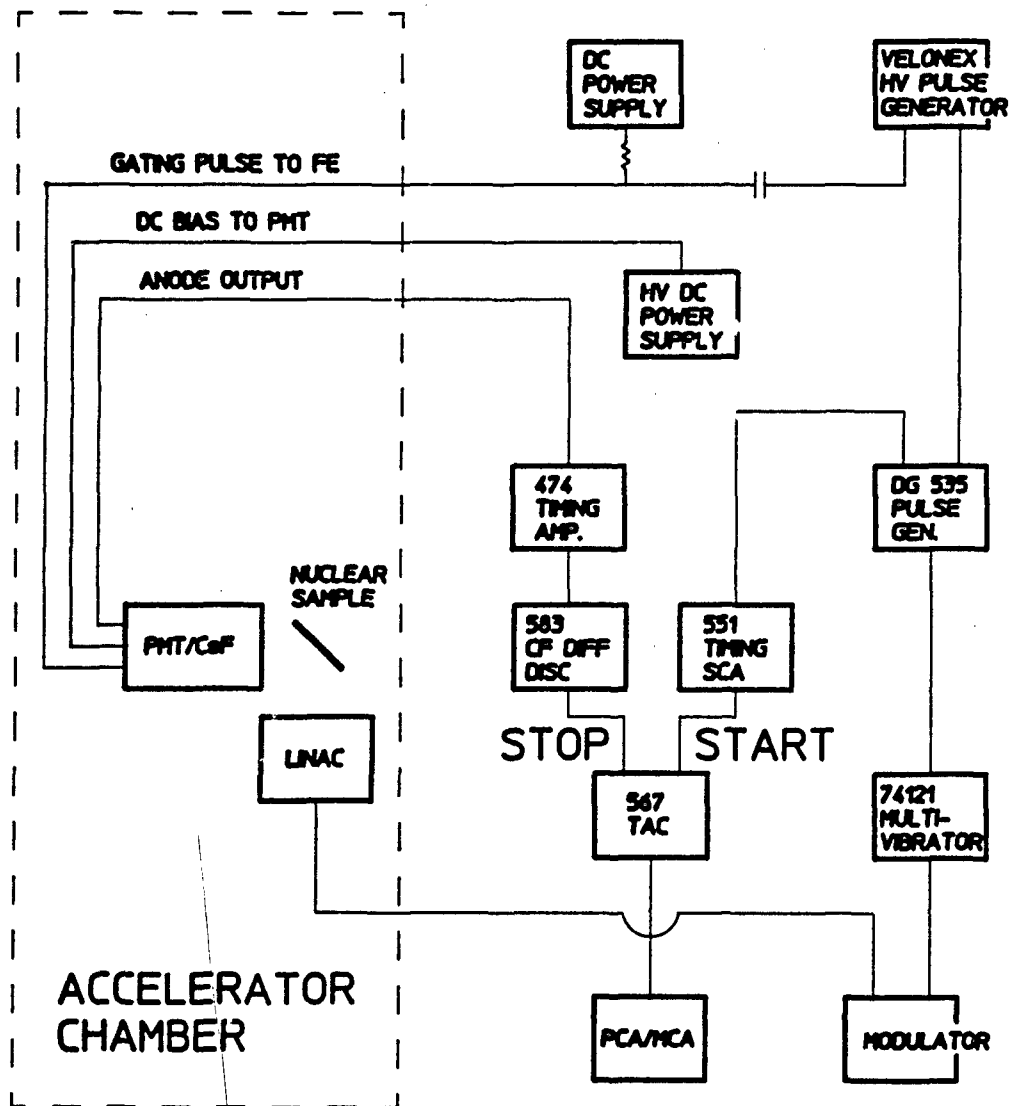


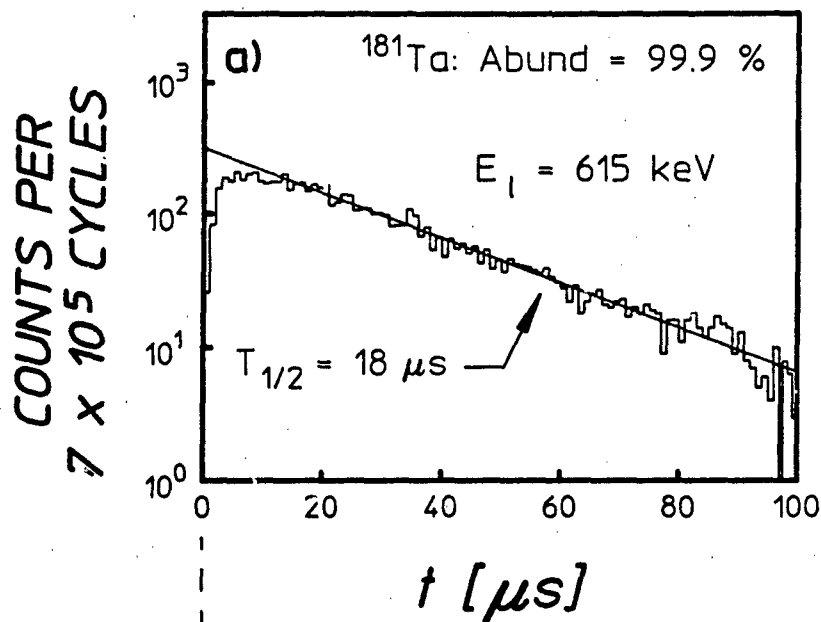










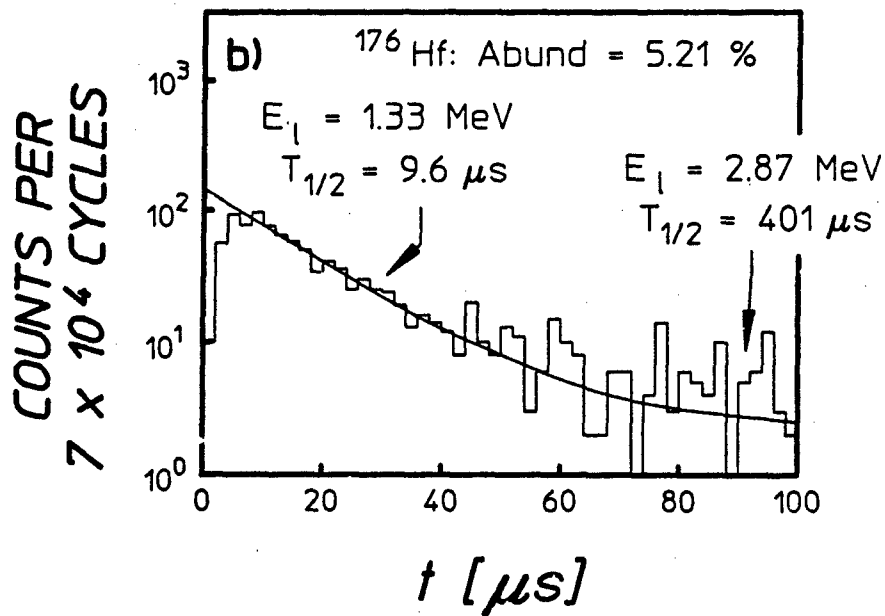


ON  
 OFF

Detector Gate

ON  
 OFF

Linac



ABSOLUTE MEASUREMENT OF SPATIAL AND SPECTRAL CHARACTERISTICS  
OF BREMSSTRAHLUNG BY THE PHOTOEXCITATION OF NUCLEAR ISOMERS:  
CALIBRATION OF THE TEXAS-X

J. J. Carroll, D. G. Richmond, T. W. Sinor, K. N. Taylor,

C. Hong, J. D. Standifird and C. B. Collins

INTRODUCTION

Linear electron accelerators (linacs) and pulsed power e-beam devices have become indispensable as sources of bremsstrahlung for a wide variety of applications. Linacs are now common in medical radiology,<sup>1</sup> nuclear physics<sup>2</sup> and industry<sup>3</sup> for the irradiation of a broad range of materials. The uses of e-beam devices are less familiar but no less important and large machines are employed extensively as nuclear simulators<sup>4</sup> to test the effects of radiation on electronics and other hardware. They have also been used for nuclear physics research.<sup>5</sup> These diverse applications and their procedures have been established over a period of years yet there remains a common impediment to the use of such intense photon sources. This is the difficulty in accurately and directly measuring the spectral properties of the bremsstrahlung needed to calibrate the output of the accelerator or pulsed-power machine.

Many techniques have been developed for the characterization of bremsstrahlung, the most prevalent of which is based upon traditional measurements of the dose of absorbed radiation. This quantity is routinely and accurately measured<sup>1</sup> with ionization chambers or thermoluminescent dosimeters (TLD's) for either flash or continuous exposures. Since the dose can be a useful indicator of the overall photon flux it is the basis of calibration procedures employed in most medical and industrial applications and in monitoring the radiation produced by nuclear simulators.<sup>6</sup> However, dose is a convolution of the photon spectrum with appropriate absorption

coefficients which depend upon wavelength<sup>1</sup> so it is not possible to explicitly determine the energy distribution of the bremsstrahlung. Instead the usual practice<sup>7</sup> is to use dose measurements to normalize spectra computed with sophisticated Monte Carlo codes<sup>8-10</sup> such as EGS4, GEANT or TIGER. This procedure is most suspect when used for e-beam devices<sup>6</sup> since the simulations rely heavily upon difficult to measure voltage and current profiles which are needed as input parameters. An improvement on traditional dose methods has been devised<sup>11</sup> in which a set TLD's are irradiated which are enclosed within small spheres of assorted materials like aluminum and depleted uranium. The dosimeters register various measurements attenuated by the shielding provided by the "differential absorbers" and these values are deconvolved to give the spectrum of the incident radiation. This method has been effectively<sup>11</sup> used to characterize bremsstrahlung flashes from e-beam devices but it cannot provide information for photon energies above about 1 MeV for which there is little variation in the transparency of the absorber materials. The form of the spectra obtained is also quite sensitive to the initial shape assumed in the calculation.

Other techniques are available which provide spectral characterizations of MeV bremsstrahlung but even the simplest of these is seriously limited in its usefulness. The most straightforward approach<sup>12</sup> is to allow a well-shielded detector placed at a large distance from the photon source to observe a greatly diminished flux through a pinhole collimator. With this arrangement the energy distribution can be directly measured as a pulse-height spectrum. However, in addition to the requirement of a large working environment, long exposures are needed for the accumulation of reasonable statistics that cannot be achieved with most low duty cycle e-beam devices. A more complex method<sup>13</sup> is that of nuclear resonance fluorescence (NRF) which provides an excellent means of calibrating bremsstrahlung spectral by using  $(\gamma, \gamma')$  reactions to inelastically scatter large numbers of photons from gram-sized targets. The incident spectral

intensity is obtained at discrete excitation energies from known reaction cross sections. Yet NRF procedures are limited by the large amount of shielding needed for detectors that observe the scattered photons in real time and the necessity of long continuous exposures. Compton spectrometers are also quite useful but require simple irradiation geometries<sup>14</sup> and are often large and expensive.<sup>15</sup> Finally there are photoactivation methods that rely on the detection of fluorescence from  $(\gamma, n)$  reaction products. Samples are irradiated with either continuous bremsstrahlung or flashes of x rays and are transported to a quieter environment for counting. However, few isotopes permit this type of reaction at incident photon energies<sup>16</sup> below 4 MeV so this method has no utility for calibrating many bremsstrahlung sources. Despite the variety of characterization techniques available there is a clear and present need for a new approach which is equally applicable for the calibration of linacs and e-beam devices. It should also be sensitive to photon energies up to several MeV and be simple and portable in its implementation.

The X-ray Activation of Nuclei (XAN) procedure is ideally suited to meet this need while avoiding the problems inherent in other methods. The fundamental concept<sup>17</sup> was first suggested in the 1940's but has only been applied in the quantitative fashion of XAN since 1987, primarily for the characterization of flashes of x rays from large pulsed-power machines.<sup>18-22</sup> This basic idea is similar to that of NRF in that nuclear transitions are used to measure the spectral intensity of bremsstrahlung at discrete excitation energies. However, in NRF scattered gamma rays are detected in real time at intensities that are only slightly above a dominant Compton background.<sup>23</sup> In XAN the focus is on the detection of fluorescence from exceptionally long-lived nuclear states called isomers which are produced by  $(\gamma, \gamma')$  reactions so it is not necessary to count samples in situ. Instead targets containing isomeric nuclei in their ground state are irradiated and then transported either pneumatically or by hand to a simple gamma-spectrometer system. With half-lives ranging from seconds to hours, populations of nuclear isomers sample

bremsstrahlung spectra and effectively store the information for convenient retrieval. The equipment and samples needed to implement XAN are relatively inexpensive, portable and reusable and the target package occupies very little space in the irradiation environment.

In the past XAN has been primarily applied<sup>19-21</sup> to the characterization of bremsstrahlung with photon energies no higher than about 1.5 MeV due to the paucity of information on ( $\gamma, \gamma'$ ) reactions which populate isomers. Recently the nuclear database has been expanded by a series of investigations<sup>23-25</sup> of the photoexcitation of the isomers of <sup>79</sup>Br, <sup>87</sup>Sr, <sup>115</sup>In and <sup>137</sup>Ba. Thus it has been feasible to extend the applicability of XAN up to energies approaching 4 MeV, making it possible to calibrate a wider range of photon sources. The utility of this approach was demonstrated by the measurement of spatial and spectral distributions for bremsstrahlung produced by the Texas-X research linac at the University of Texas at Dallas.

#### THEORETICAL BACKGROUND

The irradiation of a sample containing  $N_T$  target nuclei in some initial state by bremsstrahlung results in a population of  $N_f$  nuclei in a given final state according to

$$N_f = N_T \int_0^{E_0} \sigma(E) \frac{d\Phi(E)}{dE} dE, \quad (1)$$

where the photon continuum is described by an endpoint  $E_0$  that equals the electron energy and a time-integrated spectral intensity function  $d\Phi(E)/dE$  that gives the photon flux per unit energy bandwidth. The excitation reaction is described by the energy dependent cross section  $\sigma(E)$ .

The XAN technique is based on the photoexcitation of nuclear isomers which are metastable due to the large multipolarities required for their electromagnetic decay to levels at lower energies.<sup>26</sup> This also inhibits the inverse process so isomers are not significantly excited by direct

absorption transitions from the ground state. Instead at energies below the photoneutron threshold, isomers are produced by the two step process illustrated in Fig. 1 in which an incident photon designated by  $\gamma$  is resonantly absorbed by a higher-lying level. The metastable level is then populated by a branch of the decay cascade from the intermediate, or "gateway" state with promptly emitted photons being the  $\gamma'$ . This process is equivalent to bandwidth funneling which is so familiar in laser physics. The standard notation for this reaction is  $X(\gamma, \gamma')X^m$  in which  $X$  and  $X^m$  represent the participating nucleus in its ground and isomeric states, respectively. It has been demonstrated experimentally<sup>23</sup> that gateways are well separated and have widths that are large on a nuclear scale but small compared to the structure of broad bremsstrahlung continua. Since the spectral intensity is a constant over each gateway, Eq. 1 reduces to

$$A = \frac{N_I}{N_T} = \sum_j (\sigma\Gamma)_j \frac{d\Phi(E_j)}{dE} \quad (2)$$

where the fractional activation,  $A$  has been introduced and

$$(\sigma\Gamma)_j = (\pi b_a b_o \sigma_0 \Gamma / 2)_j \quad (3)$$

is the integrated cross section for production of the isomer through the  $j^{\text{th}}$  gateway having an excitation energy  $E_j$ . For each intermediate state the integration is performed over a Lorentzian lineshape having the natural width of the level,  $\Gamma = (\hbar \ln 2)/T_{1/2}$  with  $T_{1/2}$  being its half-life. The summation in Eq. 3 includes all gateways whose excitation energies are less than the bremsstrahlung endpoint. In the process depicted in Fig. 1 the probabilities that a gateway will decay directly back to the ground state and either directly or by cascade to the isomer are  $b_a$  and  $b_o$ , respec-



tively. The quantity  $\sigma_0$  is one half of the peak cross section for the absorption resonance and is given by the Breit-Wigner formula<sup>27</sup>

$$\sigma_0 = \frac{\lambda^2}{2\pi} \frac{2I_j + 1}{2I_g + 1} \frac{1}{\alpha + 1}, \quad (4)$$

in which  $\lambda$  is the wavelength of the incident photon,  $I_j$  and  $I_g$  are the angular momenta of the gateway and ground states, respectively, and  $\alpha$  is the internal conversion coefficient for the absorption transition.

In the most ideal implementation of XAN several isomeric nuclides would be chosen, each of which possessed only one gateway which satisfied the condition  $E_j \leq E_0$ . The summation of Eq. 3 would then reduce to a single term. If integrated cross sections were available in the literature for these gateways either as direct evaluations or from the quantities in Eqs. 3 and 4, it would be a simple matter to obtain the incident spectral intensity at each of the  $E_j$  from measured activations. Unfortunately the nuclear data only supported the identification of one isotope,  $^{137}\text{Ba}$  which fulfills this criterion for  $E_0 \leq 4$  MeV. Other isomeric nuclei whose lifetimes and fluorescence energies were convenient for measurements and whose gateway structures were well known all possess multiple intermediate states. Thus it was necessary to employ a more complex procedure to determine the spectral distribution of bremsstrahlung. This approach will be discussed in a later section. The isotopes used in this work were  $^{79}\text{Br}$ ,  $^{87}\text{Sr}$ ,  $^{115}\text{In}$  and  $^{137}\text{Ba}$  and their relevant parameters are listed in Table I.

## EXPERIMENTAL DETAILS AND RESULTS

### General

Irradiations were performed with bremsstrahlung from the Texas-X research linac recently installed at the University of Texas at Dallas. The Texas-X was designed to produce nominal 4 MeV electrons in pulses of 2.78  $\mu$ s duration with a repetition rate of 360 Hz. This gave a duty cycle of 1/1000 and a time integrated current of 150  $\mu$ A for the exposures used in this work. The accelerator was emplaced in an underground facility with internal dimensions of 2.6 m height, 7.3 m length, and 2.9 m width. Only the magnetron/wave-guide assembly resided in the chamber and this was oriented such that the electron beam propagated horizontally along the long dimension at a height of 1.4 m from the floor. The electrons exited the modified Varian waveguide through a 2 mil (51  $\mu$ m) window composed of a 9:1 alloy of Cu and Be. Bremsstrahlung was produced by electrons that impinged normally on a 2.5 cm x 2.5 cm, 3 mm thick tantalum converter held within a large water-cooled copper jacket. The converter was located 2.7 cm from the exit window.

### Preliminary Measurements

Measurements were made of the properties of the electron beam prior to irradiating nuclear targets. Stopping range experiments were performed using aluminum, copper and graphite sheets of different thicknesses as attenuators. Electrons passing through these filters were collected by an aluminum block and the excess charge was recorded from the voltage across a 50  $\Omega$  load using an oscilloscope and trace digitizing software. Typical data obtained using aluminum attenuators are shown in Fig. 2a and plot the charge delivered to the collector during each pulse as a function of filter thickness in  $\text{g cm}^{-2}$ . An extrapolated range of 2.19  $\text{g cm}^{-2}$  was obtained from these data and tables in the literature<sup>28</sup> indicated that this corresponded to an

electron energy of 3.55 MeV. The average of values determined from experiments conducted with different materials gave  $E_0 = 3.6 \pm 0.1$  MeV.

The spatial profile of the electrons was measured by using a 10 cm x 10 cm, 2 cm thick aluminum plate to scan across the beam. This plate was oriented so that its large area faced the exit window at a distance of 2.7 cm. Figure 2b plots the collected charge as a function of its relative horizontal position and this varied from zero when no part of the beam was intercepted to a maximum when all electrons were stopped. The best fit to these and similar data obtained by vertical scans was a Gaussian having a radial half width of 0.69 cm. This defined the electron spot size at the entrance plane to the converter and the half angle for the electron divergence,  $\theta_e = 13.5^\circ$ . The beam axis was determined from scans conducted at various distances from the exit window and a small HeNe laser affixed to a stable platform was used to identify the axis for further experiments.

#### Bremsstrahlung Spatial Distribution

Although the strength of XAN lies in its ability to provide spectral characterizations of bremsstrahlung, spatial distributions can also be obtained. In this work the axial dependence of x rays from the Texas-X was investigated by using metallic indium disks 1.0 cm in diameter and 0.127 mm thick as well as plastic planchettes 5.0 cm in diameter and 0.8 cm thick containing  $\text{BaF}_2$  in powder form. In each case the calibration isotopes of  $^{115}\text{In}$  and  $^{137}\text{Ba}$  were present in their natural abundances. The samples were oriented to face the beam and were placed at various distances along the beam axis. Following their irradiation the targets were transported by hand to a standard NaI(Tl) spectrometer system to obtain pulse-height spectra. A typical example is shown in Fig. 3 for an indium sample exposed for 15 min and counted for 5 min. The fluorescence signature<sup>29</sup> of the decay of  $^{115}\text{In}^m$  was the large photopeak at 336 keV while the

smaller peak to its right resulted from the decay of a less well characterized isomer,  $^{113}\text{In}^m$ . Fractional activations were determined from the measured numbers of counts in the full-energy peaks using standard corrections for the finite lifetimes of the isomers, the detection and emission efficiencies and the transparencies of the samples to the fluorescence gamma rays. This last correction factor was computed by a simple Monte Carlo code that was tested to insure that samples of identical mass but in different configurations would give the same activation.

Fractional activations normalized to irradiation time for the indium and barium samples are shown in Fig 4. The data are plotted as functions of  $R^{-2}$  where  $R = z - z_0$ ,  $z$  is the axial distance from the converter and  $z_0$  is an offset included to account for the extended nature of the photon source. The expected behavior was observed in the measurements and in the results of EGS4 simulations of the photon flux passing through the sample areas. The offset was found to be  $z_0 = -(2.5 \pm 0.5)$  cm which coincided with the location of the CuBe exit window.

The radial dependence of the bremsstrahlung was determined by irradiating a set of thin (0.127 mm) indium samples at several axial distances. These foils were fashioned in the form of concentric annuli in radial increments of 0.5 cm and a circular central target 1.0 cm in diameter. A total diameter of 8.0 cm was covered by the set of eight samples. The total photon flux striking each annulus was taken to be well represented by the fractional activation of each sample due to the division by  $N_T$  in Eqs. 1 and 2. This was justified because the number of target nuclei was directly proportional to the mass and therefore to the area of each sample. It was assumed that there was no significant variation in spectral content across the annuli. Radial distributions mapped in this way are shown in Fig. 5 and indicate the beam profiles at each axial position at which samples were irradiated. Profiles at  $z \geq 5$  cm were described by Gaussians whose halfwidths were proportional to  $R^{-2}$ . To display the information in a more familiar form the radiation lobe

was obtained by connecting values of a given relative intensity in the radial profiles. The shape of this lobe evidenced the expected qualitative behavior for thick target bremsstrahlung<sup>30</sup> and a half angle for the photon intensity was found to be  $\theta_{\text{tot}} = 23^\circ$ . This was in excellent agreement with the sum of  $\theta_c$  and the mean angle for the emission of bremsstrahlung from colinear relativistic electrons,<sup>30</sup>

$$\theta_m = \gamma^{-1} = (29^\circ)/E_0 \quad (6)$$

Here  $\gamma$  is the relativistic gamma factor and the electron energy is expressed in MeV. For 3.6 MeV electrons,  $\theta_m = 8.06^\circ$  giving  $\theta_{\text{tot}} = 21.6^\circ$ .

Spatial distributions were also obtained from dose measurements made with an ionization chamber whose calibration was traceable to NIST and are shown in Fig. 6. Again the expected axial dependence was observed and the angular dose profile determined at a distance of 60 cm from the converter was in good agreement with that given by fractional activations and by a Gaussian function with a half angle of  $22^\circ$ .

#### Bremsstrahlung Spectral Distribution

The spectral distribution was examined by irradiating the full set of the calibration nuclides listed in Table I. Planchettes containing the compounds  $\text{BaF}_2$  and  $\text{SrF}_2$  in powder form and an indium disk were exposed for times on the order of 15 min and transported by hand from the linac chamber to the spectrometer system. In the case of the bromine isotope the short lifetime (4.9 s) necessitated the pneumatic transfer of a cylindrical sample 5.0 cm in length and 1.0 cm in diameter containing LiBr through a plastic tube to a NaI(Tl) well scintillator. The "rabbit" was irradiated axially for 20s. Additional electronics were used to initiate its transport by turning on a standard shop vacuum and to signal its arrival in the detector well, thereby beginning the acquisition of a pulse-height spectrum. As outlined before, fractional activations normalized to

the exposure times were determined from the fluorescence observed. These values are listed in Table II and were normalized to an axial position of  $R = 30$  cm.

The application of Eq. 2 to the  $^{137}\text{Ba}$  datum yielded a spectral intensity of  $(8.96 \pm 0.62) \times 10^6 \text{ cm}^{-2} \text{ s}^{-1} \text{ keV}^{-1}$  at  $E_j = 3.2$  MeV. Prior to proceeding with the complete analysis it was instructive to see to what degree the endpoint could be determined by a simple approach. Assuming that only the large gateway at 2.7 MeV produced the measured activation for  $^{87}\text{Sr}^m$ , the spectral intensity at that energy was found to be  $2.1 \times 10^7 \text{ cm}^{-2} \text{ s}^{-1} \text{ keV}^{-1}$ . An uncertainty was not assigned to this value due to the nature of the approximation. It was expected that the energy dependence near the endpoint of the spectrum could be described as a linear function since photons in this region were for the most part due to single interactions within the converter. This is the basis of the traditional Kühlenkampff approach.<sup>31</sup> Following this idea, a linear fit was made to the spectral intensities obtained above and gave an endpoint energy of 3.58 MeV, in remarkable agreement with the results of electron stopping measurements.

The determination of bremsstrahlung spectral intensity in XAN is equivalent to solving a system of equations. Unfortunately in this application the nuclides of Table I possessed a total of twelve gateways giving an equal number of unknowns (at each of the  $E_j$ ) while there were only four equations available from the measured activations. Although this could not be solved exactly, an iterative procedure was used to obtain the spectrum. The basic strategy was to employ a simplified gateway mesh to arrive at successive approximations to the spectrum, working from the known value fixed by the  $^{137}\text{Ba}$  activation towards lower energies. Convergence was tested at each step by using a fitted energy distribution to calculate expected values for the fractional activations of the calibration isomers and comparing these with the measurements.

The only assumption made regarding the spectral shape was that the natural logarithm of the energy distribution was smoothly and slowly varying and could be represented well by a low-order polynomial above about 0.5 MeV.

The simplified gateway mesh was defined by the five bands shown in Fig. 7. The choice of the groupings was obvious for those intermediate states lying near 3.25, 2.75 and 0.76 MeV but the remaining gateways were more evenly spaced and were simply divided into two bands at 1.25 and 1.82 MeV. These energies were averages of the  $E_i$  for the included states, weighted by the relative sizes of their integrated cross sections which were summed to give the  $(\sigma\Gamma)$  for each group. Using these bands an approximate system of three equations in three unknowns was obtained by neglecting the lower band at 0.76 MeV. The known spectral intensity at 3.2 MeV was also used to remove contributions to the activations due to that band. Expressed in matrix form this was (suppressing units for convenience)

$$(\overline{\sigma\Gamma}) \cdot \vec{\phi} = \vec{A} \quad , \quad (7a)$$

where

$$\overline{(\sigma\Gamma)} = \begin{pmatrix} 8.5 & 16 & 430 \\ 0 & 65 & 0 \\ 82.7 & 20.9 & 540 \end{pmatrix} \quad , \quad (7b)$$

$$\vec{\phi} = \begin{pmatrix} d\Phi(1.25)/dE \\ d\Phi(1.82)/dE \\ d\Phi(2.75)/dE \end{pmatrix} \quad , \text{ and} \quad (7c)$$

$$\vec{A} = \begin{pmatrix} 0.889 \\ 0.639 \\ 1.09 \end{pmatrix} \times 10^{10} \quad , \quad (7d)$$

and having the solution

$$\vec{\phi} = \begin{pmatrix} -0.484 \\ 9.83 \\ 1.71 \end{pmatrix} \times 10^7 \quad . \quad (8)$$

In this first approximation the unphysical result obtained at 1.25 MeV indicated that the spectral intensity was seriously overestimated between 1.82 and 2.75 MeV. Therefore an upper bound on the energy distribution was found by fitting the natural logarithm of intensity to a quadratic function of E expressed in MeV using the positive values of Eq. 8 and the known value at 3.2 MeV,

$$\phi_1(E) = (2.32 \times 10^{10}) \exp(-3.75E + 0.409E^2) \quad (9)$$

The form of Eq. 9 is shown in Fig. 8 as the curve labeled "Step 1."

Fractional activations were calculated with this function and the full set of gateways listed in Table I. These were found to be larger than the measured values by factors of 1.77, 1.47 and 2.23 for  $^{79}\text{Br}$ ,  $^{87}\text{Sr}$  and  $^{115}\text{In}$ , respectively. The next approximation was to lower the upper bound accordingly. To diminish the magnitude of the fit more at lower energies than near the fixed value at 3.2 MeV,  $\phi_1(1.82) = 9.77 \times 10^7$  was reduced by the average overestimation of the activations, 1.82. A new fit was obtained using spectral intensities of  $5.37 \times 10^7$ ,  $1.71 \times 10^7$  and  $8.96 \times 10^6$  at 1.82, 2.75 and 3.25 MeV. This gave

$$\phi_2(E) = (4.09 \times 10^8) \exp(-1.04E - 0.0424E^2) \quad (10)$$

Fractional activations computed using Eq. 10 differed from the measurements by 0.91, 1.11 and 1.36 for  $^{79}\text{Br}$ ,  $^{87}\text{Sr}$  and  $^{115}\text{In}$ , respectively, with an average factor of 1.13. Since this differed from unity by 13 %, comparable to the uncertainties for the integrated cross sections of Table I, the fitting procedure was terminated. The second order fit of Eq. 10 is shown in Fig. 8 along with a spectrum computed with EGS4 for the experimental geometry and materials and for an endpoint of 3.6 MeV. Despite the good agreement seen in the figure, the weakness of the approach was that it required an extrapolation outside the better determined region of 1.25 - 3.25 MeV in order to obtain spectral intensities at lower energies. Generally such an



extrapolation is suspect but in this case was justified by the assumption of slow variation for the natural logarithm of the energy distribution.

As confirmation of the spectrum of Fig. 8, a calculation was made of the corresponding dose. Normalized to a distance of  $z = 1$  m this was found to be  $269 \text{ rad min}^{-1}$ , agreeing within 4 % of the measured value of  $280 \text{ rad min}^{-1}$ .

### CONCLUSIONS

The XAN technique provides an ideal method for obtaining absolute measurements of the spectral and spatial distributions of bremsstrahlung while requiring relatively simple and inexpensive equipment and samples and avoiding problems inherent in other methods. The target package used is also small, portable and reusable. Although its utility was demonstrated by the characterization of x rays from a linear accelerator, XAN is equally well suited to the calibration of e-beam devices. However, the present accuracy of the technique is limited to about 10 % due to the available nuclear data and the nature of the approach employed to analyze the measured activations. Still it was not necessary to introduce any a priori assumptions regarding the spectral shape other than that the natural logarithm of the intensity was slowly varying above about 0.5 MeV. What remains for the future is the refinement of the analytical approach and its extension to higher energies as improvements are made to the nuclear database.

## REFERENCES

1. The Physics of Radiology, Fourth Edition, H. E. Johns and J. R. Cunningham (Thomas Publ. Co., Springfield, Ill., 1983).
2. A. Richter, Nucl. Phys. News 1, 20 (1990).
3. Industrial Electron Accelerators and Applications, E. A. Abramyan (Hemisphere Publ. Co., New York, 1988).
4. B. Bernstein and I. B. Smith, IEEE Trans. Nucl. Sci. NS-20, 294 (1973).
5. C. B. Collins, J. A. Anderson, Y. Paiss, C. D. Eberhard, R. J. Peterson and W. L. Hodge, Phys. Rev. C 38, 1852 (1988).
6. *The Aurora Bremsstrahlung Environment*, K. G. Kerris, Harry Diamond Laboratories Report No. HDL-TM-81-18 (unpublished).
7. R. Mohan, C. Chui and L. Lidofsky, Med. Phys. 12, 592 (1985).
8. *The EGS4 Code System*, W. R. Nelson, H. Hirayama and D. W. O. Rogers, Stanford Linear Accelerator Center Report No. SLAC 265, 1985 (unpublished).
9. *GEANT3*, R. Brun, F. Bruyart, M. Marie, A. C. McPherson and P. Zanarini, CERN Report DD/EE/84-1, 1987 (unpublished).
10. *ITS: The Integrated TIGER Series of Couples Electron/Photon Monte Carlo Transport Codes*, J. A. Halbleib and T. A. Mehlhorn, Sandia National Laboratories Report SAND84-0573, 1984 (unpublished).
11. D. A. Whittaker, K. G. Kerris, M. Litz, S. G. Gorbics and N. R. Pereira, J. Appl. Phys. 58, 1034 (1985).
12. R. Abrose, D. L. Kahler, H. E. Lehtihet and C. A. Quarles, Nucl. Instrum. Meth B56, 327 (1991).
13. F. R. Metzger, Prog. Nucl. Phys. 7, 54 (1959).

14. D. J. Landry and D. W. Anderson, Med. Phys. 18, 527 (1991)
15. G. T. Baldwin and J. R. Lee, IEEE Trans. Nucl. Sci. NS-33, 1298 (1986).
16. J. A. Anderson, C. D. Eberhard, K. N. Taylor, J. M. Carroll, J. J. Carroll, M. J. Byrd and C. B. Collins, IEEE Trans. Nucl. Sci. NS-36, 241 (1989).
17. W. C. Miller and B. Waldman, Phys. Rev. 75, 425 (1949).
18. Y. Paiss, C. D. Eberhard and C. B. Collins, J. de Phys. C9, 131 (1987).
19. J. A. Anderson and C. B. Collins, Rev. Sci. Instrum. 58, 2157 (1987).
20. J. A. Anderson and C. B. Collins, Rev. Sci. Instrum. 59, 414 (1988).
21. J. A. Anderson, J. M. Carroll, K. N. Taylor, J. J. Carroll, M. J. Byrd, T. W. Sinor, C. B. Collins, F. J. Agee, D. Davis, G. A. Huttlin, K. G. Kerris, M. S. Litz, D. A. Whittaker, N. R. Pereira and S. G. Gorbics, Nucl. Instrum. Meth. B40, 1189 (1989).
22. J. A. Anderson, C. D. Eberhard, K. N. Taylor, J. M. Carroll, M. J. Byrd and C. B. Collins, IEEE Trans. Nucl. Sci. NS-36, 241 (1989).
23. P. v. Neumann-Cosel, A. Richter, C. Spieler, W. Ziegler, J. J. Carroll, T. W. Sinor, D. G. Richmond, K. N. Taylor, C. B. Collins and K. Heyde, Phys. Lett. B266, 9 (1991).
24. J. J. Carroll, T. W. Sinor, K. N. Taylor, D. G. Richmond, M. Huber, N. Huxel, A. Richter, P. v. Neumann-Cosel, A. Richter and W. Ziegler, to be submitted to Phys. Rev. C.
25. C. B. Collins, J. J. Carroll, T. W. Sinor, M. J. Byrd, D. G. Richmond, K. N. Taylor, M. Huber, N. Huxel, P. v. Neumann-Cosel, A. Richter, C. Spieler and W. Ziegler, Phys. Rev. C 42, 1813 (1990).
26. Nuclei and Particles, Second Edition, E. Segre (Benjamin/Cummings Publ. Co., Menlo Park, Calif., 1982) p 369 ff.
27. G. Breit and E. Wigner, Phys. Rev. 49, 519 (1936).

28. Introduction to Radiological Physics and Radiation Dosimetry, F. H. Attix  
(Wiley, New York, 1986) Appendix E.
29. Table of Radioactive Isotopes, E. Browne and R. B. Firestone, ed. V. S. Shirley  
(Wiley, New York, 1986).
30. The Quantum Theory of Radiation, Third Edition, W. Heitler (Dover, New York, 1984)  
p 242 ff.
31. H. Kuhlenskampff, Ann. der Phys. 69, 548 (1922).

TABLE I

Relevant quantities for the isomeric nuclides employed in this work. Gateway energies,  $E_j$  and integrated cross sections,  $(\sigma\Gamma)_j$  were obtained from the literature as either direct evaluations or calculated from the parameters of Eq. 3 and 4. Uncertainties in the  $E_j$  were on the order of 3 % while those for the  $(\sigma\Gamma)_j$  were on the order of 10 %. The fluorescence energies,  $E_{\text{fluor}}$ , are the primary signatures of the decay of the isomers.

Isomer	$T_{1/2}$	$E_{\text{fluor.}} [\text{keV}]$	$E_j [\text{MeV}]$	$(\sigma\Gamma)_j [10^{-29} \text{ cm}^2 \text{ keV}]$
$^{79}\text{Br}^{\text{m}}$	4.9 s	207	0.761	5.9
			1.8	65
$^{87}\text{Sr}^{\text{m}}$	2.8 h	388	1.2	8.5
			1.9	16
			2.7	430
$^{115}\text{In}^{\text{m}}$	4.5 h	336	1.1	18.7
			1.4	64
			1.6	10.1
			2.0	10.8
			2.8	540
			3.3	760
$^{137}\text{Ba}^{\text{m}}$	2.6 min	662	3.2	220

TABLE II

Fractional activations normalized to exposure time obtained from samples containing the four calibrations isomers used in this work. These values were employed for the determination of the spectral intensity of the irradiating bremsstrahlung and have been normalized to  $z = 30$  cm.

Isomer	Normalized Fractional Activation [ $10^{-19} \text{ s}^{-1}$ ]
$^{79}\text{Br}^m$	$1.40 \pm 0.03$
$^{87}\text{Sr}^m$	$0.889 \pm 0.03$
$^{115}\text{In}^m$	$1.77 \pm 0.01$
$^{137}\text{Ba}^m$	$0.197 \pm 0.013$

## CAPTIONS

Figure 1: Schematic representation of the population of a nuclear isomer by a  $(\gamma, \gamma')$  reaction. The incident photon  $\gamma$  is absorbed with a cross section  $\sigma_0$  by the  $j^{\text{th}}$  gateway shown having a natural width  $\Gamma$ . The probabilities that the intermediate state decays directly back to the ground state and either directly or by cascade to the isomer are  $b_g$  and  $b_o$ , respectively. Photons promptly emitted during the population of the isomer are the  $\gamma'$ .

Figure 2: (a) Electron stopping measurements obtained using aluminum attenuators. The symbols plot the relative charge delivered to the aluminum collector during each linac pulse as a function of attenuator thickness in  $\text{g cm}^{-2}$ . The extrapolated range was found to be  $R_{\text{ext}} = 2.19 \text{ g cm}^{-2}$  and tables in the literature indicated<sup>28</sup> that this corresponded to an electron energy of 3.55 MeV. (b) Horizontal profile of the electron beam determined at a distance of 2.7 cm from the CuBe exit window. The symbols plot the charge collected by a large aluminum plate as it was moved across the beam. Values ranged from 0 when no part of the beam was intercepted to a maximum when all electrons were stopped. The best fit to the data was a Gaussian having a half radius  $r_{1/2} = 0.69 \text{ cm}$ . This defined the spot size of the electron beam at a distance corresponding to the entrance to the converter foil.

Figure 3: Typical pulse-height spectrum obtained from an  $^{115}\text{In}$  sample using a standard NaI(Tl) spectrometer. The sample had been irradiated for 15 min and was counted for 5 min. The peak at 336 keV was the fluorescence signature of the decay of  $^{115}\text{In}^{\text{m}}$  while that at 392 keV resulted from the decay of another indium isomer,  $^{113}\text{In}^{\text{m}}$ .

Figure 4: Axial dependence of the bremsstrahlung determined from measured fractional activations, A normalized to irradiation time for the calibration isotopes  $^{115}\text{In}$  and  $^{137}\text{Ba}$ . The

symbols are plotted as functions of  $R^2$  where  $R = z - z_0$  and  $z_0 = -(2.5 \pm 0.5)$  cm. This offset corresponded to the spacing between converter and exit window. The expected behavior was observed in the measurements and in the curves which resulted from EGS4 simulations.

Figure 5: Radial dependence of the bremsstrahlung determined from fractional activations, A normalized to irradiation time of indium annular samples exposed at various distances along the beam axis. Radial profiles are plotted at each distance and demonstrate the spread of the radiation lobe. The shape of the lobe was obtained by connecting values of a given relative intensity in the radial profiles and evidenced the expected qualitative behavior. The half angle for the bremsstrahlung was found to be  $\theta_{tot} = 23^\circ$ .

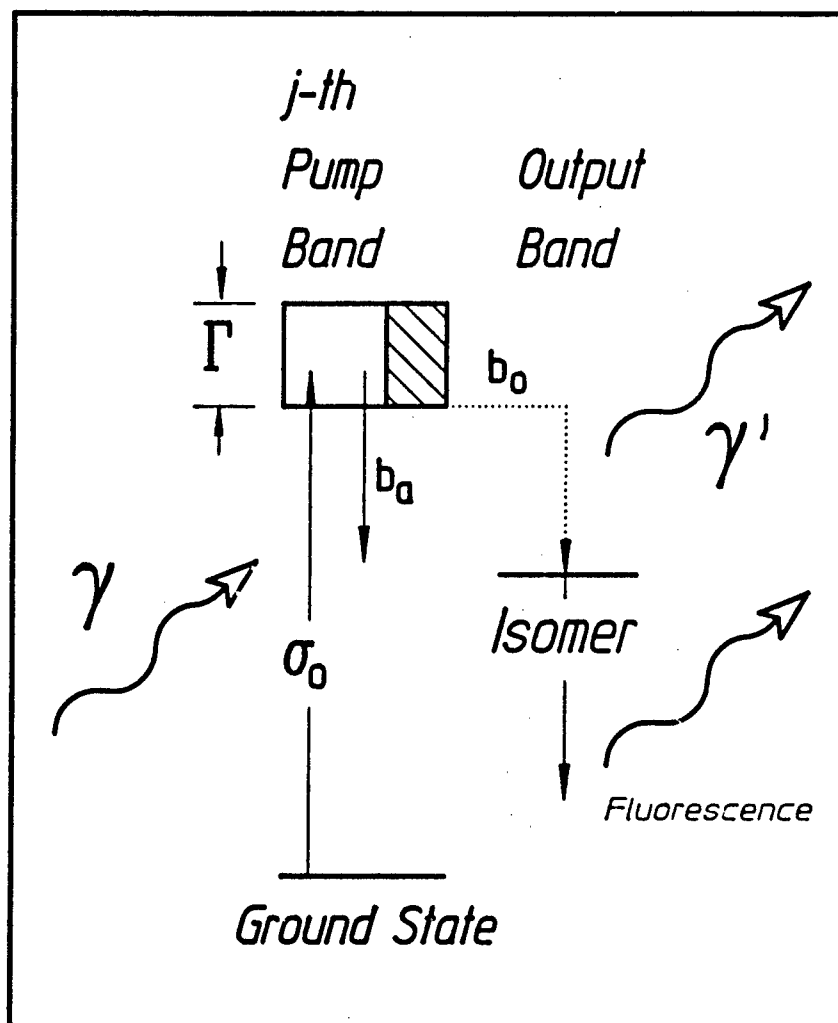
Figure 6: Photon intensities determined from dose measurements made with a calibrated ionization chamber showing (a) axial dependence and (b) angular dependence of the bremsstrahlung. In both cases the data evidenced the expected behavior observed in the results of isomeric activations. In (b) both dose and photoactivation measurements are included as well as a curve given by a Gaussian distribution with half angle of  $22^\circ$ .

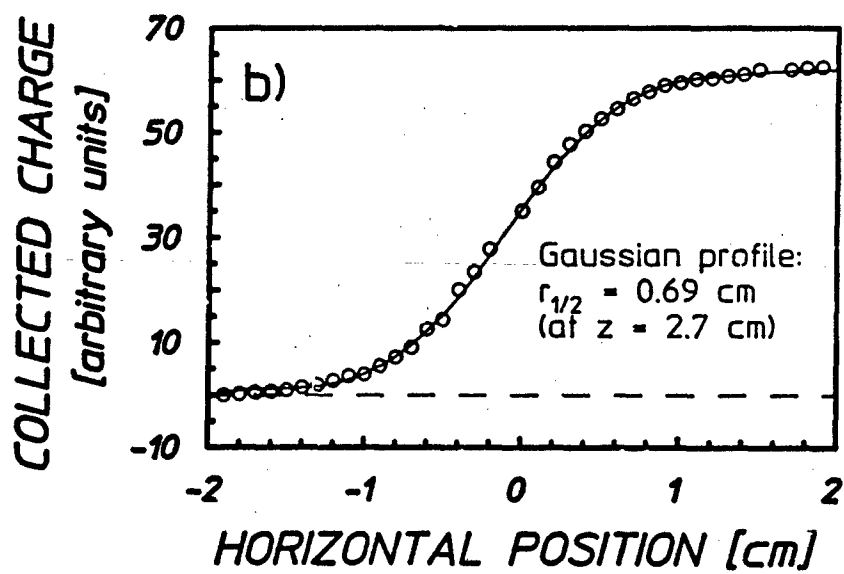
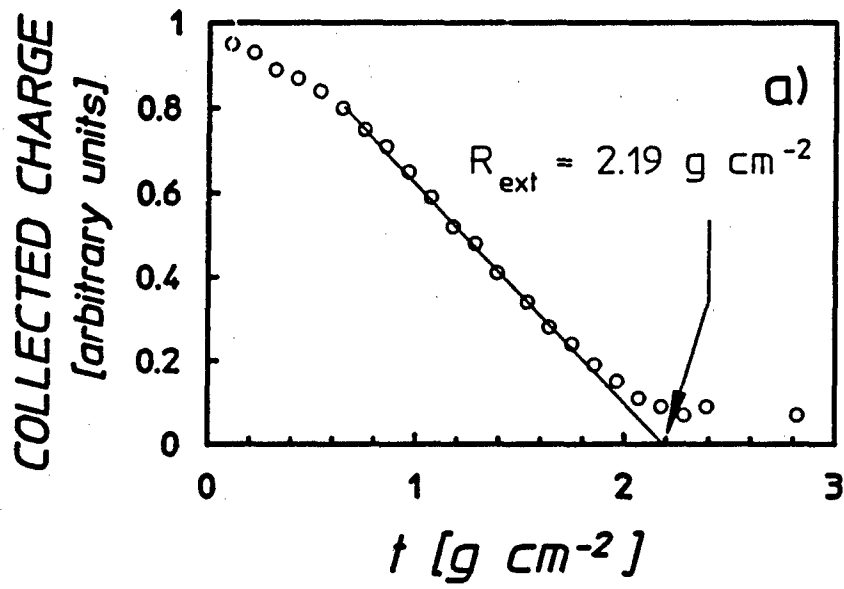
Figure 7: Integrated cross sections and excitation energies for the gateways of listed in Table I for the population of the four calibration isomers. The simplified mesh used to determine the spectral distribution of the bremsstrahlung was obtained by grouping the gateways into the bands shown. The energy representing each band was the average of the  $E_j$  for the enclosed states weighted by their integrated cross sections.

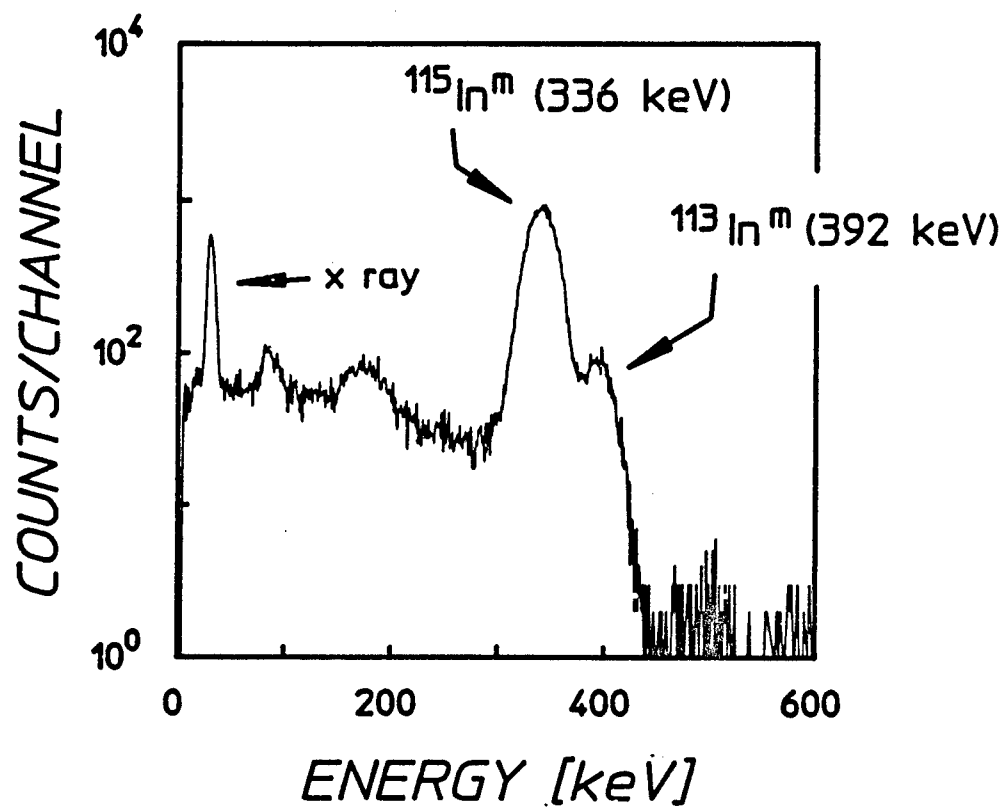
Figure 8: Spectral intensity of the bremsstrahlung determined from fractional activations of the calibration isomers. The dashed curve plots the result of the first iteration of the analytical

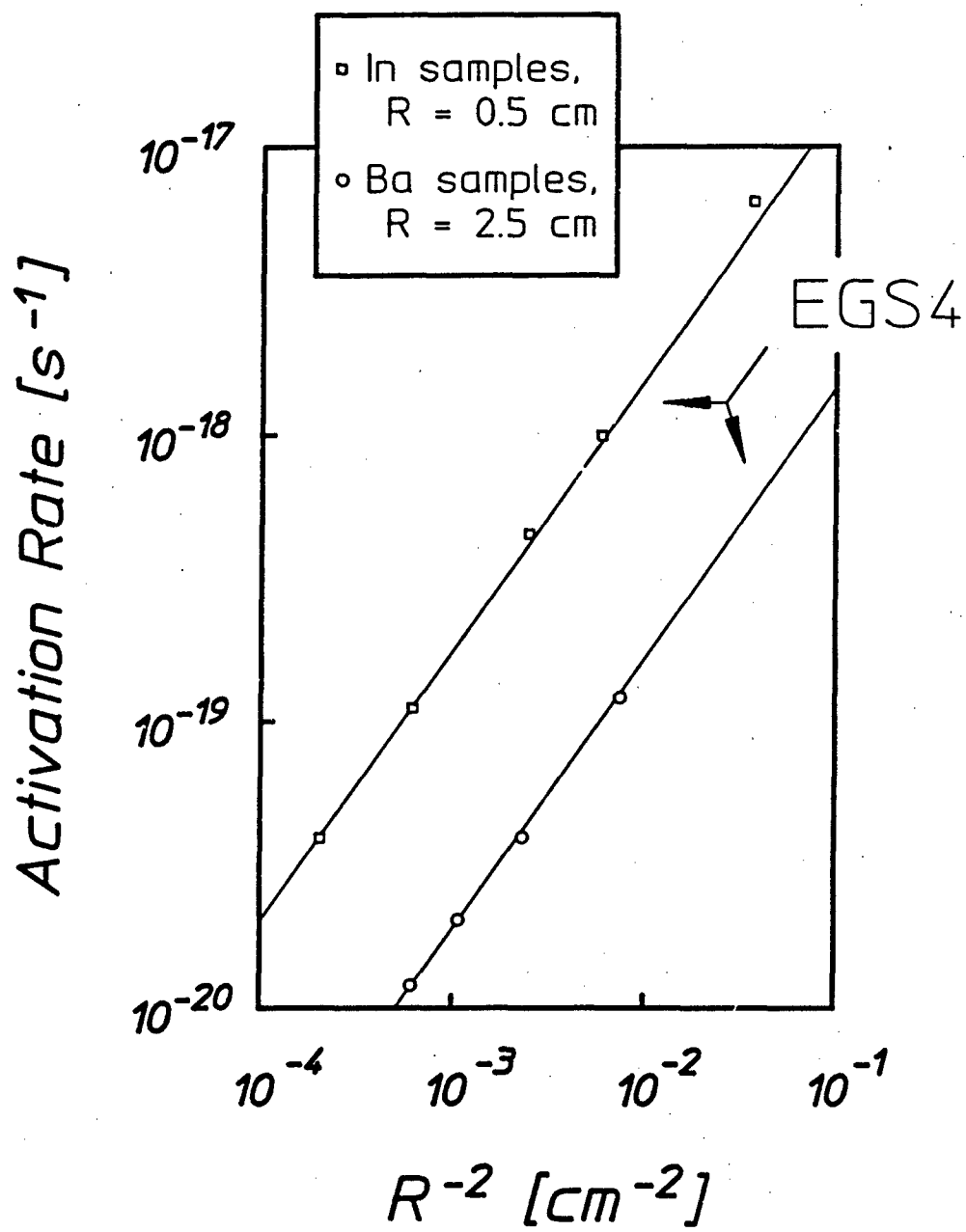


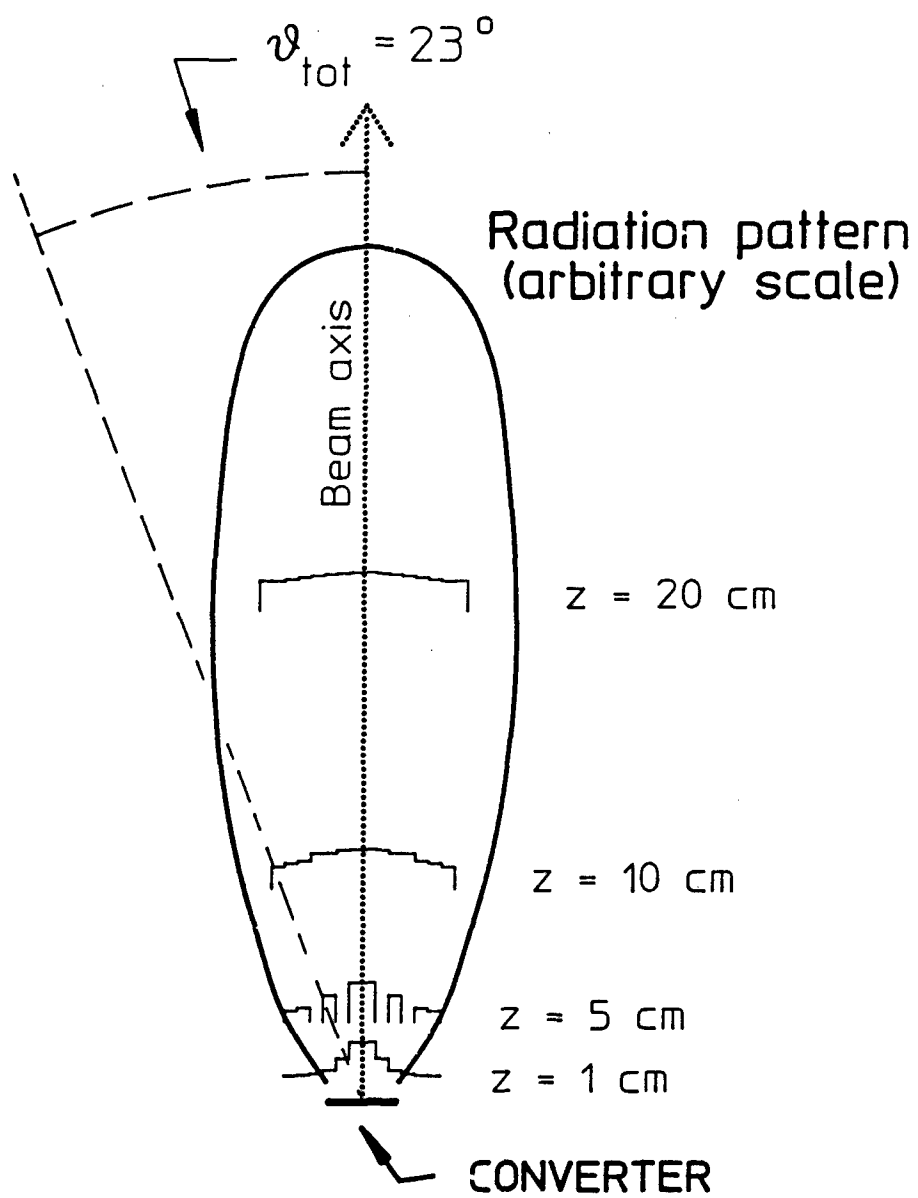
procedure and represented an overestimation of the flux which worsened at energies away from the fixed value at 3.25 MeV. The symbols plot the result of the final iteration at the five band energies of Fig. 7. Fractional activations computed using this fit were within an average of 13 % of the measured values. For comparison a spectrum calculated using EGS4 for the experimental geometry and materials and  $E_0 = 3.6$  MeV is shown. Good agreement was in evidence between the results of XAN, EGS4 and measurements of the dose delivered by the photon continuum of the figure.

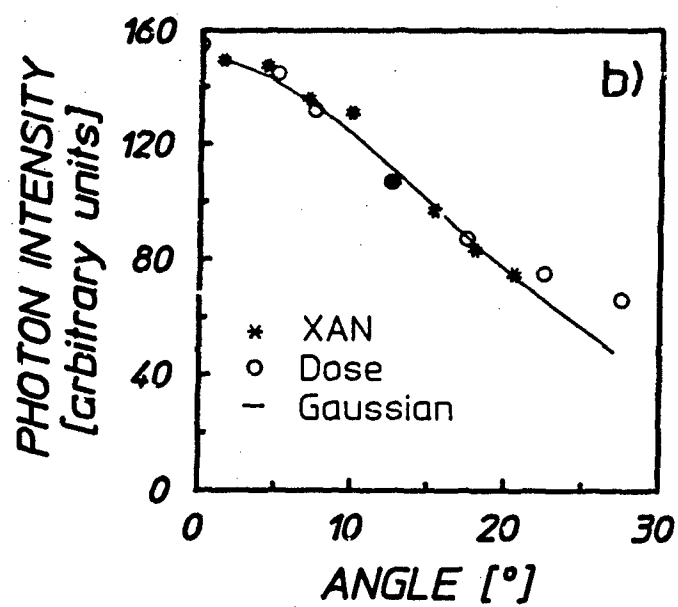
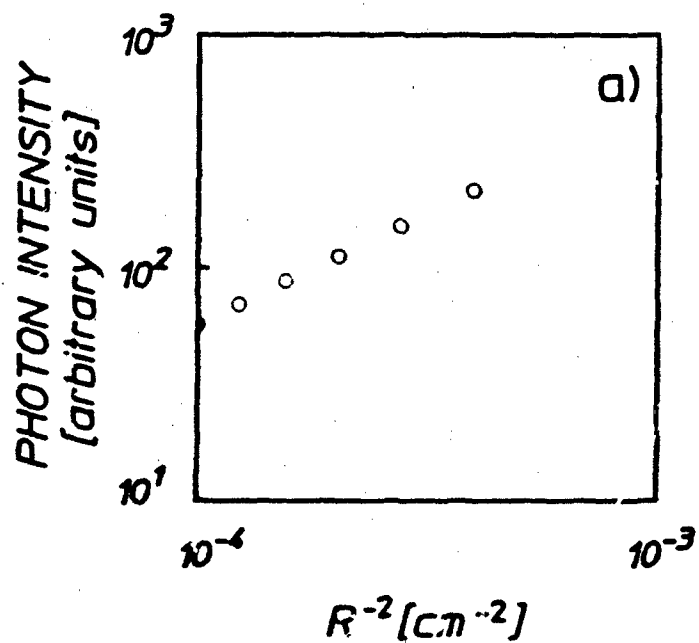


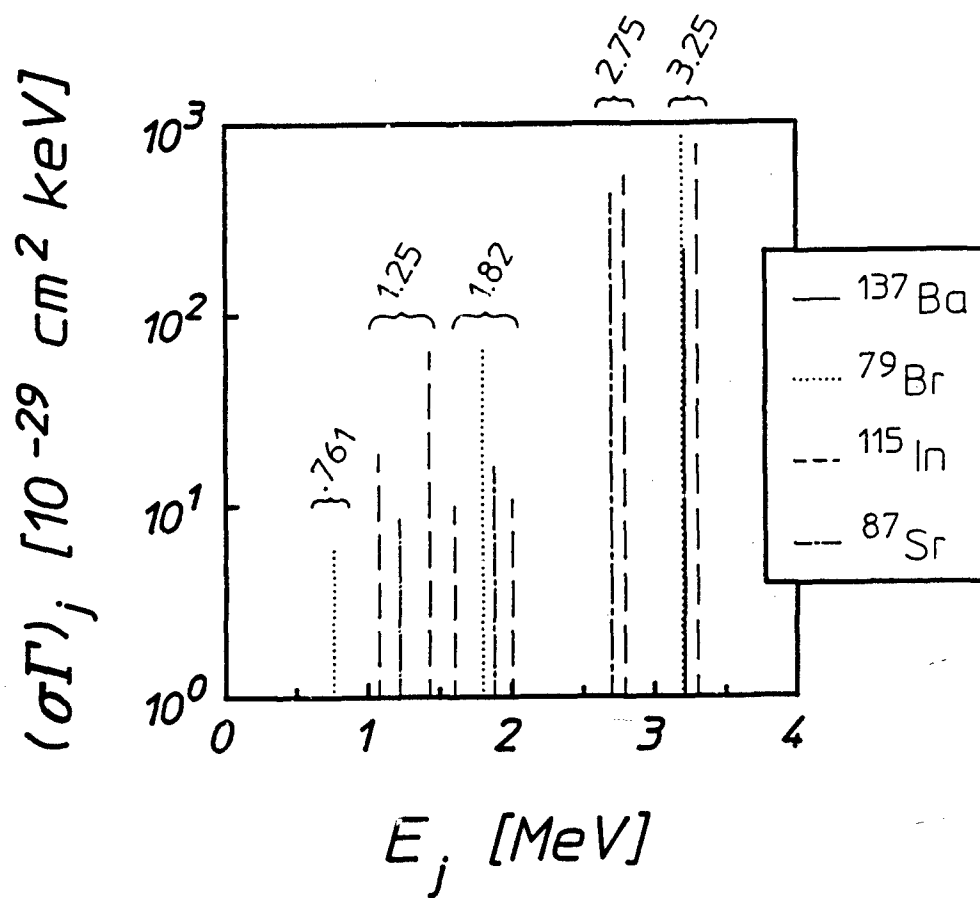




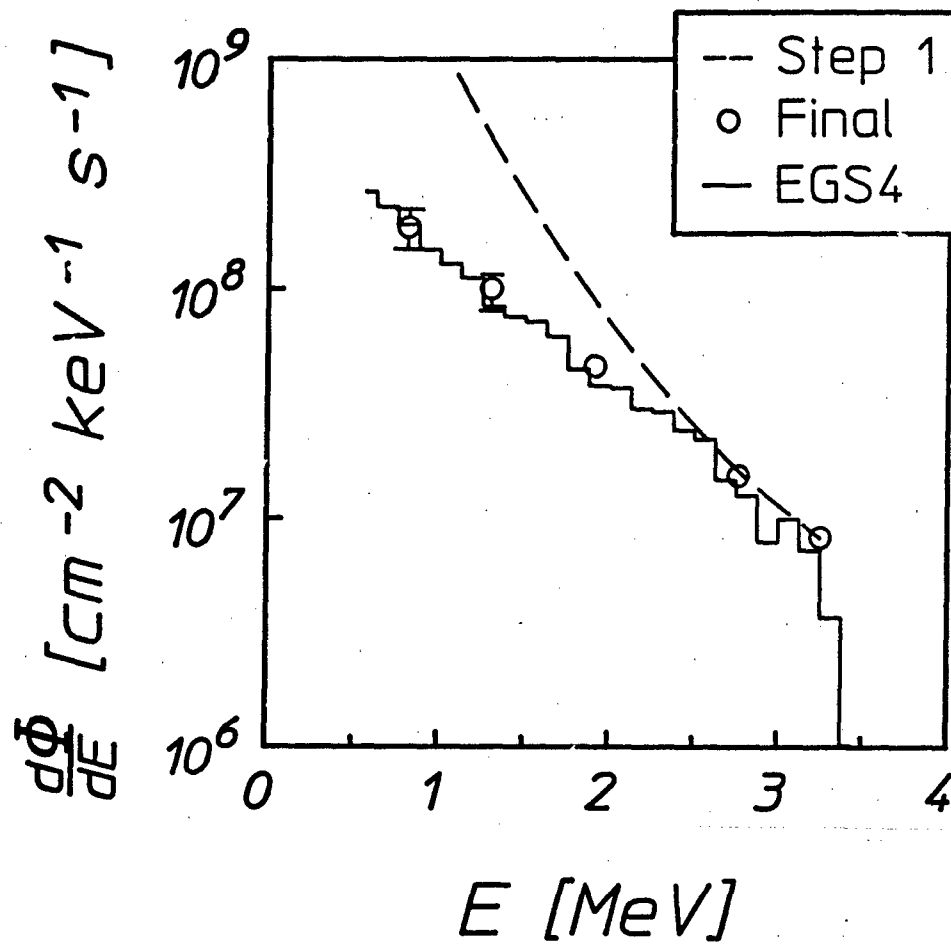












AN EVALUATION OF NANOPHASE DIAMOND FILM DOPED  
WITH  $^{57}\text{Fe}$  FOR USE AS A NUCLEAR TARGET

T. W. Sinor, J. D. Standifird, J. J. Carroll, K. N. Taylor,  
C. Hong, B. W. Johnson and C. B. Collins

INTRODUCTION

The Mössbauer effect proves ideal for the sensitive characterization of implanted materials because it reveals the sharpest resonances occurring in nature. In this work we used it to investigate the properties of  $^{57}\text{Fe}$  atoms implanted in nanophase (amorphous) diamond. The target had been prepared by depositing a 1  $\mu\text{m}$  thick film of nanophase diamond on a Ti substrate. The film was then ion implanted with  $^{57}\text{Fe}$  at an energy of 20 keV and a dose of  $5 \times 10^{16}$  atoms/cm<sup>2</sup>. The  $^{57}\text{Fe}$  atoms penetrated to a depth of approximately 200 Å in the film and represented a concentration of about 10%.

The relatively low number of  $^{57}\text{Fe}$  atoms implanted in the diamond film, combined with the presence of the Ti substrate, made the use of standard spectroscopic techniques impractical. To observe the resonant effects produced by the  $^{57}\text{Fe}$  nuclei required the use of backscattering techniques. In Mössbauer spectroscopy two options for this are available, conversion electron Mössbauer spectroscopy (CEMS) and  $\gamma$  ray and conversion x ray Mössbauer spectroscopy.

The purpose of this work was to determine the utility of nanophase diamond films doped with micrograms of  $^{57}\text{Fe}$  for use as nuclear targets in gamma-ray laser research. In these experiments the doped nanophase diamond would be used as the primary target excited by the bremsstrahlung radiation. Narrow-line fluorescence pumped through strong absorption resonances would be emitted with the best recoil-free fraction and the least amount of broad band background noise from scattering events in the target. Of secondary interest was the

potential for using doped diamond samples as efficient detectors for the resonance fluorescence emitted by the primary target. In this latter usage the electrons emitted from the detector as a result of the resonant absorption of the 14.4 keV component of the target fluorescence would be collected as signal.

## CEMS MEASUREMENTS

### Methods

Conversion electron Mössbauer spectroscopy has the advantage of being more sensitive to small concentrations of Mössbauer nuclei because of the large internal conversion coefficient of  $^{57}\text{Fe}$ . The primary drawback to the use of CEMS is that it has a maximum depth of sensitivity in the sample equal to that for the escape of conversion and Auger electrons. Since most Mössbauer samples are much thicker than this depth which is typically around 50 nm, CEMS is not sensitive to most of the volume of the material being studied. In iron, the conversion and Auger electrons have mean escape depths of 57 nm and 36 nm respectively.<sup>1</sup> One question to resolve in this work was whether CEMS might nevertheless serve as a useful means of detecting a component of resonant fluorescence in a larger broad band background of scattered radiation.

Figure 1 shows the experimental arrangement for the CEMS measurements reported here. The absorbers under investigation were mounted on a rotatable holder so that samples could be changed without breaking the vacuum in which the experiments were done. The signal electrons emitted from the sample being illuminated were detected by a chevron microchannel plate (MCP) assembly. A two stage electrostatic lens was used to accelerate and steer the signal electrons from the target to the detector.<sup>2</sup> The Mössbauer source and Doppler motor assembly were external to the UHV chamber and the Mössbauer source illuminated the absorber assembly through a thin Ti entrance window.

The electrostatic lens assembly served several purposes. It was responsible for both focusing and accelerating the low energy ( $\leq 15$  eV) conversion and Auger electrons emitted from the absorber to the detector while shielding the various elements from the ground potentials of the chamber walls. A 700 V gradient increased the electron energies to values more compatible with the sensitivity of the input to the MCP.

Lower energy resonant electrons arise from both a surface and a bulk effect. In iron, the electrons sensitive to surface effects have a mean escape depth of approximately 4 nm, while electrons from the bulk have a mean escape depth of approximately 40 nm. For electron energies less than 15 eV, the ratio of the surface component to the bulk effect is reported<sup>3</sup> to be 8.5 to 12.5.

In this work spectra were obtained by CEMS for a variety of samples. They included foils of natural iron that contain 2.19%  $^{57}\text{Fe}$ , 310 stainless steel enriched to 90.6%  $^{57}\text{Fe}$  for the iron content of the alloy, and a 93.55% enriched iron absorber. These foils were used to generate an absolute calibration curve for the detection system. As seen in Fig. 1 each sample under investigation was mounted on a rotatable target holder inside the UHV chamber. A 310 stainless steel calibration foil placed on the opposite side of the holder could be rotated into the illumination to verify the reproducibility of the detection system without altering the experimental arrangement.

### Analysis

The resulting calibration curve demonstrates the linear dependence of the resonant counting rate on the total illuminated mass of  $^{57}\text{Fe}$  in each absorber that would be expected in a well-aligned system. The reproducibility of the detection system gives a high degree of confidence with respect to the placement of the data points on the calibration curve that is shown in Fig. 2. For each point on the curve, the counting rates in the corresponding spectra were normalized to

a spectrum taken when the calibration absorber on the opposite side of the holder was rotated into the illumination. The highlighted point in the figure corresponds to the  $^{57}\text{Fe}$  implanted nanophase diamond sample. Direct comparison of this point with the calibration curve demonstrates that the emissivity of electrons from the nanophase diamond is greater than would be expected for a corresponding metallic absorber having the same number of Mössbauer nuclei. A typical spectrum taken with the nanophase diamond sample is shown in Fig. 3. The enhanced emissivity of resonant electrons from the nanophase diamond sample can be attributed to an increased Debye-Waller fraction as well as perhaps to the properties of the nanophase diamond film in which the  $^{57}\text{Fe}$  atoms were implanted.

The enhanced emission effects produced in nanophase diamond thin films were studied by overcoating the original sample with successive layers of nanophase diamond. Two layers having thicknesses of 230 Å and 240 Å, respectively, were deposited and calibration spectra were taken after each deposition. Analysis of the resonant counting rate from the sample versus the overcoat thickness revealed the presence of exponential and linear terms in the data. The exponential term represented attenuation of the resonant signal as the electrons propagated out of the film. The linear term corresponded to a small but definite increase in the signal that suggested the nanophase diamond material was able to enhance the emission of the electron signal. A numerical fit to the data yielded a mean free path of 30 nm.

## GAMMA-RAY AND CONVERSION X-RAY MEASUREMENTS

### Methods

The CEMS data indicated that the nanophase diamond film may have a relatively large recoil-free fraction at room temperature. However, since CEMS provides only information about the surface layer of the nanophase diamond it cannot be used to determine the recoil-free

fraction of the bulk material. Information about the bulk properties of the material can be obtained from  $\gamma$  and conversion x ray fluorescence techniques.<sup>4,5</sup> Specifically this technique was used to verify linearity and to obtain a relative measurement of the recoil-free fraction of the nanophase diamond film.

For  $\gamma$  and conversion x-ray fluorescence measurements data were collected in a typical geometry with a scattering angle of  $45^\circ$ . A specially designed graded shield was used to reduce environmental scattering of the source radiation into the detector. In addition to the graded shield an x-ray filter was placed between the source and scattering target to reduce the number of low energy x rays which resulted from de-excitation processes in the source. These x rays were a major source of noise in the signal and by attenuating them with an appropriate filter, the signal to noise ratios of the Mössbauer spectra were greatly improved. The scattered  $\gamma$  and x rays from the various targets were detected by a thin window NaI(Tl)-PMT combination.

#### Analysis

Data were collected for a variety of iron targets and the total counts in the resonance lines were plotted as a function of the total mass of  $^{57}\text{Fe}$  in the sample. The calibration curve is shown in Fig. 4. As expected the count rate increased linearly with the amount of  $^{57}\text{Fe}$  in the sample. The total signal count rate for the  $^{57}\text{Fe}$  implanted in the nanophase diamond film was plotted against the calibration curve and is shown in the inset of Fig. 4. As in the case of the CEMS measurement, direct comparison of this point with the calibration curve indicated that the fluorescent signal from the  $^{57}\text{Fe}$  in the nanophase diamond was greater than would be expected for a corresponding metallic absorber having the same number of Mössbauer nuclei. This unambiguously indicated that the recoil-free fraction of the nanophase diamond at room temperature is greater than that for iron. From this data it was possible to estimate a lower limit of the recoil-free fraction of the nanophase diamond.

## DETERMINATION OF THE RECOILLESS FRACTION OF NANOPHASE DIAMOND THIN FILMS

For the nuclear lifetimes usually encountered in the Mössbauer effect, the scattering process can be considered as a resonant absorption and subsequent re-emission. Under these conditions, the intensity of recoil-free resonant scattering will be proportional to the square of the Debye-Waller factor, while the intensity of recoil-free nonresonant scattering will be proportional to the first power of the Debye-Waller factor.<sup>4</sup> Multiple scattering, line width and interference effects are neglected in this analysis. Furthermore, the shapes of the lines after resonant scattering are assumed to be unaffected by self absorption. The recoilless fraction  $f$  of the nanophase diamond was determined from a measurement of the resonant scattering intensity calibrated against metallic iron foils with a known Debye-Waller fraction. A brief outline of the theory follows.

According to the Debye theory a solid may be considered to consist of a large number of linear oscillators with a distribution of frequencies ranging from zero to some maximum,  $\omega_D$ . The total number of oscillators is equal to  $3N$ , where  $N$  is the number of atoms in the solid. If the recoil energy of the nucleus is less than the quantum of energy necessary to excite the oscillator to the next higher energy level, the  $\gamma$  ray may be emitted without recoil. The probabilities of such recoilless emissions are, in most cases, governed by the Debye-Waller factor which is given by the Debye model as

$$f = \exp \left( - \frac{3E_R}{2k_B\theta_D} \left( 1 + 4(\pi/\theta_D)^2 \int_0^{\theta_D/T} \frac{x}{e^x - 1} dx \right) \right) . \quad (1)$$

In the limit of low or high temperatures Eq. 1 reduces to

$$f = \exp\left(-\frac{3E_R}{2k_B\theta_D}\right), \quad T \leq \theta_D$$

and

(2)

$$f = \exp\left(-\frac{6E_RT}{2k_B\theta_D^2}\right), \quad T > \theta_D$$

where  $T$  is the absolute temperature,  $k_B$  is the Boltzman constant and  $\theta_D$  is the Debye temperature. The Debye temperature is a measure of the stiffness of the lattice and is defined by the expression  $\hbar\omega_D = k_B\theta_D$ .

Absolute measurements of  $f$  are difficult to make. However relative measurements of the recoil-free-fraction can be made by comparing the resonant scatterings from a target with a known value of  $f$  with the emissions of the material with an unknown  $f$  using the same source. For purposes of calibration, we used metallic iron foils with a recoil-free fraction<sup>5</sup> at room temperature of  $f_{\text{iron}} = 0.69$ . This corresponds to a Debye temperature calculated from Eq. 1 of about 335 K. The Debye temperature reported in the literature<sup>6</sup> for iron is 460 K. This indicates that the recoil-free fraction reported by Debrunner and Morrison<sup>5</sup> could possibly be low. However, O'Connor and Longworth<sup>7</sup> have reported the recoilless fractions of  $^{57}\text{Co}$  in  $^{56}\text{Fe}$  and natural iron absorbers to be  $0.77 \pm 0.02$  and  $0.76 \pm 0.06$  respectively. These measurements correspond to a Debye temperature of 400 K. Preston et al.<sup>8</sup> give  $f = 0.90$  for iron at room temperature which corresponds to a Debye temperature of about 650 K.

This diverse range of  $f$ -values for metallic iron at room temperature indicates that the recoil-free fraction of thin films of the type usually used in Mössbauer spectroscopy are sensitive to the history of the foil, i.e., rollins procedure, annealing, etc. To obtain an absolute value for



the recoil-free fraction of the iron doped nanophase diamond it would have been necessary to determine  $f_{\text{iron}}$  for the calibration foils used in these experiments. However, as an approximation the value of  $f = 0.69$  from Debrunner and Morrison<sup>5</sup> was used to obtain a lower limit for  $f_{\text{dia}}$  and the corresponding Debye temperature was calculated for Eq. 1.

If the recoil-free fraction for the source is  $f_s$  and the absorber is  $f_{\text{abs}}$ , the probability for resonant absorption is  $f_s f_{\text{abs}}$  and the probability for resonant reemission is  $f_s f_{\text{abs}}^2$ . To relate this to an experimentally measured parameter we note that in a scattering geometry the total area under the lines of a Mössbauer spectrum is given by

$$A_{\text{Theory}} = \frac{\pi}{2} \sum_i \Gamma_i n_i \sigma_0 f_s f_{\text{abs}}^2 \quad (3)$$

where  $n_i$  is the number of Mössbauer nuclei per  $\text{cm}^2$ ,  $\Gamma_i$  is the full-width half maximum of the  $i^{\text{th}}$  resonance line and  $\sigma_0$  is the cross-section for resonance interaction.

The corresponding area of an experimental spectrum that has a Lorentzian shape is given by

$$A_{\text{exp}} = \frac{\pi}{2} \sum_i \epsilon_i \Gamma_i^{\text{exp}} \quad (4)$$

where

$$\epsilon_i = \frac{N_0 - N_{\text{b}}}{N_{\text{b}}} \quad (5)$$

Here  $N_0$  is the total intensity of the resonantly scattered gamma rays and  $N_{\text{b}}$  is the nonresonant background.

If the resonant scatterings of two targets are compared and if the recoil-free fraction of one of the materials is known we may take the ratio of the experimentally determined areas in the Mössbauer resonance and equate these to Eq. 4 to obtain

$$\frac{A_{1\text{exp}}}{A_{2\text{exp}}} = \frac{f_1^2}{f_2^2}, \quad (6)$$

or more specifically,

$$f_{\text{dia}} = f_{\text{iron}} \sqrt{A_{\text{dia}}/A_{\text{iron}}}. \quad (7)$$

Equation 7 provides an approximate value of the recoil-free fraction of the nanophase diamond film which is proportional to the area under the lines of the experimentally measured spectrum.

The determination of  $f$  from a measurement of the area of an experimental Mössbauer spectrum has been widely used. This method was developed by Shirley et al.<sup>9</sup> and later generalized by Lang.<sup>10</sup> In the present context it is important to notice that Eq. 7 is independent of the recoil-free fraction of the source. Furthermore by taking the ratio of the areas instrumental errors should cancel.

From the calibration data of Fig. 4 and using  $f_{\text{iron}} = 0.69$  we obtained  $f_{\text{dia}} = 0.94$  with a lower bound of 0.85. Using this measurement of  $f$  it is possible to determine the Debye temperature  $\Theta_D$  by using Eq. 1 to make a plot of recoil-free fraction vs Debye temperature. This plot is shown in Fig. 5. As seen from the figure, the median value of the recoilless fraction of the nanophase diamond corresponds to a Debye temperature of 900 K.

### CONCLUSION

In these experiments the Mössbauer properties of <sup>57</sup>Fe implanted nanophase diamond samples were investigated. The CEMS data indicates that the nanophase diamond film has a relatively large recoil-free-fraction at room temperature and that enhanced emission effects may

be produced in the amorphous diamond. Analysis of the resonant counting rate from the sample versus the overcoat thickness revealed the presence of both exponential and linear terms in the data. The exponential term is indicative of the attenuation of the electrons as they escape from the film. The linear term is believed to represent a small but definite growth of the resonant electron signal. Further analysis of the  $^{57}\text{Fe}$  implanted nanophase diamond sample is necessary to fully understand the mechanisms responsible for its enhanced electron emissivity. Particular emphasis will be placed on re-implantation of the nanophase diamond sample so that more overcoating experiments can be performed to aid in the continuing study of resonant electron propagation and emission in nanophase diamond films.

Gamma and conversion x-ray Mössbauer spectroscopy has been used to experimentally determine the Debye-Waller fraction for the nanophase diamond film. The recoilless fraction  $f$  of the nanophase diamond film was determined from a measurement of the resonant scattering intensity calibrated against metallic iron foils with a known recoil-free fraction. Preliminary results give a median value of  $f_{\text{dia}} = 0.94$  for the nanophase diamond film and a corresponding Debye temperature of 900 K for comparison with the value of 335 K indicated by recoil-free fractions of 0.69 in conventional iron Mössbauer foils. The large recoil-free fraction at room temperature makes nanophase diamond a promising substrate for micrograms of exotic nuclear materials that are of particular interest in gamma ray laser research.

## REFERENCES

1. J. A. Sawicki, in Industrial Applications of the Mössbauer Effect, ed. G. J. Long and J. G. Stevens. (Plenum Press, New York, 1986), p. 83.
2. T. W. Sinor, J. D. Standifird, K. N. Taylor, C. Hong, J. J. Carrell and C. B. Collins, (submitted to Rev. Sci. Instrum.).
3. G. Klingelhöfer and E. Kankleit, Hyperfine Interaction, 57, 1905 (1990).
4. J. K. Major, Nucl. Phys. 33, 323 (1962).
5. P. Debrunner and R. J. Morrison, Rev. Mod. Phys. 36, 463 (1962).
6. G. Burns, Solid State Physics, (Academic Press, Orlando, Florida, 1985) p. 354.
7. D. A. O'Connor and G. Longworth, Nucl. Instr. and Methods, 30, 290 (1964).
8. R. S. Preston, S. S. Hanna and J. Heberle, Phys. Rev. 128, 2207 (1962).
9. D. A. Shirley, M. Kaplan and P. Axel, Phys. Rev. 123, 816 (1961).
10. G. Lang, Nucl. Instr. and Methods, 24, 425 (1963).

## CAPTIONS

Figure 1: Schematic diagram showing the arrangement of the sample holder and MCP detection assembly inside the UHV chamber. Note that the sample holder can be rotated to obtain calibration spectra without altering the experimental arrangement.

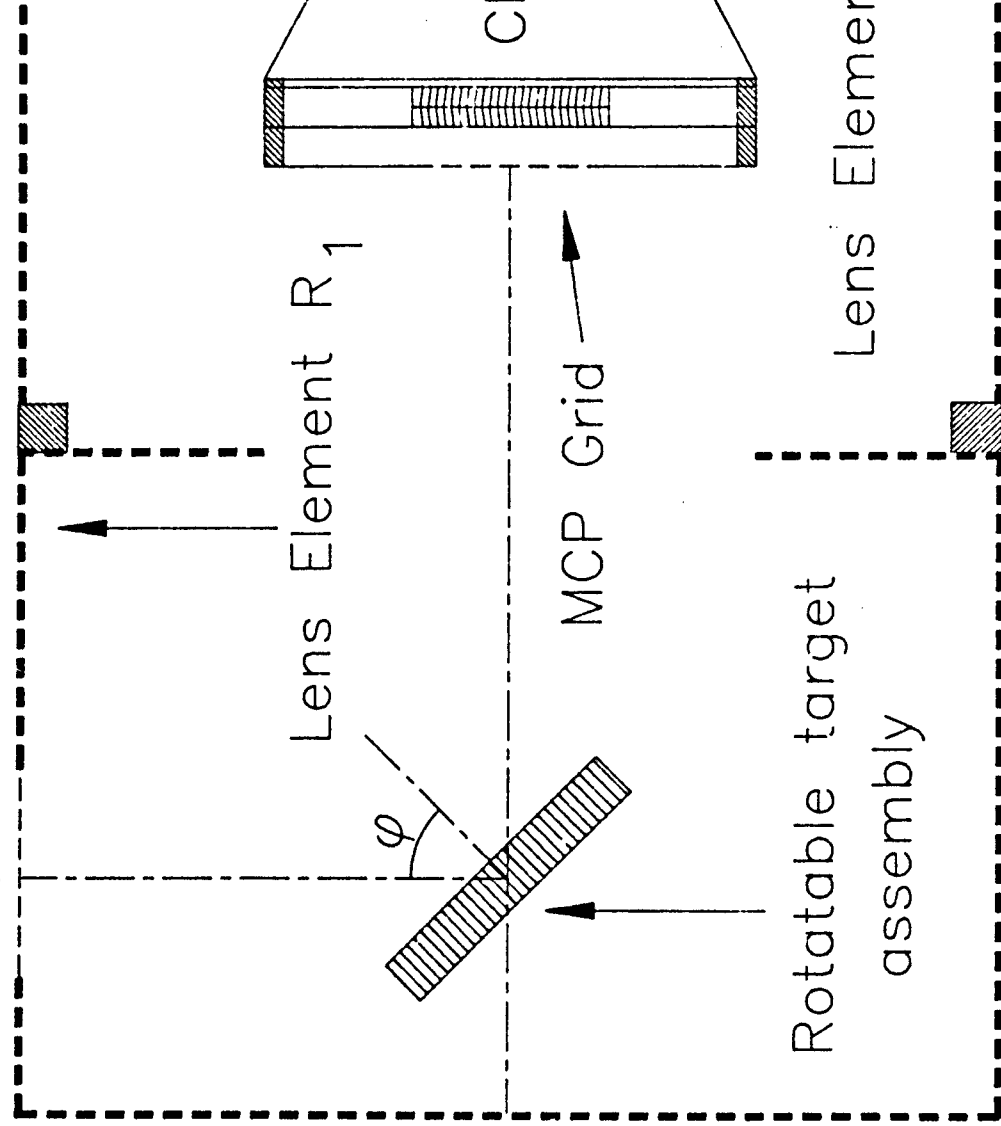
Figure 2: Calibration curve for the resonant counting rate of the metallic samples as a function of the number of micrograms of  $^{57}\text{Fe}$  contained within them. The highlighted point at 8.5 micrograms corresponds to the implanted amorphous diamond sample. The increase in emissivity over the metallic absorbers can be seen clearly.

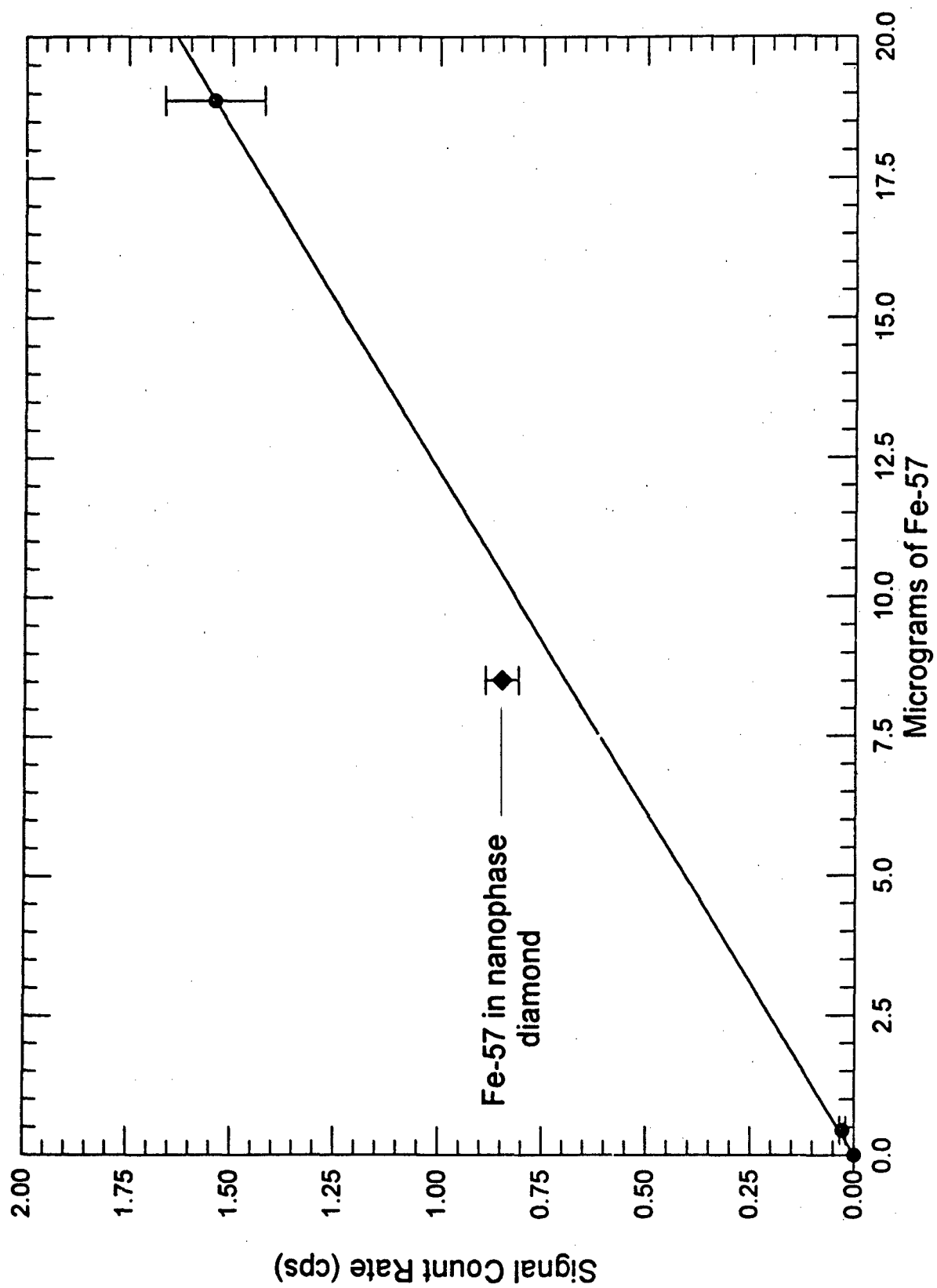
Figure 3: CEMS spectrum of the  $^{57}\text{Fe}$  implanted nanophase diamond sample. The partially resolved doublet is due to quadruple splitting in the sample.

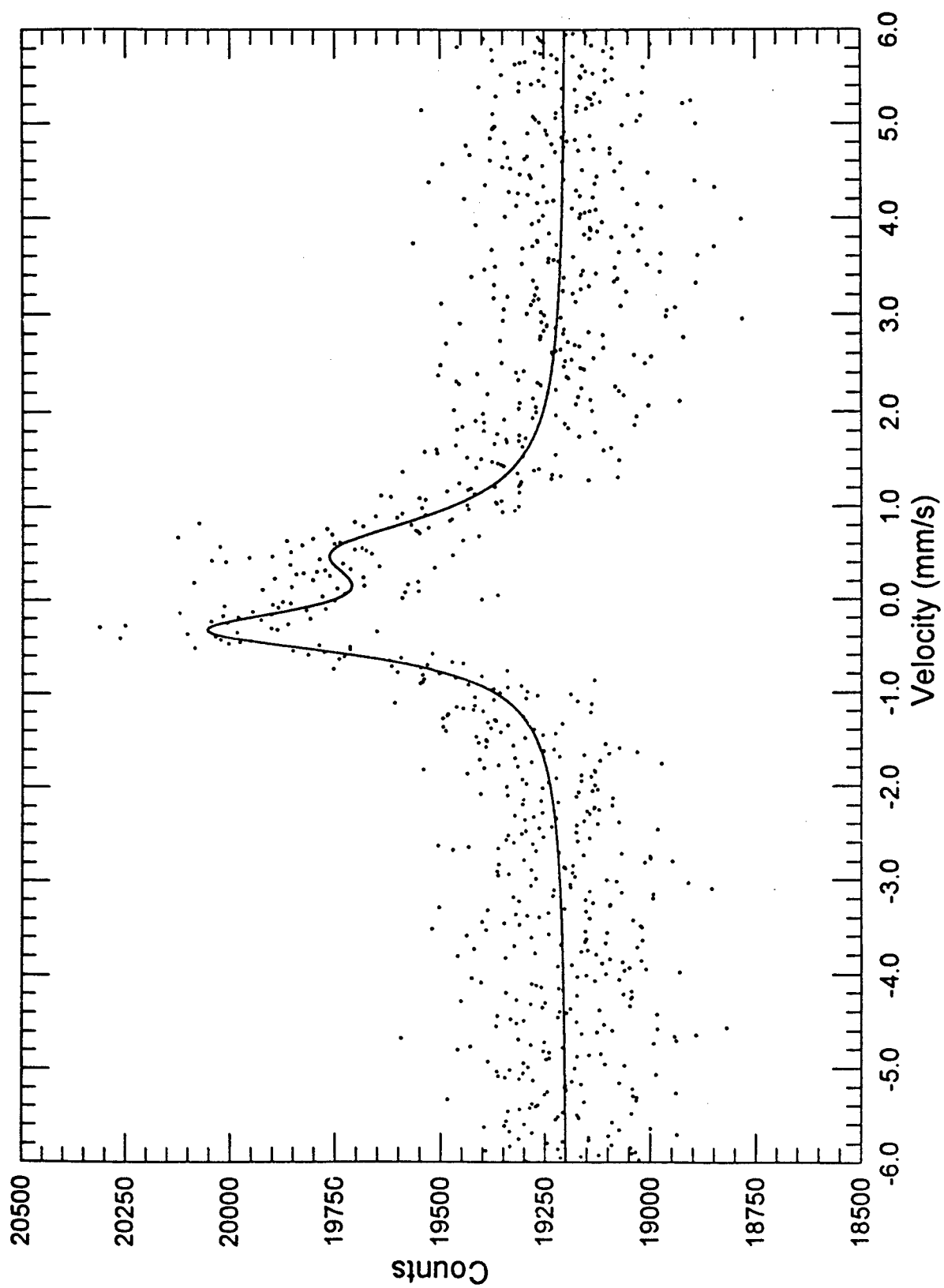
Figure 4: Calibration data for signal count rate vs. amount of  $^{57}\text{Fe}$ . The inset shows the datum for iron in amorphous diamond. From this data the lower limit on the recoil-free-fraction of amorphous diamond is  $f = 0.85$ .

Figure 5: Plot of recoil-free-fraction vs Debye temperature. Using the measured value of  $f = 0.94$  the corresponding Debye temperature of nanophase diamond was 900 K.

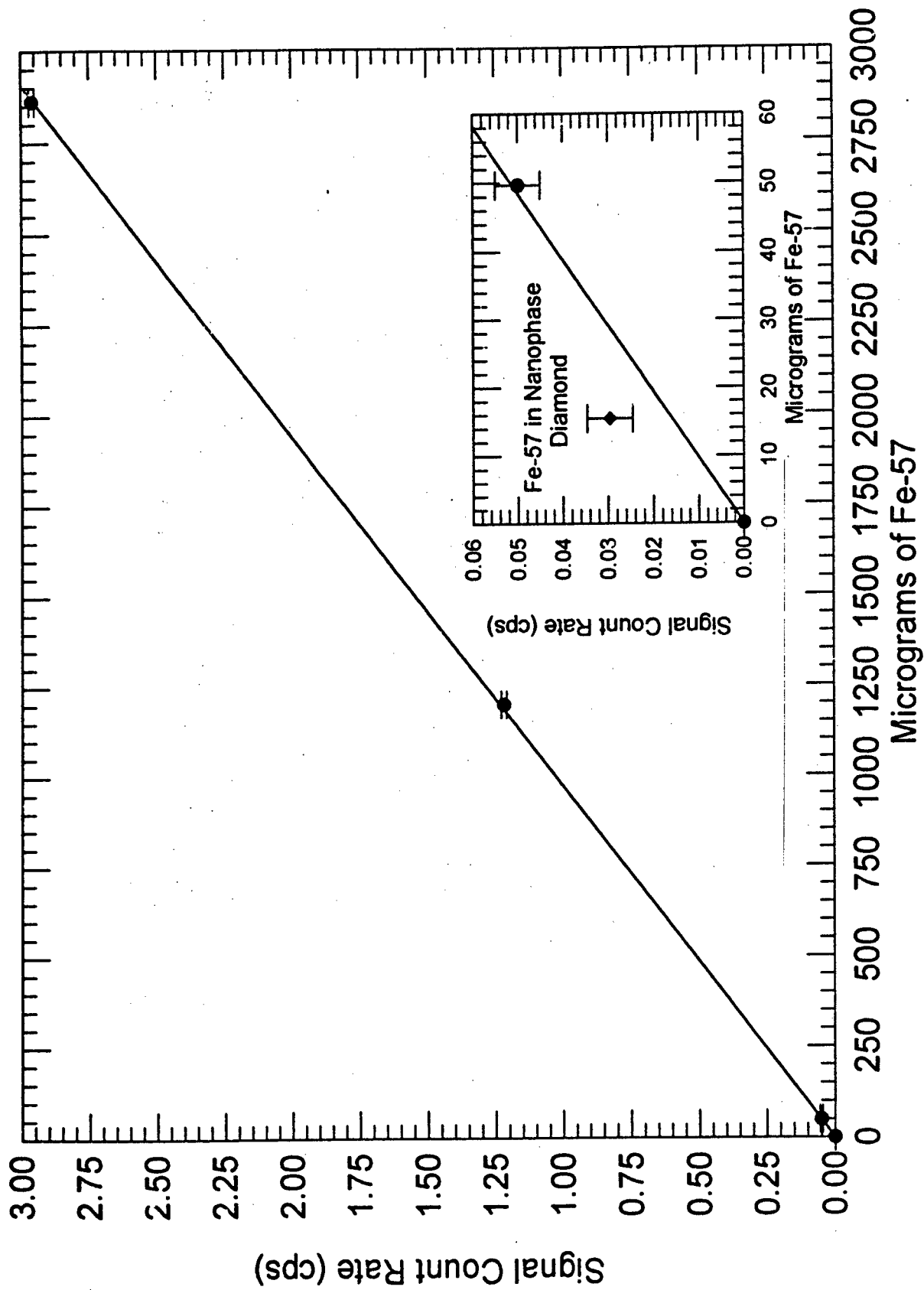
Incident Radiation

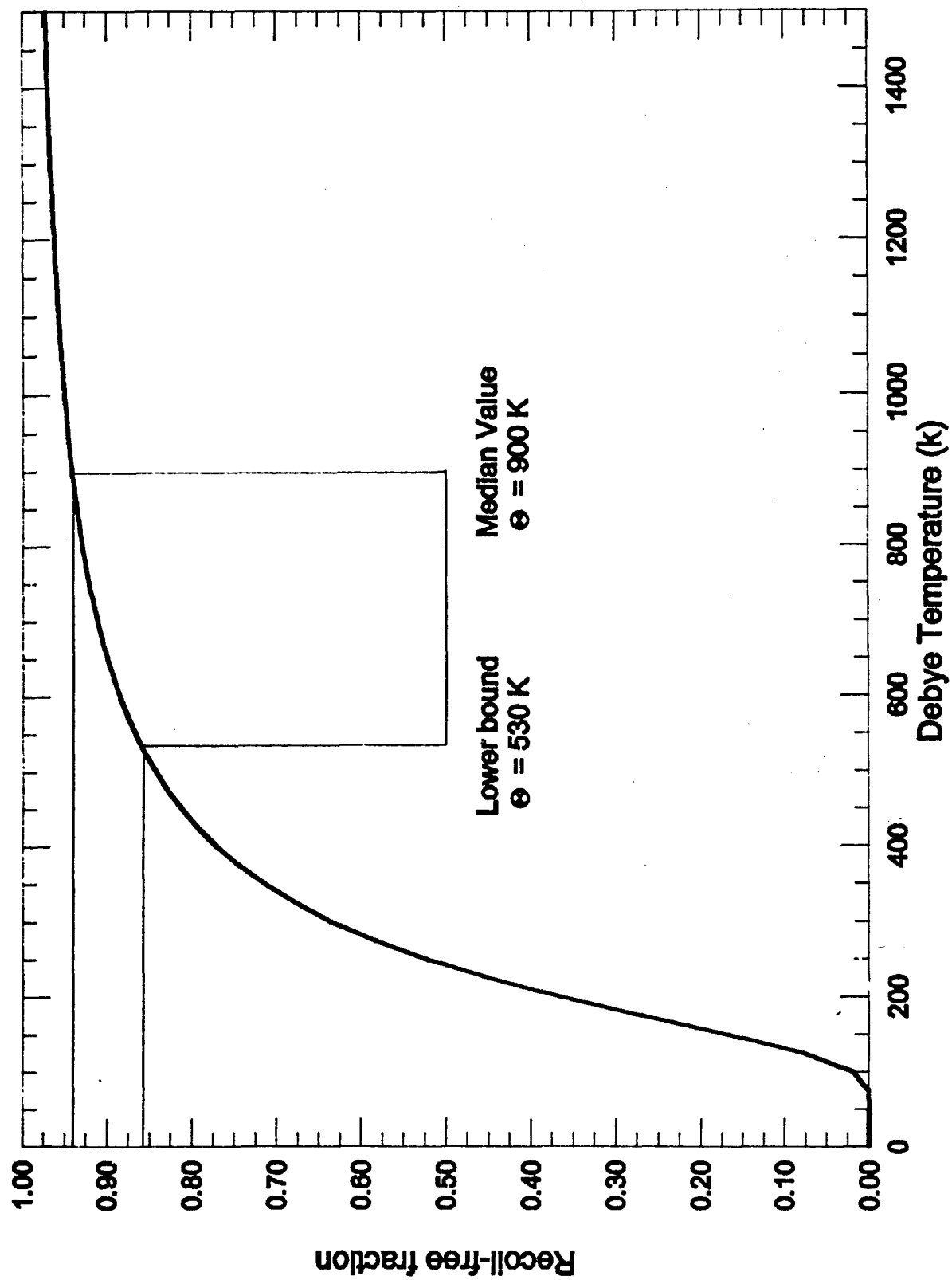












## Common thresholds and the role of deformations in the photoexcitation of isomers

C. B. Collins, J. J. Carroll, K. N. Taylor, D. G. Richmond, and T. W. Sinor

Center for Quantum Electronics, University of Texas at Dallas, P.O. Box 830688, Richardson, Texas 75083

M. Huber, P. von Neumann-Cosel, A. Richter, and W. Ziegler

Institut für Kernphysik, Technische Hochschule Darmstadt, D-6100 Darmstadt, Germany

(Received 25 October 1991)

Photoexcitations of the short-lived isomers  $^{167}\text{Er}^m$ ,  $T_{1/2}=2.28$  s,  $^{178}\text{Hf}^m$ ,  $T_{1/2}=18.68$  s,  $^{191}\text{Ir}^m$ ,  $T_{1/2}=4.94$  s, and  $^{197}\text{Au}^m$ ,  $T_{1/2}=7.8$  s, were produced with bremsstrahlung from the superconducting Darmstadt linear accelerator. Excitation functions were measured for the population of these isomers by  $(\gamma, \gamma')$  reactions between 2 and 7 MeV. They indicated that the isomers were excited by resonant absorption through isolated intermediate states having integrated cross sections in excess of  $10^{-26}$  cm<sup>2</sup> keV, i.e., values about 1000 times larger than most  $(\gamma, \gamma')$  activation reactions reported previously although they were comparable to those reported earlier for the depopulating reaction  $^{180}\text{Ta}^m(\gamma, \gamma')^{180}\text{Ta}$ . In all four nuclei a common onset was observed near 2.5 MeV for intermediate states with strengths much larger than those occurring at lower energies. The summed cross sections exhibit a clear correlation with the ground state deformations.

PACS number(s): 25.20.Dc, 27.70.+q, 27.80.+w

## I. INTRODUCTION

The photoexcitation of nuclear isomers by  $(\gamma, \gamma')$  reactions has been known for more than 50 years [1,2]. For most of this time, studies of this phenomenon have been concentrated either upon higher photon energies around particle thresholds or upon relatively low energies of excitation,  $E \leq 2$  MeV. Results in the former case have been dominated by the photoabsorption through the giant dipole resonance and have emphasized concerns for the gross properties of the photoexcitation process [3] or for tests of statistical models of  $\gamma$  decay at high excitation energies [4]. At the lower energies, efforts have been characterized by the excitation of discrete intermediate states that have branched or cascaded back to an isomer with a significant probability [5]. Under those conditions the integrated cross sections for the photoexcitation of isomers have been typically  $10^{-29}$  to  $10^{-27}$  cm<sup>2</sup> keV.

Only recently have studies been extended systematically into the intermediate range of energies and then with surprising results. Initiated with the observation [6] of the deexcitation of the isomer  $^{180}\text{Ta}^m(\gamma, \gamma')^{180}\text{Ta}$  with an unprecedented integrated cross section exceeding  $10^{-25}$  cm<sup>2</sup> keV, such extraordinary values were subsequently reported [7] for  $^{176}\text{Lu}(\gamma, \gamma')^{176}\text{Lu}^m$ , also. A large survey of 19 nuclides was reported [8] that covered the broad range of end-point energies 0.5–11 MeV from four different accelerators and established that comparable integrated cross sections can be found in the majority of cases studied. However, the relatively coarse mesh over which those measurements were conducted prevented the extraction of the excitation energies and strengths of individual intermediate states (IS's).

As a next step, a series of experiments was performed in the 2–7-MeV range in order to identify and characterize the important intermediate levels. These studies were

motivated by two principal aspects. First, the very efficient coupling of the ground state (g.s.) and isomer demonstrated in Refs. [6–8] provided unexpected encouragement of schemes [9] to use the resonant photoexcitation of isomer (or the reverse process, the sudden depopulation of an isomer) as a mechanism to pump a  $\gamma$ -ray laser. Among other conditions, the feasibility depends sensitively on the locations and coupling strengths of the resonant states. Second, the reaction mechanism selects a unique set of states with two features: a large partial g.s. width and strong admixtures in the wave function, which induce the decay into states efficiently cascading to the isomer. A schematic representation of this process which defines important parameters is shown in Fig. 1. In the excitation energy region investigated, the underlying nuclear structure is almost unexplored and theoretical interpretations are badly needed. To our knowledge, the only attempt to interpret similar data on

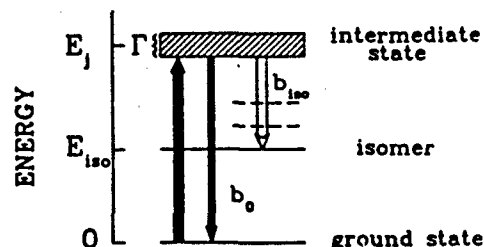


FIG. 1. Schematic representation of the resonant photoexcitation mechanism for population of an isomer with energy  $E_{\text{iso}}$ . The hatched area describes an intermediate-state IS with energy  $E_j$  and total decay width  $\Gamma$ . The direct branch to the ground state is denoted by  $b_0$ , and  $b_{\text{iso}}$  represents the sum of all branchings leading to the isomer. The dashed horizontal lines indicate that the decay to the isomer usually proceeds via a cascade.

a microscopic base is found in Ref. [10]. On the other hand, such data provide stringent constraints for any model calculation.

A study of the deexcitation of  $^{180}\text{Ta}^m$  confirmed the striking results of Ref. [6]. It was found to occur through two intermediate states at 2.8 and 3.6 MeV with integrated cross sections of  $1.2 \times 10^{-25}$  and  $3.5 \times 10^{-25}$  cm<sup>2</sup> keV, respectively [11]. The excitation of isomers with large probabilities through discrete intermediate states was also established in the reactions [12,13] of  $^{123,125}\text{Te}(\gamma, \gamma')^{123,125}\text{Te}^m$  and  $^{115}\text{In}(\gamma, \gamma')^{115}\text{In}^m$ . However, in these latter cases, integrated cross sections were of the order of  $10^{-26}$  to  $10^{-25}$  cm<sup>2</sup> keV.

Utilizing the large natural abundance of  $^{115}\text{In}$ , complementary nuclear resonance fluorescence experiments were performed and the important intermediate states were identified [13]. Unified model [14] calculations provided a qualitative explanation of the IS as being due to fragmented  $g_{9/2} \rightarrow g_{7/2}$  spin-flip strength.

The next step in understanding would require an extension of the information available on IS's in a variety of nuclei which might build a base for more systematic nuclear structure interpretations. The recent survey [8] indicates two empirical trends, viz., an average increase of yields with mass number and a correlation with the g.s. deformation. These findings are illustrated in Figs. 2(a)

and 2(b) in which the integrated cross sections obtained at an electron energy of 6 MeV are plotted versus  $A$  and  $N_p N_n$ , respectively. The latter is the product of open-shell proton and neutron occupation numbers and is a well-established measure of the deformation driving proton-neutron interactions [15]. Its application is restricted to nuclei with  $A > 90$ . While the above-mentioned trends are clearly visible, before attempting a detailed comparison one should keep in mind that these integrated cross sections have been normalized by arbitrarily assuming a single IS at 2 MeV.

One purpose of the present experiments was to investigate the empirical correlation with the g.s. deformation more closely. Therefore the nuclides  $^{167}\text{Er}$ ,  $^{179}\text{Hf}$ ,  $^{191}\text{Ir}$ , and  $^{197}\text{Au}$  were chosen because they cover a large span of deformations ( $\delta = 0.09$ – $0.32$ ), but lie within the same group in Fig. 2(a) and have comparable mass numbers. Furthermore, the well-deformed  $^{167}\text{Er}$  and  $^{179}\text{Hf}$  are prime candidates to verify that the extraordinarily large cross sections of the IS derived [11] for  $^{180}\text{Ta}^m$  are indeed not uncommon. Additional results obtained in the  $A = 70$ – $90$  mass region will be presented elsewhere.

## II. EXPERIMENTS

### A. Methods

Elemental samples of Ir, Au, and In (as a calibration standard) and the compounds  $\text{HfO}_2$  and  $\text{Er}_2\text{O}_3$  of typically 5–15 g served as targets. The materials were contained in hollow aluminum cylinders with 3.5 cm length and 1.4 cm outer diameter.

Isomeric populations were produced by exposing the targets to bremsstrahlung from a 3-mm tantalum converter foil irradiated by the electron beam from the injector of the new superconducting S-DALINAC accelerator at the Technische Hochschule Darmstadt [16]. Electron energies were varied from 2 to 7 MeV with a minimum step size of 125 keV. The electron energies were measured with an accuracy of 50 keV before and after each exposure. At each end point, individual samples were irradiated axially in close proximity to the converter. Each target cylinder was held in position by an aluminum stop which terminated a plastic transfer tube. The proper alignment of the beam was achieved by maximizing the dose delivered to a remote ionization chamber shielded to observe only the central 12 mrad of the bremsstrahlung cone.

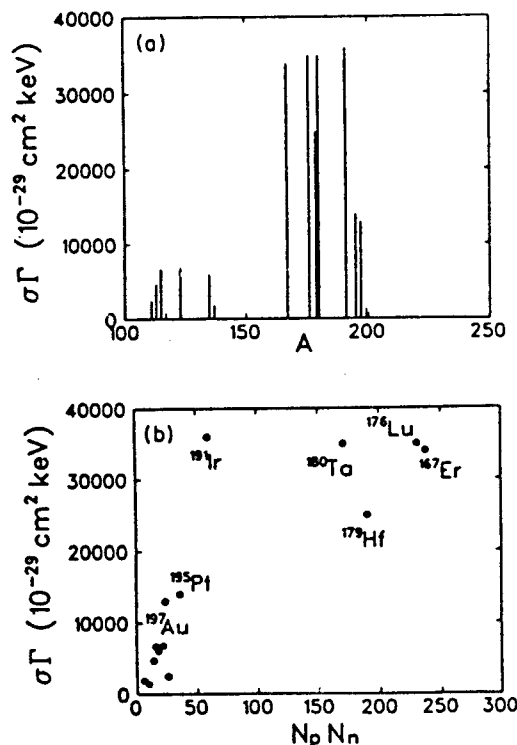


FIG. 2. Integrated cross sections of Ref. [8] for an electron energy of 6 MeV determined according to the assumption of a single hypothetical intermediate state at 2 MeV plotted versus (a) mass number  $A$  and (b) the product of open-shell proton and neutron occupation numbers  $N_p N_n$  calculated according to Ref. [15].

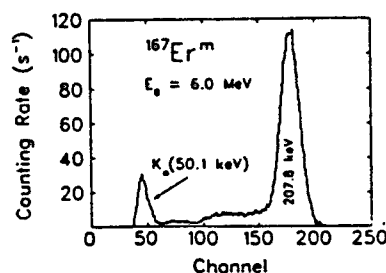


FIG. 3. Pulse-height spectrum of the  $\gamma$  decay of the isomer  $^{167}\text{Er}^m$  pumped by bremsstrahlung from a 6-MeV electron beam.

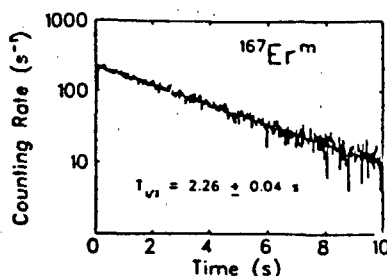


FIG. 4. Time-decay spectrum of the isomer  $^{167}\text{Er}^m$ . The straight line represents a best fit with  $T_{1/2} = 2.26 \pm 0.04$  s.

Variations in all beam parameters were recorded during the experiments. In particular, the charge passed to the converter was determined for each exposure by integrating the current with an analog circuit whose time constant for charging was arranged to match the lifetime of the isomer being investigated. Nominal beam currents were  $5 \mu\text{A}$ . The lengths of the exposures were typically chosen to be twice the half-life of the isomer in question, while the calibration sample  $T_{1/2} = 4.486$  h was exposed for 5 min.

The termination of each irradiation provided a trigger signal which initiated the pneumatic transport of each sample through the plastic tube to a well-type NaI(Tl) detector for counting. This detector and all necessary electronics for the experiments were located in a room separate from the accelerator hall. A phototransistor signaled the arrival of the sample within the detector and started the simultaneous acquisition of both pulse-height and multichannel-scalar spectra. Examples of spectra obtained in this way are shown in Figs. 3 and 4. A quad counter/timer was gated by TTL signals at the start and end of irradiation, and at the arrival of the sample in the detector to measure the precise durations of exposure and transport.

The numbers of isomers produced by these irradiations were determined from the counting rates measured in distinctive fluorescence lines. The particular  $\gamma$ -ray signatures used in these measurements and other relevant parameters are given in Table I. The raw number of counts in each peak was corrected for the finite durations of exposure, transport, and counting, the absolute counting efficiencies of the detector, and the relative emission intensities. The opacity of the samples to the escape of the

signature  $\gamma$  rays was compensated by a factor calculated with a Monte Carlo code specifically adapted for the well-type detector geometry.

### B. Data analyses

The experimentally measured yield of isomers,  $N_f$ , resulting from the irradiation of  $N_T$  ground-state nuclei with bremsstrahlung is given analytically by

$$N_f = N_T \int_{E_c}^{E_0} \sigma(E) \frac{d\Phi(E)}{dE} dE, \quad (1)$$

where  $E_0$  is the end-point energy,  $d\Phi(E)/dE$  is the time-integrated spectral intensity in  $\text{cm}^{-2} \text{keV}^{-1}$  of the photon field, and  $\sigma(E)$  is the cross section in  $\text{cm}^2$  for the reaction. The spectral intensity is conveniently expressed as the product of a flux  $\Phi_0$  of all photons above a cutoff energy  $E_c$  of 0.5 MeV incident on the target and a relative intensity function  $F(E, E_0)$ , which is normalized according to

$$\int_{E_c}^{E_0} F(E, E_0) dE = 1. \quad (2)$$

Equation (2) allows the definition of a normalized yield or activation per photon,  $A_f(E_0)$ , given by

$$A_f(E_0) = \frac{N_f}{N_T \Phi_0} = \int_{E_c}^{E_0} \sigma(E) F(E, E_0) dE. \quad (3)$$

At energies of interest in these experiments, IS's have widths that are small in comparison to their spacings and if can be assumed that  $d\Phi/dE$  is constant over each resonance region. Then Eq. (3) reduces to the summation

$$A_f(E_0) = \sum_j (\sigma \Gamma)_j F(E_j, E_0). \quad (4)$$

with  $(\sigma \Gamma)_j$  giving the integrated cross section of the  $j$ th IS having excitation energy  $E_j$ . We note that non-resonant cross sections which would inhibit the use of Eq. (4) are not considered. The previous claims for the significance of nonresonant contributions [17] have recently been disproven [18] and shown to have resulted merely from the omission of the importance of intense contributions to the photon fields arising in such experiments from environmental Compton scattering.

The normalized activation  $A_f$  can be useful as a sensitive indication of the opening of  $(\gamma, \gamma')$  channels whenever photons of the requisite energies  $E_j$  become available. A change of the end-point energy  $E_0$  of the bremsstrahlung

TABLE I. Summary of the literature values [20] for the relevant nuclear parameters and transparencies for the escape of fluorescence photons from samples of the nuclides. In the column for  $K$ , entries of NA indicate nuclei for which  $K$  cannot be defined or for which there are no accepted values.

Nuclide	g.s. spin		$E_{\text{iso}}$ (keV)	isomer spin		$T_{1/2}$ (s)	Abundance (%)	Principal fluorescence	Transparency (%)
	$J^\pi$	$K$		$J^\pi$	$K$			(keV)	
$^{167}\text{Er}$	$\frac{7}{2}^+$	$\frac{7}{2}$	208	$\frac{1}{2}^-$	$\frac{1}{2}$	2.28	22.95	207.79	48
$^{170}\text{Hf}$	$\frac{7}{2}^+$	$\frac{7}{2}$	375	$\frac{1}{2}^-$	$\frac{1}{2}$	18.68	13.63	214.31	43
$^{191}\text{Ir}$	$\frac{7}{2}^+$	$\frac{7}{2}$	171	$\frac{11}{2}^-$	$\frac{11}{2}$	4.94	37.30	129.43	13
$^{197}\text{Au}$	$\frac{7}{2}^+$	NA	409	$\frac{11}{2}^-$	NA	7.80	100.00	279.11	11

lung spectrum modulates the spectral intensity function  $F(E_j, E_0)$  in Eq. (3) at all of the important IS energies. The largest effect in the excitation function occurs when  $E_0$  is increased from a value just below some state at  $E_j$  to one exceeding it so that  $F(E_j, E_0)$  varies from zero to some finite value. In earlier work [5] plots of quantities equivalent to Eq. (3) as functions of the end-point energies of the irradiating spectra showed very pronounced activation edges, which appeared as sharp increases at the energies  $E_j$  corresponding to excitations of new intermediate states.

Calculated spectra of both  $\Phi_0$  and  $F(E, E_0)$  were obtained from the EGS4 electron-photon transport code. This Monte Carlo program is well established in the medical physics community, and its general validity has been demonstrated elsewhere [19]. In this work confidence in the calculated photon spectra was maintained by calibrating them with the reaction  $^{115}\text{In}(\gamma, \gamma')^{115}\text{In}^m$ . This reaction is now sufficiently well characterized in the literature [13] to support its use in this way and, in this effort, was preferred over the calibration reaction  $^{87}\text{Sr}(\gamma, \gamma')^{87}\text{Sr}^m$  used in other work [11,12] because of the completeness of the experimental information for it in the low-energy region not covered in the present experiments.

### III. RESULTS

Figure 3 shows a typical pulse-height spectrum of the fluorescence from an isomeric population pumped by bremsstrahlung through some intermediate state(s). In this particular case, the data from  $^{167}\text{Er}^m$  are shown for an electron energy of  $E_0 = 6$  MeV. Even with the limited resolution of the NaI(Tl) well detector, the distinctive signature line of  $^{167}\text{Er}^m$  is clear in the data obtained from one 10-s exposure of an erbium sample. Nevertheless, to confirm the identity of the peak, a measurement of the time decay of the fluorescent state population was taken in parallel. Such a decay curve is shown for  $^{167}\text{Er}^m$  in Fig. 4 together with a fit which agrees well with the literature value [20] of the half-life,  $T_{1/2} = 2.28$  s.

To improve statistics, at least nine successive repetitions of the cycle for irradiation and counting were made for each nuclide at each end-point energy of the bremsstrahlung. Each was corrected for slight variations of the photon flux on that particular exposure, as well as for any variations in the transit time from the site of exposure to the counting enclosure. The resulting curves of  $A_f$  obtained from Eq. (3) as functions of the bremsstrahlung end point  $E_0$  are shown in Figs. 5-8. The results at 6 MeV given by Carroll *et al.* [8] are included for comparison. The agreement of these values obtained in completely different experimental environments is excellent.

Values for the integrated cross sections  $(\sigma\Gamma)_{fj}$  were found by fitting Eq. (4) to the data of Figs. 5-8. A useful measure of the degree of fit was provided by the residue of activation,  $R_M(E_0)$ , remaining after subtracting contributions from the  $M$  lowest-lying intermediate states,

$$R_M(E_0) = A_f(E_0) - \sum_{E_j=E_1}^{E_M} (\sigma\Gamma)_{fj} F(E_j, E_0), \quad (5)$$

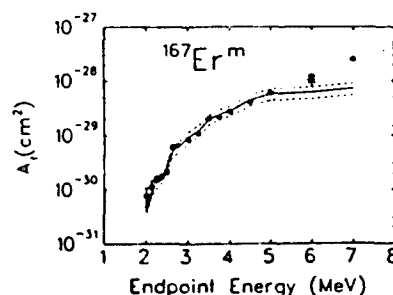


FIG. 5. Normalized yield  $A_f$  of the activation of  $^{167}\text{Er}^m$  as a function of electron energy. The asterisk represents the experimental result of Ref. [8] obtained at 6 MeV. The solid line corresponds to the fit to the data, and its error bounds are given by the dotted lines.

where  $E_M$  is the resonance energy of the highest-lying intermediate state already included. Fitted values of the integrated cross sections  $(\sigma\Gamma)_{fj}$  were found by minimizing  $R_M(E_0)$  for the lowest-energy state giving a break in the excitation function, and then iterating after including any new gateways suggested by the data. The contribution of IS's below  $E_0 = 2$  MeV that could not be distinguished by the present experiments was estimated by assuming a single state for which properties were adjusted to give the best description of  $A_f$  values for energies below 2.5 MeV. Because of the sudden jump of intermediate-state strength of typically more than a factor of 10 around 2.5 MeV, variations of the IS cross sections at lower energies have little effect on the results.

The results of fitting the model of Eq. (4) to the data are shown in Figs. 5-8 and are summarized in Table II. Uncertainties are shown explicitly. It should be noted

TABLE II. Values of integrated cross sections  $(\sigma\Gamma)_{fj}$  and excitation energies  $E_j$  of the intermediate states most important in the production of these isomers by  $(\gamma, \gamma')$  reactions. Values needed to fit the data were determined in this work by minimizing the residues of Eq. (5).

Isomer	$E_j$ (MeV)	$(\sigma\Gamma)_{fj}$ ( $10^{-29}$ cm <sup>2</sup> keV)
$^{167}\text{Er}^m$	$1.9 \pm 0.1$	$1500 \pm 200$
	$2.5 \pm 0.1$	$8000 \pm 2000$
	$3.1 \pm 0.15$	$28\,000 \pm 4000$
	$3.8 \pm 0.2$	$50\,000 \pm 15\,000$
$^{170}\text{Hf}^m$	$1.5 \pm 0.2$	$40 \pm 10$
	$2.5 \pm 0.1$	$1200 \pm 200$
	$3.0 \pm 0.15$	$6000 \pm 1000$
	$4.3 \pm 0.2$	$75\,000 \pm 15\,000$
$^{191}\text{Ir}^m$	$1.2 \pm 0.3$	$180 \pm 50$
	$2.5 \pm 0.1$	$2500 \pm 300$
	$3.2 \pm 0.15$	$5000 \pm 500$
	$4.3 \pm 0.2$	$30\,000 \pm 4000$
$^{197}\text{Au}^m$	$1.7 \pm 0.3$	$70 \pm 30$
	$2.5 \pm 0.1$	$500 \pm 50$
	$3.2 \pm 0.15$	$4500 \pm 500$
	$4.2 \pm 0.2$	$20\,000 \pm 4000$

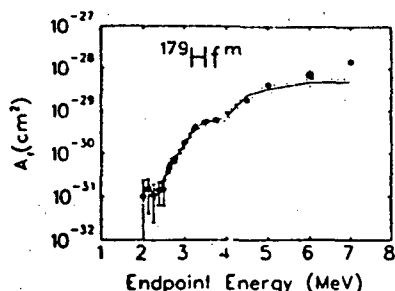


FIG. 6. Normalized yield  $A_f$  of the activation of  $^{179}\text{Hf}^m$  as a function of electron energy. The asterisk represents the experimental result of Ref. [8] obtained at 6 MeV. The solid line corresponds to the fit to the data, and its error bounds are given by the dotted lines.

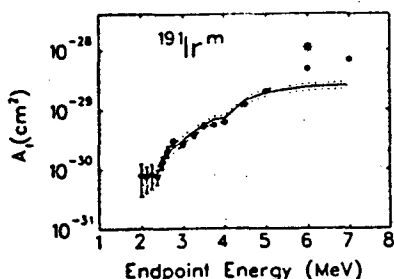


FIG. 7. Normalized yield  $A_f$  of the activation of  $^{191}\text{Ir}^m$  as a function of electron energy. The asterisk represents the experimental result of Ref. [8] obtained at 6 MeV. The solid line corresponds to the fit to the data, and its error bounds are given by the dotted lines.

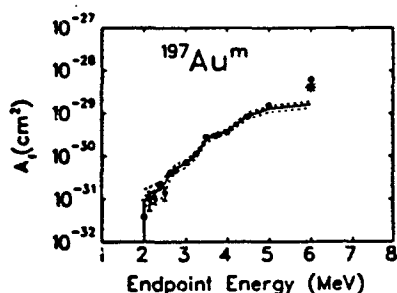


FIG. 8. Normalized yield  $A_f$  of the activation of  $^{197}\text{Au}^m$  as a function of electron energy. The asterisk represents the experimental result of Ref. [8] obtained at 6 MeV. The solid line corresponds to the fit to the data, and its error bounds are given by the dotted lines.

that within the energy errors given for the IS locations the present approach cannot distinguish between single states and contributions from fragmented strength.

#### IV. DISCUSSION

Examination of the results presented in Table II reveals some interesting phenomena. All four nuclei show a sudden jump of very significant magnitude in the values of integrated cross sections accessed around 2.5 MeV. This same phenomenology had been reported earlier [11–13] in  $^{180}\text{Ta}^m$ ,  $^{123}\text{Te}$ , and  $^{115}\text{In}$ . Confirmed for  $^{115}\text{In}$  by both studies of resonant scattering and unified model calculations, the IS strength there accrued from  $g_{9/2} \rightarrow g_{7/2}$  spin-flip transitions. However, in the present work, the chosen nuclei, together with the  $^{180}\text{Ta}^m$ , represent cases of both unpaired protons and unpaired neutrons in different major shells. A common mechanism independent of the details of nuclear structure would be indicated for this group of IS's.

Before attempting to find the means to explain such extraordinary strengths for these IS's, a first concern is the extent to which these measurements may be supported by prior work. Unfortunately, there are few compelling results in the literature. The only precedents are the recent measurements made over a very coarse mesh of energies [8] and the 1970 work of Johnson, Chertok, and Dick (JCD) [21]. The agreement is excellent between values of  $A_f$  obtained in the present work and those obtained with three of the four different accelerators employed previously [8]. No arbitrary factors were used to scale any of those earlier data, and the agreement seen in the Figs. 5–8 is a measure of the accuracy with which absolute measurements can be made for  $(\gamma, \gamma')$  reactions. Reference back to the original data of Ref. [8] shows that comparisons with activations produced by the fourth accelerator, a 4-MeV medical linac, were less satisfactory. With that device it was not possible either to monitor or control the end-point energy of the electrons, nominally fixed at 4.0 MeV. Because of the amount of structure now reported for activation curves near 4 MeV, the effects of small variations of end-point energy would be expected to be magnified in the resulting yields. Not surprisingly disagreements as great as a factor of 2 were obtained with that accelerator.

It is important to note that the experimental  $A_f$  value for  $^{191}\text{Ir}$  at  $E_0 = 6$  MeV in the present experiment is about a factor of 2 smaller than that in Ref. [8]. This magnitude of excitation agrees well with the empirical systematics discussed above. In addition, a corresponding reduction of the  $(\sigma\Gamma)_{\text{iso}}$  value for  $^{191}\text{Ir}$  plotted from Ref. [8] in Fig. 2(b) removes the deviation observed for this nucleus, which then fits very well into the  $N_p N_n$  systematics.

Comparisons with the JCD results are more difficult. Published in a Letter, both results and procedures were too briefly described to permit any repetition of the work. Details were promised for publication in a subsequent article which never appeared. Both the strengths and excitation energies of the IS reported by JCD disagree completely with those summarized in Table II. However, the

uniqueness of such values depends upon the degree to which inflections in curves of  $A_f$  as functions of endpoint energy can be precisely located. The fragments of data shown by JCD in the Letter are insufficient to support the uniqueness of the values they reported.

The degree to which the results of this work reported in Table II agree with prior measurements is best summarized in Fig. 9. There are plotted the values of  $A_f$  that were recently obtained in this work for the reaction  $^{167}\text{Er}(\gamma, \gamma')^{167}\text{Er}^m$  together with those from Ref. [8], including the one made with the 4-MeV linac of lessened reliability. No scale factors were used and absolute measurements have been plotted. From the JCD Letter, it is possible only to calculate values of  $A_f$  which would have resulted from excitation through the IS they report by bremsstrahlung with reasonable spectra. Since they did not report IS's below 2.5 MeV, a single hypothetical intermediate state had to be included in all computations of  $A_f$  to represent contributions from those lower energies. That state was chosen to give the closest agreement with the rest of the values plotted. The results are shown in Fig. 9, which now permits a comparison of all known measurements of the activation of  $^{167}\text{Er}(\gamma, \gamma')^{167}\text{Er}^m$  in the energy range from 2 to 7 MeV.

Agreement of the results of JCD from 20 years ago with the present work is at least as good as has been obtained with the 4-MeV medical linac, about a factor of 2. However, it is doubtful whether the procedures of Eq. (5) would deliver the same number and magnitudes of the IS reported by JCD if now applied to the corresponding data of Fig. 9. Values they reported were sufficient for the description of their measured  $A_f$ , but were not unique. Despite the generally favorable agreement of all of the measurements summarized in Fig. 9, we believe it reasonable to ascribe a greater weight to those from the current experiment. A primary consideration is that each exposure in the present work also included the activation of  $^{115}\text{In}(\gamma, \gamma')^{115}\text{In}^m$  believed now to be well un-

derstood from a unique level of agreement of photoexcitation, resonant scattering, and model interpretation. Through this constant recalibration, the effects of experimental uncertainties were minimized.

The resulting IS cross sections of Table II show a general tendency to increase with increasing excitation energy. We have investigated whether photoabsorption through the tail of the isovector electric giant dipole resonance (GDR) provides a quantitative explanation of the excitation functions. It is well known that the extrapolation of the GDR to lower energies describes  $\gamma$ -strength functions [22] and the statistical distribution of low-energy  $E1$  transitions [23] reasonably well. This extrapolation might be extended down to about 4–5 MeV in nuclei far from closed shells, but nuclei near the  $^{208}\text{Pb}$  shell closure show strong irregularities and experimental results tend to be significantly overestimated [22]. In this analysis we therefore show a comparison for both  $^{167}\text{Er}$  and  $^{197}\text{Au}$  as representative examples of the two groups.

The following simplifications are assumed for the calculations. The photoabsorption cross section is taken from the usual Lorentzian parametrization

$$\sigma_{\text{abs}}(E) = \sum_i \sigma_{\text{max}} \frac{E^2 \Gamma^2}{(E^2 - E_{\text{max}}^2)^2 + E^2 \Gamma^2}, \quad (6)$$

with  $E_{\text{max}}$  and  $\sigma_{\text{max}}$  being the energy and cross section at maximum, respectively, and  $\Gamma$  is the width. For spherical nuclei,  $i=1$ , and for deformed nuclei,  $i=1$  or 2, corresponding to oscillations with respect to the different axes. Equation (6) is substituted into Eq. (3) to obtain  $A_f$  values comparable to the experiment. In order to simplify the integral,  $\sigma_{\text{abs}}$  is described as a histogram with a mesh interval  $\Delta$  equal to the step size of the photon intensity function  $F(E, E_0)$ . Then the integral can again be reduced to a simple summation

$$A_f(E_0) = \sum_{i=1}^N F(E_i, E_0) \sigma(E_i - \Delta/2, E_i + \Delta/2), \quad (7)$$

with  $E_i = E_{i-1} + \Delta$ . The Lorentzian parameters were taken from Ref. [24], and the experimental results of  $^{167}\text{Er}$  were used for  $^{167}\text{Er}$ .

The results are shown in Fig. 10 as hatched areas above 3.5 MeV (model A). The upper and lower borders correspond to the limits of reasonable branching ratio values of  $b_0 b_{\text{iso}} = 0.05$  and 0.25. Below 3.5 MeV, results based on the single-particle model multiplied with an average experimentally deduced [25] hindrance factor of  $3 \times 10^{-5}$  (model C) are displayed. This approach has been tested by Zurmühl *et al.* [26] for various well-deformed heavy nuclei. Alternatively, an extrapolation of the GDR using an energy-dependent damping width of the form  $\Gamma(E) = \Gamma_{\text{max}}(E/E_{\text{max}})^\gamma$  has been proposed [27,28] with typical values  $\gamma = 1.5$ –2. As an example, we adopt the approach of Kopecky and Uhl [28] (with  $T=0$  since we measure the upward strength function), which is displayed as model B.

A comparison of the  $^{167}\text{Er}$  and  $^{197}\text{Au}$  results reveals considerable differences. In  $^{167}\text{Er}$ , model A provides a reasonable description slightly below particle threshold, while results of model B are much too small. On the con-

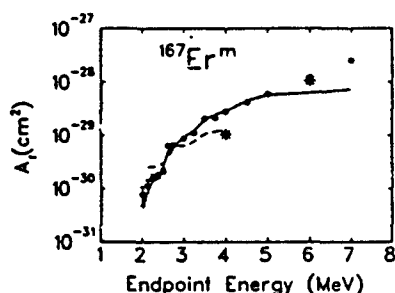


FIG. 9. Comparison of the present experiments with previous work for  $^{167}\text{Er}^m$ . The asterisks denote the  $A_f$  results of Ref. [8] attained at 4 and 6 MeV. The dashed curve was calculated with the intermediate states given in Ref. [21] plus an arbitrary state below 2.5 MeV to account for the unknown lower-energy contributions not covered in that early work. The energy  $E=1.9$  MeV and integrated cross section  $\sigma\Gamma=2250 \times 10^{-29}$   $\text{cm}^2 \text{keV}$  of this state were adjusted to achieve an optimum agreement with the present data in the 2.5–3.6-MeV region accessed in both experiments. The solid line indicates the fit to the current data obtained from Eq. (5).



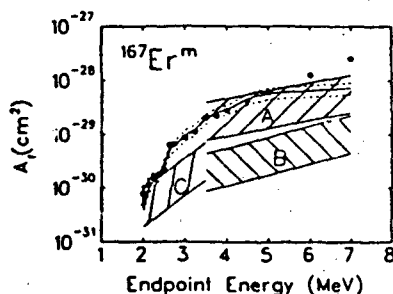


FIG. 10. Comparison of the  $^{167}\text{Er}^m$  excitation function with extrapolations of the photoabsorption through the tail of the GDR assuming a Lorentzian shape (model A) or a Lorentzian with an energy-dependent damping width (model B), and with a single-particle model (model C). The Lorentzian parameters were taken from Ref. [24]. The borders of the hatched regions showing the model predictions correspond to reasonable limits assumed for the unknown branching-ratio values  $b_0 b_{iso} = 0.25$  and  $0.05$ . The solid line corresponds to the fit to the data, and its error bounds are given by the dotted lines.

trary, as shown in Fig. 11, model A predicts too large photoabsorption cross sections in  $^{197}\text{Au}$ , in line with other investigations of the  $\gamma$ -strength function [22], while model B accounts well for the data down to about 4 MeV. It is also clear that an average  $E1$  transition strength (model C) could explain the low-energy data in this case.

The extraordinary photoabsorption strength around 2.5 MeV in  $^{167}\text{Er}$  is reflected by the failure of model C, which predicts values which are much too small. The empirical relation to the deformation parameter and IS parameters in Table II indicates that collective degrees of freedom should play a decisive role. However, recent studies of low-energy collective dipole strength in rare-earth nuclei [29–32] provide no fully satisfactory ex-

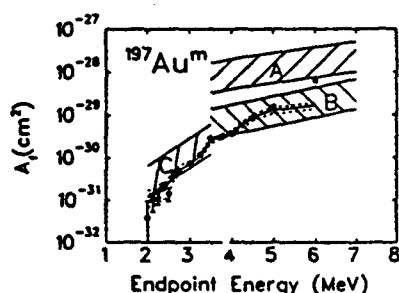


FIG. 11. Comparison of the  $^{197}\text{Au}^m$  excitation function with extrapolations of the photoabsorption through the tail of the GDR assuming a Lorentzian shape (model A) or a Lorentzian with an energy-dependent damping width (model B), and with a single-particle model (model C). The Lorentzian parameters were taken from Ref. [24]. The borders of the hatched regions showing the model predictions correspond to reasonable limits assumed for the unknown branching-ratio values  $b_0 b_{iso} = 0.25$  and  $0.05$ . The solid line corresponds to the fit to the data, and its error bounds are given by the dotted lines.

planation. For the IS at 2.5 MeV, reduced transition probabilities  $B(M1) = 3.6 \mu_N^2$  and  $B(E1) = 40 \times 10^{-3} e^2 \text{fm}^2$  can be extracted assuming a favorable  $b_0 b_{iso} = 0.2$ . These numbers roughly correspond to the total experimental  $M1$  and  $E1$  transition strengths [31,33] typically observed below 4 MeV in the experiments. However, all the above data have been taken in even-even nuclei. Recently, a first attempt to investigate low-lying dipole transitions in an odd-even case  $^{165}\text{Ho}$  was reported [34]. Only intrinsic single-particle transitions were excited with reasonable magnitude, and significant collective  $M1$  or  $E1$  strengths were not observed below 3 MeV.

The importance of the quadrupole deformation already suggested in Fig. 2(b) is clearly confirmed in the present results, if one compares the cross sections of different nuclei at about equal energies. The integrated isomer cross section of the  $j$ th IS can be related to photon-scattering results via

$$(\sigma\Gamma)_{iso} = \pi^2 \left( \frac{\hbar c}{E_\gamma} \right)^2 \left[ \frac{2J_f + 1}{2J_i + 1} \right] b_0 b_{iso} \Gamma, \quad (8)$$

with  $\Gamma$  being the total decay width of the IS. Here  $b_0$  is the direct IS to ground state branching ratio and  $b_{iso}$  stands for the sum of all branches populating the isomer, either directly or via a cascade. In order to remove the obvious excitation energy dependence contained in  $(\sigma\Gamma)_{iso}$ , it is useful to introduce the isomer population probabilities

$$S_j^D = \frac{(\sigma\Gamma)_{iso}^D}{E_j} \quad \text{and} \quad S_j^Q = \frac{(\sigma\Gamma)_{iso}^Q}{E_j^3}. \quad (9)$$

These quantities are proportional to the reduced transition probabilities for excitation for the  $j$ th IS assuming either a dipole ( $S^D$ ) or quadrupole ( $S^Q$ ) transition, multiplied by the branching ratio to the isomer. The spin statistics factor from Eq. (8) is neglected in this approach.

This definition permits a useful comparison between the contributions of IS's at different energies in one nucleus as well as between IS's of different nuclei. In Fig. 12 the summed isomer population probability  $S = \sum_j S_j$  for each nucleus is plotted versus the quadrupole deformation parameter  $\delta$  of the ground state that has been derived from measured moments [35]. The circles correspond to the assumption of dipole absorption by the IS and the squares to quadrupole excitations. Since the upward transitions might be of mixed character and the sums might include transitions of both types, the results shown for pure dipole and quadrupole cases should be considered as limits. Still, regardless of the assumed character of the IS excitation, the data show a correlation between  $S$  and  $\delta$ ; i.e. the isomer population probability increases with the ground-state deformation.

Nuclear resonance fluorescence work [29–34] in the rare-earth region has recently suggested that for energies below 4 MeV the absorption step is most likely mediated by dipole rather than quadrupole strength. Then a very simple linear relationship is indicated in Fig. 12. A fit assuming a direct proportionality of  $S$  and  $\delta$  is displayed as a solid line and describes the data very well.

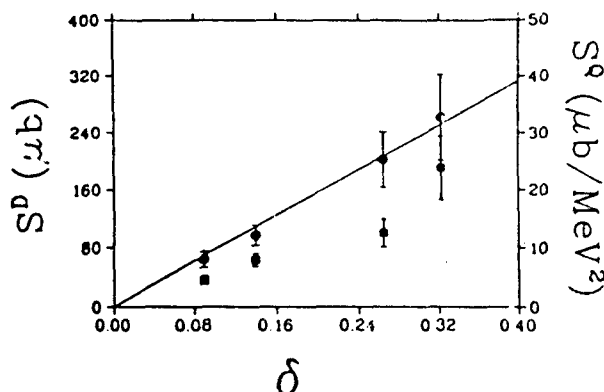


FIG. 12. Isomer excitation probability  $S$ , calculated from Eq. (9) and summed over the energy region 2–4.5 MeV versus the ground-state deformation parameter  $\delta$ . The circles correspond to the assumption of dipole excitations ( $S^D$ ) and are plotted according to the left ordinate. The squares correspond to quadrupole excitations ( $S^Q$ ) of the IS, plotted according to the right ordinate. The solid line is a best fit for the dipole results with a zero intercept.

At present, it remains open whether such a linear dependence is of physical significance or simply fortuitous. One should keep in mind several details: The results are a function of the excitation energy interval considered, the IS spin statistics factor might introduce variations of about a factor of 2 (see Table I), and the number of data points is certainly too small for a final conclusion. If one assumes quadrupole excitations, no simple functional form is suggested.

The extremely large integrated cross sections for the photoexcitation of well-deformed isomers are difficult to interpret in a single-particle model, and a puzzle of comparable complexity is found in the efficiency with which  $\Delta K$  is transferred. Many of these isomers have values of  $K$  that differ considerably from the ground-state values [ $\Delta K=8$  ( $^{180}\text{Ta}$ ),  $\Delta K=6$  ( $^{176}\text{Lu}$ ), and Table I]. The extraordinary integrated cross sections can only be explained with considerable  $K$  mixing in the IS wave function. While  $K$  mixing is common at neutron threshold energies [36], evidence for violation of  $K$  selection rules around 3 MeV has also been recently gained in nuclear resonance fluorescence investigations [37] and in a detailed decay study [38] of the  $K^\pi=14^+$ , 4- $\mu\text{s}$  isomer at 3.312 MeV in  $^{174}\text{Hf}$ .

It is an interesting speculation that at certain energies of excitation, collective oscillations of the core nucleons could break some of the symmetries upon which rest the identifications of the pure single-particle states. If

single-particle states of differing  $K$  were mixed in this way, the possibility for transferring larger amounts of  $\Delta K$  with greater partial widths might be enhanced. The similarity of results for odd-even as well as odd-odd nuclei with dissimilar single-particle structures might support the identification of this  $K$ -mixing process with some type of core property varying only slowly among neighboring nuclei.

## V. CONCLUSIONS

In the present work, the main IS's between 2 and 5 MeV have been identified for  $^{167}\text{Er}$ ,  $^{179}\text{Hf}$ ,  $^{191}\text{Ir}$ , and  $^{197}\text{Au}$ . A sudden jump of IS cross sections of typically more than an order of magnitude is observed in all cases around 2.5 MeV. This coincides with previous results in  $^{115}\text{In}$  [13],  $^{123}\text{Te}$  [12], and  $^{180}\text{Ta}$  [11], where similar phenomena were observed below 3 MeV, and indicates the presence of a common excitation mechanism.

The isomer population probability, defined as the sum of the reduced transition probabilities to the IS times the branching ratio of the IS to the isomer, reveals a correlation to the ground-state deformation regardless whether dipole or quadrupole excitations are assumed. If dipole transitions are solely responsible for the excitation (which can be justified from recent photon-scattering experiments in this mass region [29–34]), the data are well described by a linear dependence. While it is unclear at present whether this linear relation bears physical significance, the overall increase of the isomer population probability with deformation is undoubted and will be subject of further investigations, e.g., by nuclear resonance fluorescence studies.

At present, it remains an open question what might be the nuclear structure underlying the particularly strong IS below 3 MeV observed in  $^{167}\text{Er}$ ,  $^{176}\text{Lu}$ ,  $^{179}\text{Hf}$ , and  $^{180}\text{Ta}$  and whether a common excitation mechanism dominates or whether the detailed interplay of collective and single-particle aspects in each particular nucleus is responsible. Microscopic calculations are clearly needed.

## ACKNOWLEDGMENTS

We thank H.-D. Gräf, Th. Rietdorf, P. Schardt, and H. Weise for their great support in operating the superconducting electron accelerator, and M. L. Williams for his assistance in analyzing the data. In addition, we wish to thank our sponsors, the Department of Defense through the Naval Research Laboratory and the Bundesministerium für Forschung und Technologie, Contract No. 06DA1841.

- [1] B. Pontecorvo and A. Lazard, C. R. Acad. Sci. 208, 99 (1939).
- [2] G. B. Collins, B. Waldman, E. M. Stubblefield, and M. Goldhaber, Phys. Rev. 55, 507 (1939).
- [3] Z. M. Bigan, E. L. Lazarev, V. M. Mazur, and V. Sokolnyk, Yad. Fiz. 49, 913 (1989) [Sov. J. Nucl. Phys. 49, 567

- (1989)].
- [4] L. Z. Dzhilavyan, V. L. Kauts, V. I. Furman, and A. Y. Chaprikov, Yad. Fiz. 51, 336 (1990) [Sov. J. Nucl. Phys. 51, 215 (1990)].
- [5] E. C. Booth and J. Brownson, Nucl. Phys. A98, 529 (1967).
- [6] C. B. Collins, C. D. Eberhard, J. W. Glesener, and J. A.

- Anderson, Phys. Rev. C 37, 2267 (1988).
- [7] J. J. Carroll, J. A. Anderson, J. W. Glesener, C. D. Eberhard, and C. B. Collins, Astrophys. J. 344, 454 (1989).
- [8] J. J. Carroll, M. J. Byrd, D. G. Richmond, T. W. Sinor, K. N. Taylor, W. L. Hodge, Y. Paiss, C. D. Eberhard, J. A. Anderson, C. B. Collins, E. C. Scarbrough, P. P. Antich, F. J. Agee, D. Davis, G. A. Huttlin, K. G. Kerris, M. S. Litz, and D. A. Whittaker, Phys. Rev. C 43, 1238 (1991).
- [9] C. B. Collins, F. W. Lee, D. M. Shemwell, B. D. DePaola, S. Olariu, and I. I. Popescu, J. Appl. Phys. 53, 4645 (1982).
- [10] V. Ponomarev, A. P. Dubenskij, V. P. Dubenskij, and E. A. Boykova, J. Phys. G 16, 1727 (1990).
- [11] C. B. Collins, J. J. Carroll, T. W. Sinor, M. J. Byrd, D. G. Richmond, K. N. Taylor, M. Huber, N. Huxel, P. von Neumann-Cosel, A. Richter, C. Spieler, and W. Ziegler, Phys. Rev. C 42, 1813 (1990).
- [12] J. J. Carroll, T. W. Sinor, D. G. Richmond, K. N. Taylor, C. B. Collins, M. Huber, N. Huxel, P. von Neumann-Cosel, A. Richter, C. Spieler, and W. Ziegler, Phys. Rev. C 43, 897 (1991).
- [13] P. von Neumann-Cosel, A. Richter, C. Spieler, W. Ziegler, J. J. Carroll, T. W. Sinor, D. G. Richmond, K. N. Taylor, C. B. Collins, and K. Heyde, Phys. Lett. B 266, 9 (1991).
- [14] K. Heyde, P. van Isaker, M. Waroquier, J. L. Wood, and R. A. Mayer, Phys. Rep. 102, 291 (1983).
- [15] R. F. Casten, Nucl. Phys. A443, 1 (1985).
- [16] K. Alrutz-Ziemssen, D. Flasche, H.-D. Gräf, V. Huck, M. Knirsch, W. Lotz, A. Richter, T. Rietdorf, P. Schardt, E. Spamer, A. Staschek, W. Voigt, H. Weise, and W. Ziegler, Part. Accel. 29, 53 (1990).
- [17] A. Ljubicic, M. Pisk, and B. A. Logan, Phys. Rev. C 23, 2238 (1981); M. Krcmar, A. Ljubicic, B. A. Logan, and M. Bistrovic, *ibid.* 33, 293 (1986); M. Krcmar, S. Kaucic, T. Tustonic, A. Ljubicic, B. A. Logan, and M. Bistrovic, *ibid.* 41, 771 (1990).
- [18] P. von Neumann-Cosel, A. Richter, J. J. Carroll, and C. B. Collins, Phys. Rev. C 44, 554 (1991).
- [19] *Monte Carlo Transport of Photons and Electrons*, edited by T. M. Jenkins, W. R. Nelson, and A. Rindi (Plenum, New York, 1988).
- [20] E. Browne and R. B. Firestone, in *Table of Radioactive Isotopes* edited by V. S. Shirley (Wiley, New York, 1986); *Evaluated Nuclear Structure Data File* (Brookhaven National Laboratory, Upton, New York, 1986).
- [21] W. T. K. Johnson, B. T. Chertok, and C. E. Dick, Phys. Rev. Lett. 25, 599 (1970).
- [22] G. A. Bartholomew, E. D. Earle, A. J. Ferguson, J. W. Knowles, and M. A. Lone, Adv. Nucl. Phys. 7, 229 (1972).
- [23] M. Schumacher, U. Zurmühl, F. Smend, and R. Nolte, Nucl. Phys. A438, 493 (1985).
- [24] S. S. Dietrich and B. L. Berman, At. Data Nucl. Data Tables 38, 199 (1988).
- [25] P. M. Endt, At. Data Nucl. Data Tables 26, 47 (1981).
- [26] U. Zurmühl, P. Rullhusen, F. Smend, M. Schumacher, and H. G. Börner, Phys. Lett. 114B, 99 (1982).
- [27] G. Maino, A. Ventura, L. Zuffi, and F. Iachello, Phys. Rev. C 30, 2101 (1984).
- [28] J. Kopecky and M. Uhl, Phys. Rev. C 41, 1941 (1990).
- [29] C. Wesselborg, P. von Brentano, K. O. Zell, R. D. Heil, H. H. Pitz, U. E. P. Berg, U. Kneissl, S. Lindenstruth, U. Seemann, and R. Stock, Phys. Lett. B 207, 22 (1988).
- [30] H. H. Pitz, U. E. P. Berg, R. D. Heil, U. Kneissl, R. Stock, C. Wesselborg, and P. von Brentano, Nucl. Phys. A492, 411 (1989).
- [31] A. Zilges, P. von Brentano, C. Wesselborg, R. D. Heil, U. Kneissl, S. Lindenstruth, H. H. Pitz, U. Seemann, and R. Stock, Nucl. Phys. A507, 399 (1990).
- [32] W. Ziegler, C. Rangacharyulu, A. Richter, and C. Spieler, Phys. Rev. Lett. 65, 2515 (1990).
- [33] A. Zilges, P. von Brentano, H. Friedrichs, R. D. Heil, U. Kneissl, S. Lindenstruth, H. H. Pitz, and C. Wesselborg, Z. Phys. A 340, 155 (1991).
- [34] N. Huxel, W. Ahner, H. Diesener, P. von Neumann-Cosel, C. Rangacharyulu, A. Richter, C. Spieler, W. Ziegler, C. De Coster, and K. Heyde, Nucl. Phys. A539, 478 (1992).
- [35] P. Raghavan, At. Data Nucl. Data Tables 42, 189 (1989).
- [36] A. Bohr and B. Mottelson, *Nuclear Structure* (Benjamin, New York, 1975), Vol. 2, p. 37.
- [37] A. Zilges, P. von Brentano, A. Richter, R. D. Heil, U. Kneissl, H. H. Pitz, and C. Wesselborg, Phys. Rev. C 42, 1945 (1990).
- [38] P. M. Walker, F. Sletten, N. L. Glörup, M. A. Bentley, J. Borggreen, D. Fabricius, A. Holm, D. Howe, J. Pedersen, J. W. Roberts, and J. F. Sharpey-Schafer, Phys. Rev. Lett. 65, 416 (1990).

Reply to "Comment on 'Resonant excitation of the reaction  $^{180}\text{Ta}^m(\gamma, \gamma')^{180}\text{Ta}$ '"

J. J. Carroll,<sup>(1)</sup> C. B. Collins,<sup>(1)</sup> P. von Neumann-Cosel,<sup>(2)</sup> D. G. Richmond,<sup>(1)</sup> A. Richter,<sup>(2)</sup> T. W. Sinor,<sup>(1)</sup>  
and K. N. Taylor<sup>(1)</sup>

<sup>(1)</sup>Center for Quantum Electronics, The University of Texas at Dallas, P.O. Box 830688, Richardson,  
Texas 75083

<sup>(2)</sup>Institut für Kernphysik, Technische Hochschule Darmstadt, D-6100 Darmstadt, Germany

(Received 11 November 1991)

We reply to the preceding Comment.

PACS number(s): 21.10.Tg, 25.20.Dc, 95.30.Cq, 27.70.+q

The preceding Comment of Németh [1] raises three topics regarding the observation of intermediate states in the resonant  $^{180}\text{Ta}^m(\gamma, \gamma')^{180}\text{Ta}$  reaction [2] at 2.8 and 3.6 MeV with very large integrated cross sections of 1.2 and  $3.5 \times 10^{-25} \text{ cm}^2 \text{ keV}$ , respectively. These topics are (i) Németh assumes a summed branching ratio of ground state (g.s.) transitions of 0.01–0.001, from which he calculates the transition strengths of intermediate states (IS) to the isomer and concludes that the recommended upper limits (RUL) [3] for dipole transitions in this mass region would be significantly exceeded; (ii) he suggests that the bremsstrahlung spectra used in the data analysis might be wrong because the energies and strengths of IS in the  $^{87}\text{Sr}(\gamma, \gamma')^{87}\text{Sr}^m$  calibration reaction cannot be explained with the available nuclear structure data base; and (iii) he claims that the overall cross-section ratio of the photoactivation of  $^{180}\text{Ta}^m$  and  $^{115}\text{In}$  deduced from his own experiments at 1.33 and 4 MeV provides indirect evidence against the magnitude of the reported integrated cross sections.

(i) The estimates of transitions strengths to the  $^{180}\text{Ta}^m$  isomer (Table I of Ref. [1]) are indeed very large and their interpretation is a problem of considerable interest. However, the supposition of an effective g.s. branching ratio of 0.01–0.001 which would lead to a severe contradiction with the RUL is not justified in the present case. While the  $^{180}\text{Ta}$  low energy spectrum ( $\leq 1 \text{ MeV}$ ) is well characterized [4] as a rotator for which  $K$  conservation is fulfilled, there are good reasons to assume a breakdown of the  $K$  selection rule at higher energies.

Evidence for a strong admixture of different  $K$  values at energies around neutron thresholds has been derived from a statistical analysis of the widths of slow neutron capture resonances [5]. While the degree of completeness of the mixing is still a subject of discussion [6], the disappearance of  $K$  conservation at these energies is well established. Also, evidence for  $K$  mixing at excitation energies of about 3 MeV has recently emerged from nuclear resonance fluorescence (NRF) studies [7] and an investigation of the 3.312 MeV isomer in  $^{174}\text{Hf}$  [8].

The decay of the  $K = 14^+$ , 4  $\mu\text{s}$  isomer at 3.312 MeV in  $^{174}\text{Hf}$  provides a particularly impressive example of strong  $K$  mixing. Amongst the 20 transitions depopulating the state (see Table I of Ref. [8]) no relation to the final state  $K$  value can be observed. The strongest branch

has  $\Delta K = 8$ , and even  $\Delta K = 14$  transitions to the yrast band are seen with a probability  $> 1\%$ . In contrast, the minimum  $\Delta K = 2$  transitions contribute less than 20%. It is obvious that with a comparable mixing in the IS wave functions, the  $\Delta K = 8$  transfer from isomer to g.s. in  $^{180}\text{Ta}$  could be mediated very efficiently, perhaps even in a single step. The cascade from IS to g.s. needed for the spin transfer could then proceed through unhindered transitions.

The example of  $^{174}\text{Hf}$  is an even-even nucleus, so in the doubly odd  $^{180}\text{Ta}$  configuration mixing induced by the high level density should additionally amplify the  $K$ -transfer efficiency. A simple estimate of the level density, based on the backshifted Fermi gas model [9] and using parameters taken from the comparable  $^{182}\text{Ta}$  nucleus, shows that within the experimental uncertainty of  $\pm 1.0 \text{ MeV}$  for the 3.6 MeV state one finds approximately  $10^3$  states with  $J = 8$  (the IS spin assumed by Németh).

On the other hand, due to the configuration mixing a fragmentation of the principal transitions into several close lying levels is quite likely. Exactly such a behavior has been observed in a recent study [10] of the  $^{115}\text{In}(\gamma, \gamma')^{115}\text{In}^m$  reaction. Here, the isomer excitation function was compared to NRF data that fixed the g.s. branches. Numerous transitions were observed which clustered in two groups corresponding to the IS identified from the isomer photoactivation. The model interpretation strongly favored a common excitation mechanism and qualitatively reproduced the energy clustering [10]. If a similar distribution over several states occurs in  $^{180}\text{Ta}$ , the individual transitions would be well below the RUL and all concerns about unexpectedly large transition probabilities become unfounded.

We also note that the magnitudes of integrated cross sections reported in Ref. [2] are not singular cases. A recent investigation [11] of the photoactivation of short-lived isomers reveals two isotopes,  $^{167}\text{Er}$  and  $^{179}\text{Hf}$ , with similar values in the same 2.5–4 MeV excitation energy region.

(ii) Németh questions the calibration of the bremsstrahlung spectra obtained with the  $^{87}\text{Sr}(\gamma, \gamma')^{87}\text{Sr}^m$  reaction. He extracts the information available from the nuclear structure data base [12] on energies and strengths of IS in  $^{87}\text{Sr}$ . We agree that the available data upon branching ratios and half-lives explain neither the integrated cross

sections of the 1.88 MeV level detected by Booth and Brownson [13] and assumed in our calculation [2], nor of the 2.67 MeV level observed in both experiments. Németh's discussion indicates that the experimental cross sections might result from, respectively, three and two closely spaced levels instead of single ones. The photon spectral intensity distribution varies slowly with respect to the energy differences of the levels in question, so this would have little impact, certainly below 5%, on the overall normalization.

The finding that the IS identified by Németh cannot account for the experimental value raises the question whether all relevant states have been identified and whether the spectroscopic information on the decay branches is complete. As an example, one could conclude from unplaced  $\gamma$  transitions excited in the  $^{86}\text{Sr}(n,\gamma)^{87}\text{Sr}$  study of Winter *et al.* [14] that the 1.920 MeV level was populated and that an additional weak, previously unknown branch to the 1.253 MeV levels exists. Since this state decays 100% to the isomer, the additional contribution would effectively double the integrated cross section of the 1.920 MeV level. This would bring the results into much closer agreement with Refs. [2,13]. Also, the particular selectivity of different reaction types can preclude the detection of levels which are easily excited in resonant photoexcitation. We will not pursue this kind of speculation further, but instead point out two independent results which validate our confidence that both the spectral intensity distributions and the total fluxes of the bremsstrahlung spectra are correct.

The shapes of the bremsstrahlung spectra were extensively investigated [15,16] with a setup for NRF experiments [17] installed in the same experimental area as used for the work of Ref. [2]. Utilizing precisely determined [18] calibration states in  $^{27}\text{Al}$  and  $^{11}\text{B}$  distributed over the important energy region, the spectral distribution was investigated for various electron end-point energies, and very good correspondence to the Monte Carlo calculations was observed [15,16].

The absolute normalization was checked in a study [10] of the  $^{115}\text{In}(\gamma,\gamma')^{115}\text{In}^m$  reaction measured concurrently with  $^{180}\text{Ta}^m$  and  $^{87}\text{Sr}$ . In the  $^{115}\text{In}$  nucleus all relevant IS at excitation energies below the lowest bremsstrahlung end point of 2 MeV accessed in the present experiments are known from independent spectroscopic investigations [19]. The yields calculated from these parameters describe quite well our experimental data in the region from 2 to 2.75 MeV with only an overall normalization factor of 1.17. Considering the experimental errors of the input data as well as of our own experiments, this 17% deviation provides an extremely conservative estimate of the absolute normalization error of the total photon flux.

(iii) Finally, Németh claims that indirect evidence against the integrated cross section magnitudes in Ref. [2] is provided by a ratio of overall cross sections which he deduced in his own measurements of the  $^{180}\text{Ta}^m(\gamma,\gamma')^{180}\text{Ta}$  and  $^{115}\text{In}(\gamma,\gamma')^{115}\text{In}^m$  reactions at 4 MeV electron energy. While it is not clear from the Comment how the overall cross sections were calculated, we conclude from the context that it corresponds to the

normalized activation per unit photon flux  $A_f(E_0)$  defined in Eq. (2a) of Ref. [2]. It is related to the integrated cross sections  $(\sigma\Gamma)_f$  by

$$A_f(E_0) \equiv \frac{N_f}{N_i\phi_0} = \sum_j (\sigma\Gamma)_f F(E_j, E_0), \quad (1)$$

where  $N_i$  is the number of  $^{180}\text{Ta}^m$  ( $^{115}\text{In}$ ) target nuclei,  $N_f$  gives the  $^{180}\text{Ta}$  g.s. ( $^{115}\text{In}^m$  isomer) decays,  $\phi_0$  describes the total photon flux per  $\text{cm}^2$ ,  $F(E, E_0)$  is the normalized spectral intensity function, and  $E_j$  gives the resonance energy of the  $j$ th intermediate state. We note that the primary flux numbers strongly depend on the model approximations in the calculation of the photon spectra, and so  $A_f$  results from different experiments cannot be compared in a useful way.

With the data presented in Refs. [2,10] one can trivially extract the Ta/In overall cross-section ratio from Eq. (1). Németh's assertion that one could draw conclusions about the magnitudes of integrated cross sections from a knowledge of the overall cross-section ratio determined in a particular experiment at a particular electron end-point energy is simply untenable (except in the very special case in which both nuclei compared possess only one IS at nearly the same energy). It is clear from Eq. (1) that the experimental yields are proportional to the sum of products of integrated cross sections and the spectral intensities at different resonance energies. Thus, the yields obviously depend on the spectral intensity functions which differ at distinct experimental facilities. For example, in the present experiments a Ta/In cross-section ratio of  $\approx 12$  is deduced at 4 MeV, larger than that quoted by Németh. Due to the strong decrease of the number of photons within the bremsstrahlung spectrum as a function of energy, lower lying IS with smaller integrated cross sections can add significantly to the experimental activation. This is certainly more the case for  $^{115}\text{In}$  than for  $^{180}\text{Ta}^m$ .

In summary, we have shown that the reduced isomer transition probabilities extracted from the integrated cross sections in Ref. [2] can be well understood without a violation of the RUL. It has been discussed why the simple extension of  $K$  conservation to higher energies assumed by Németh in his estimates is not justified in the present case. The discrepancies between the coinciding results of Booth and Brownson and ourselves for the  $^{87}\text{Sr}(\gamma,\gamma')^{87}\text{Sr}^m$  calibration reaction and nuclear structure data from other reactions might be due to incomplete information about the important decay branches or due to the different selectivities of the reactions studied so far. We have presented independent experimental proof that both the total photon flux and the spectral distribution of the bremsstrahlung are well understood. The indirect evidence against the integrated cross-section magnitudes claimed by Németh is shown to be unfounded. Without a knowledge of the bremsstrahlung spectral shape and the energies of the IS, no information on possible integrated cross section values can be retrieved from the data presented by Németh.

What remains open is a microscopic understanding of the nuclear structure underlying the breakdown of  $K$  conservation and the strong coupling to the IS. The integrated cross sections deduced in recent experiments [2,11,20] for well-deformed nuclei with large  $\Delta K$  between g.s. and isomer demonstrate the usefulness of resonant photoexcitation as a tool for selective population of levels with

strongly  $K$ -mixed wave functions at low energies. Further experiments are clearly warranted.

We thank our sponsors, the Department of Defense through the Naval Research Office and the Bundesministerium für Forschung und Technologie (BMFT) under Contract No. 06DA1841.

- 
- [1] Zs. Németh, Phys. Rev. C **45**, 467 (1991), the preceding Comment.
  - [2] C. B. Collins, J. J. Carroll, T. W. Sinor, M. J. Byrd, D. G. Richmond, K. N. Taylor, M. Huber, N. Huxel, P. von Neumann-Cosel, A. Richter, C. Spieler, and W. Ziegler, Phys. Rev. C **42**, R1813 (1990).
  - [3] M. J. Martin, Nucl. Data Sheets, introductory material, p. ix.
  - [4] E. Warde, G. J. Costa, D. Magnac, R. Seltz, C. Gerardin, M. Buenerd, Ph. Martin, W. Spathoff, and C. A. Wiedner, Phys. Rev. C **27**, 98 (1983).
  - [5] A. Bohr and B. Mottelson, *Nuclear Structure* (Benjamin, New York, 1975). Vol. 2, p. 37f.
  - [6] J. Rekstad, T. S. Tvetter, and M. Guttormsen, Phys. Rev. Lett. **65**, 2122 (1990); **67**, 2236 (1991); P. G. Hansen, *ibid.* **67**, 2235 (1991).
  - [7] A. Zilges, P. von Brentano, A. Richter, R. D. Heil, U. Kneissl, H. H. Pitz, and C. Wesselborg, Phys. Rev. C **42**, 1945 (1990).
  - [8] P. M. Walker, G. Sletten, N. L. Gjørup, M. A. Bentley, J. Berggren, B. Fabricius, A. Holm, D. Howe, J. Pedersen, J. W. Roberts, and J. F. Sharpey-Schafer, Phys. Rev. Lett. **65**, 416 (1990).
  - [9] W. Dilg, W. Scharf, H. Vonach, and M. Uhl, Nucl. Phys. A **217**, 269 (1974).
  - [10] P. von Neumann-Cosel, A. Richter, C. Spieler, W. Ziegler, J. J. Carroll, T. W. Sinor, D. G. Richmond, K. N. Taylor, C. B. Collins, and K. Heyde, Phys. Lett. B **266**, 9 (1991).
  - [11] C. B. Collins, J. J. Carroll, D. G. Richmond, T. W. Sinor, K. N. Taylor, M. Huber, P. von Neumann-Cosel, A. Richter, and W. Ziegler, submitted to Phys. Rev. C.
  - [12] H. Sievers, Nucl. Data Sheets **62**, 327 (1991).
  - [13] E. C. Booth and J. Brownson, Nucl. Phys. A **98**, 529 (1967).
  - [14] C. Winter, B. Krusche, and K. P. Lieb, H. H. Schmidt, T. von Egidy, P. Hungerford, F. Hoyer, and H. G. Börner, Nucl. Phys. A **460**, 501 (1986).
  - [15] W. Ziegler, Ph.D. thesis, Technische Hochschule Darmstadt (1990).
  - [16] N. Huxel, W. Ahner, H. Diesener, P. von Neumann-Cosel, C. Rangacharyulu, A. Richter, C. Spieler, W. Ziegler, C. De Coster, and K. Heyde, submitted to Nucl. Phys. A.
  - [17] W. Ziegler, C. Rangacharyulu, A. Richter, and C. Spieler, Phys. Rev. Lett. **65**, 2515 (1990).
  - [18] P. M. Endt and C. van der Leun, Nucl. Phys. A **310**, 1 (1978); F. Ajzenberg-Selove, Nucl. Phys. A **433**, 1 (1985).
  - [19] J. Blachot and G. Marguier, Nucl. Data Sheets **52**, 565 (1987).
  - [20] J. J. Carroll, M. J. Byrd, D. G. Richmond, T. W. Sinor, K. N. Taylor, W. L. Hodge, Y. Paiss, C. D. Eberhard, J. A. Anderson, C. B. Collins, E. C. Scarbrough, P. P. Antich, F. J. Agee, D. Davis, G. A. Huttlin, K. G. Kerris, M. S. Litz, and D. A. Whittaker, Phys. Rev. C **43**, 1238 (1991).

# Structure of intermediate states in the photoexcitation of the $^{89}\text{Y}$ isomer\*

M. Huber, P. von Neumann-Cosel, A. Richter, C. Schlegel and R. Schulz  
*Institut für Kernphysik, Technische Hochschule Darmstadt,  
D-6100 Darmstadt, Germany*

J.J. Carroll, K.N. Taylor, D.G. Richmond, T.W. Sinor and C.B. Collins  
*Center for Quantum Electronics, The University of Texas at Dallas,  
TX 75083-0688 Richardson, Texas, USA*

V. Yu. Ponomarev  
*Laboratory of Theoretical Physics, Joint Institute for Nuclear Research, Dubna,  
Head Post Office, P.O. Box 79, Moscow, Russia*

**Abstract:** Resonant photon scattering off  $^{89}\text{Y}$  was investigated in a measurement of the  $^{89}\text{Y}^m$  excitation function for bremsstrahlung endpoint energies  $E_0 = 2 - 5$  MeV and in a nuclear resonance fluorescence experiment with  $E_0 = 5$  MeV. The results are compared to a quasiparticle-phonon model calculation. Besides a well known single particle M1 transition at low energies, the photoexcitation spectrum is governed by transitions to states built by coupling of the dominant  $p_{1/2}$  hole ground state configuration to collective quadrupole phonons in the neighbouring  $^{90}\text{Zr}$ . The detailed decay cascade to the isomer reproduces the experimental finding of only two intermediate states with about equal strength and explains the suppression of other possible transitions due to the nature of the particular E1 matrix element. The theoretical isomer branching ratios are small compared to the experiment, but depend critically on details of the model.

**NUCLEAR REACTIONS**  $^{89}\text{Y}(\gamma, \gamma')^{89}\text{Y}^m$ ,  $E_0 = 2 - 5$  MeV;  $^{89}\text{Y}(\gamma, \gamma')$ ,  $E_0 = 5$  MeV. Deduced ground state and isomer activation transition strengths,  $t_{1/2}$ . Quasiparticle-phonon model calculations.

---

\* Work supported by the German Federal Minister for Research and Technology (BMFT) under contract number 06DA641I and by the Department of Defense through the Naval Research Laboratory.

## 1. Introduction

The photoactivation of isomers has recently attracted considerable interest <sup>1-5</sup>). These studies have been motivated by several sources of interest. It has been proposed to use the population or depopulation of isomers by resonant photoabsorption as the basic mechanism for driving a  $\gamma$ -ray laser <sup>6</sup>). For feasibility studies, a much improved experimental data base is needed. Photon coupling between ground state (g.s.) and isomer plays an important role in nuclear astrophysics. As examples, photoactivation <sup>7</sup>) of  $^{176}\text{Lu}$  and the depopulation <sup>1</sup>) of  $^{180}\text{Ta}^m$  provide critical tests of the present understanding of the classical s-process <sup>8,9</sup>). Although experiments on the photoactivation of isomers have a 50 years history, surprisingly little is known about the structure of intermediate states (IS) responsible for the isomer feeding. An understanding of the nuclear structure is not only of interest by itself, but also a prerequisite for progress in the above described problems.

Most experimental photoactivation work has concentrated either on the low-energy area [see e.g. refs. <sup>10,11</sup>) and references therein]  $E \leq 2$  MeV, or on the giant resonance region <sup>12-14</sup>), where the statistical  $\gamma$ -decay properties and the competition with other emission channels can be tested. The work described in refs. <sup>1-5</sup>) focused on the energy region in between and produced a number of unexpected results. It was found that in heavy deformed nuclei the integrated cross sections (ICS) of IS can be many orders of magnitude larger <sup>1,5</sup>) than typically found in previous experiments, thereby implying considerable  $K$  mixing at low energies <sup>15</sup>). A particularly strong rise of ICS at excitation energies  $E_x = 2.5 - 3$  MeV is observed in almost all nuclei studied so far. The data also indicate a close correlation of absolute magnitudes of isomer population with the g.s. deformations <sup>5</sup>).

A first attempt to reach a detailed understanding of the IS nuclear structure was made in the investigation of  $^{115}\text{In}$ . Here, photoactivation and complementary nuclear resonance fluorescence (NRF) experiments were performed and the combined information turned out to be a powerful tool to constrain any microscopic model description <sup>4</sup>). The main features of both experiments could be successfully explained with a unified-model calculation <sup>16</sup>) and the dominant excitations could be extracted to be due to spin-flip  $g_{9/2} \rightarrow g_{7/2}$  magnetic dipole strength.

In the present work, we have extended this combined experimental method



to another example,  $^{89}\text{Y}^m$ . As for many nuclei in this mass region, the isomeric transition is of M4 type  $1/2^- \rightarrow 9/2^+$ . Complementary to the  $^{115}\text{In}$  case,  $^{89}\text{Y}$  has a  $J^\pi = 1/2^-$  g.s. and a  $J^\pi = 9/2^+$  isomer ( $E_{\text{iso}} = 0.909$  MeV). It provides an interesting case because of its semimagic nature. The reduced configuration space should facilitate the identification of the important nuclear structure aspects. Furthermore, additional information from spectroscopic studies with a variety of methods is available <sup>17)</sup> up to relatively high excitation energies. Photoactivation of  $^{89}\text{Y}^m$  was observed in the survey of ref. <sup>3)</sup> and the yields turned out to be very weak compared to other isomers in this mass region.

The results are compared to calculations with the quasiparticle-phonon model (QPM). The QPM has been extensively tested in odd-even nuclei and has been found to describe the main features of the spectra well <sup>18)</sup>. The QPM has already been successfully applied <sup>20)</sup> to explain the structure of IS in the photoactivation of  $^{81}\text{Br}$ . A QPM calculation for  $^{89}\text{Y}$  has been reported in ref. <sup>19)</sup>, but was restricted to a study of selected deep hole strength functions. The properties of the  $^{89}\text{Y}$  low-energy spectrum have been tested in a variety of other models like the broken-pair model <sup>21)</sup>, particle-core coupling <sup>22)</sup>, the cluster-phonon model <sup>23)</sup> and the shell model <sup>24)</sup>. However, the study of electromagnetic transitions has been restricted to the lowest states only <sup>21,23,24)</sup>.

## 2. Experiments and data analysis

The experiments were performed with the 10 MeV injector of the superconducting continuous wave electron accelerator S-DALINAC in Darmstadt <sup>25)</sup>. Figure 1 displays the experimental area for both measurements in more detail. The electron beam traversed through a 100  $\mu\text{m}$  Al exit window and impinged on a rotating 3 mm Ta converter disk for bremsstrahlung production. The electron beam alignment could be sensitively monitored with the dose delivered to an ionization chamber 2 m downstream which is shielded against background radiation and covers only 12 mrad around  $0^\circ$ .

### 2.1 NUCLEAR RESONANCE FLUORESCENCE EXPERIMENT

For the NRF experiment, a metallic Y powder target of 2.55 g sealed in a 0.1  $\text{mg}/\text{cm}^2$  polyethylene foil was placed behind the 60 cm lead collimator which

has a conical opening. The bremsstrahlung converter was moved to the position close to the collimator entrance indicated in fig. 1. The collimator defines a beam spot of  $2.5 \text{ cm}^2$  at the target position. The resonantly scattered photons were detected with a Ge(Li) and a HPGe detector, both 150 ccm, placed at  $90^\circ$  and  $127^\circ$ , respectively, relative to the beam axis. In the present experiment, only the  $127^\circ$  diode was used (see sec. 3). A graded shield of 9 mm Pb + 5 mm Cu was placed between target and detector in order to suppress the strong nonresonant low-energy background. Data were taken at  $E_0 = 5 \text{ MeV}$  with a typical average current of  $25 \mu\text{A}$ . The total measuring time was 32 h.

The energy calibration and relative efficiency of the Ge detector were determined off line with a  $^{56}\text{Co}$  source with a geometry identical to the target. During the measurement, thin disks of 1.05 g Al were sandwiched around the yttrium target. In  $^{27}\text{Al}$  a number of extremely well determined transitions  $^{26})$  are excited in the energy region of interest and serve as standards for the determination of the total photon flux.

The shape of the bremsstrahlung spectrum was taken from a Monte Carlo calculation with the code EGS4  $^{27})$ . From fig. 1 it is obvious that the experimental geometry is simple and reliable results from the Monte Carlo calculations can be expected. The calculated spectral shapes compare very well  $^{28,29})$  to the results for strong transitions in  $^{27}\text{Al}$  and  $^{11}\text{B}$  which are commonly used as standards. Further details of the data analysis are given in ref.  $^{28})$ .

From the line contents of identified transitions one obtains the ICS of the g.s. transitions  $(\sigma\Gamma)_0^i$  which are related to the characteristic properties of the excited state  $i$  by

$$(\sigma\Gamma)_0^i = \pi^2 \left( \frac{\hbar c}{E_i} \right)^2 \frac{2J_i + 1}{2J_0 + 1} \frac{(\Gamma_0^i)^2}{\Gamma} W(\Theta) . \quad (1)$$

Here,  $J_0$  and  $J_i$  are the spins of the g.s. and excited state, respectively,  $\Gamma_0^i$  is the partial width directly to the g.s.,  $\Gamma$  is the total width and  $E_i$  is the energy of the transition. The angular distribution  $W(\Theta)$  accounts for the nonisotropic decay which depends on the multipolarity (dipole/quadrupole) and the mixing ratio  $\delta$  of E2/M1 transitions.

## 2.2 ISOMER ACTIVATION EXPERIMENT

The experiment was performed as close as possible to the bremsstrahlung

converter in order to maximize the photon flux. The target consisted of an Al cylinder (diameter 1.4 cm, height 2.7 cm, walls 0.1 cm) filled with 4.8 g of  $\text{YF}_3$  powder. The cylinder was aligned to the beam direction with the front side in a distance of 1.3 cm to the converter. The sample was typically irradiated for a time duration of two half-lives ( $t_{1/2} = 16.06$  s) and then transported with a high compression rabbit system to a 3.5" NaI bore hole detector outside of the accelerator hall. Typically 5 to 9 cycles were performed per electron endpoint energy. Details of the measurement with this shuttle system are described in refs. <sup>5,30</sup>).

The absolute efficiency of the NaI detector was calculated with a Monte Carlo program which included the geometry of target cylinder and detector, the nonuniform distribution of activation over the length of the target and the selfabsorption of the signature transition in the target material.

The resulting isomer yield is given by

$$Y(E_o) = N_T \int_{E_c}^{E_o} \sigma(E) \frac{d\phi(E)}{dE} dE, \quad (2)$$

where  $\sigma(E)$  is the cross section,  $d\phi/dE$  is the time-integrated spectral intensity and  $N_T$  is the number of target atoms. The spectral intensity is again taken from EGS4 calculations and is conveniently expressed by

$$\frac{d\phi(E)}{dE} = \phi_o F(E, E_o) \quad (3)$$

with  $\phi_o$  being the total photon flux above a certain cutoff energy  $E_c$  in the calculation and  $F(E, E_o)$  is a relative intensity function normalized to unity.

The width of resonant intermediate states is typically small enough to assume that  $d\phi/dE$  is constant over the linewidth. Then eq. (2) can be simplified to

$$Y(E_o) = N_T \phi_o \sum_i (\sigma\Gamma)_{iso}^i F(E_i, E_o), \quad (4)$$

where  $(\sigma\Gamma)_{iso}^i$  is the ICS of the  $i^{\text{th}}$  level. We note that nonresonant contributions which would inhibit the use of eq. (4) are not considered, since the claims <sup>31</sup>) for important nonresonant contributions to the photoexcitation of isomers were recently shown to be unfounded <sup>32</sup>).

The integrated cross sections  $(\sigma\Gamma)_{iso}^i$  are related to eq. (1) by

$$(\sigma\Gamma)_{iso}^i = \pi^2 \left( \frac{\hbar c}{E_i} \right)^2 \frac{2J_i + 1}{2J_o + 1} \frac{\Gamma_o^i \Gamma_{iso}^i}{\Gamma} = (\sigma\Gamma)_o^i \frac{\Gamma_{iso}^i}{\Gamma_o^i W(\Theta)}. \quad (5)$$

Here,  $\Gamma_{iso}^i$  represents the sum of all partial widths of level  $i$  which decay to the isomer, either directly or via a cascade.

The validity of the above described data analysis procedures was tested with a measurement of  $^{115}\text{In}$ . It was shown in ref. <sup>4)</sup> that the isomeric yield below 2.8 MeV provides an absolute calibration of the total photon flux, since all activation levels are completely characterized in the literature <sup>33)</sup>. The present results agree within 5% with those of ref. <sup>4)</sup>, which were measured in a completely different geometry with a thin disk target, as well as with the 6 MeV result of ref. <sup>3)</sup>.

### 3. Results and discussion

#### 3.1. NUCLEAR RESONANCE FLUORESCENCE OF $^{89}\text{Y}$

A  $(\gamma, \gamma')$  spectrum taken at an endpoint energy  $E_0 = 5$  MeV is displayed in fig. 2. Except those levels marked as Al calibration lines, all visible transitions are assumed to be  $^{89}\text{Y}$  g.s. transitions. The observation of transitions to excited states can be excluded in the present case. Since NRF is restricted to dipole or quadrupole excitations, the lowest level which could be effectively populated would be at 1.507 MeV. Because of the correspondingly reduced  $\gamma$ -energy, such a transition is lost in the Compton background which rises exponentially towards lower energies.

A summary of all observed transitions is given in table 1 together with the available information <sup>17)</sup> on spins and g.s. branching ratios. In cases where both quantities are known, the resulting half-life is presented in the last column. For previously unknown levels, the partial g.s. width is given as  $g\Gamma_0^2/\Gamma$  with  $g = 2J + 1/2J_0 + 1$ .

Unlike the case of even-even nuclei where a two-point angular distribution allows a clear distinction between dipole and quadrupole transitions <sup>28)</sup> the possible angular distributions in an odd-even nucleus are much more isotropic. Therefore only measurements with the  $127^\circ$  detector which has a more favourable peak-to-background ratio were performed. For the angular correlations of  $^{89}\text{Y}$  g.s. transitions  $1/2 \rightarrow 1/2$ ,  $3/2$ ,  $5/2 \rightarrow 1/2$  the value of  $W(\Theta)$  at  $127^\circ$  averaged over the detector solid angle varies by less than 15% from  $W(\Theta) = 1$ . Thus, the  $W(\Theta)$  factor is omitted and for previously unknown levels an additional systematic error should be included. For an assigned  $5/2^-$  spin, the values in table 1 are corrected

with a factor  $W(\Theta) = 0.856$ . In the case of a  $3/2^-$  state, the maximum deviation from unity for an arbitrary E2/M1 mixing ratio is less than 4.5%.

The strongest transition observed in NRF is to a state at 1.508 MeV which has  $J^\pi = 3/2^-$ . Its almost pure  $p_{3/2}$  hole character is well established in single nucleon pick-up <sup>34)</sup> and  $(e,e')$  reaction <sup>35,36)</sup> studies. In an early  $(\gamma, \gamma')$  experiment <sup>37)</sup> a total width  $\Gamma = 22(3)$  meV was observed which compares favourably with the present value.

The 2.881 MeV and 3.067 MeV levels correspond to M1/E2 transitions. From a combination of the  $L = 1$  result in the  $(^3\text{He}, d)$  reaction <sup>38)</sup> and  $L = 2$  from inelastic  $(p, p')$  and  $(n, n')$  scattering <sup>39,40)</sup>,  $J^\pi = 3/2^-$  is clear. The refs. <sup>41,42)</sup> show that the 2.881 MeV state decays to the g.s. with a branching ratio  $b_0 \simeq 1$ . Including the results from sec. 3.2, we infer  $b_0 = 0.96$ .

The 3.107 MeV and 3.139 MeV states are likely  $J^\pi = 5/2^-$  candidates. The excitation of the 3.139 MeV state in the present experiment is very weak at the threshold of the detection sensitivity. It is, however, of interest because of its significant branch <sup>41,42)</sup> into a cascade to the isomer. It is noted that the  $B(E2)$  value of  $145 \text{ e}^2\text{fm}^4$  reported in ref. <sup>35)</sup> for the sum of the 3.067, 3.107 and 3.139 MeV levels unresolved in their  $(e, e')$  experiment is in good agreement with the present results, if one assumes a dominant E2 transition for the  $3/2^-$  state.

The strong 3.992 and 4.108 MeV states are again observed in inelastic nucleon scattering as  $L = 2$  states. From the available data one cannot distinguish between  $J^\pi = 3/2^-$  and  $5/2^-$ . A g.s. branching ratio of  $b_0 \simeq 1$  can be deduced for both states from refs. <sup>41,42)</sup>.

For the significantly excited 4.582 MeV transition, there is an uncertain correspondence to a  $L = 2$  level in the  $(^3\text{He}, d)$  reaction <sup>38)</sup>. If the same state is excited in  $(\gamma, \gamma')$ , the spin would be fixed to  $J^\pi = 3/2^+$ . A correspondence to the 4.588 MeV level detected in  $(p, p')$  can be excluded because of the octupole character required for the transition.

Beside this state, no candidate for an E1 transition is seen in the  $(\gamma, \gamma')$  data. For those  $3/2^-$  levels which are simultaneously observed in the  $(p, p')$  and  $(n, n')$  experiments, dominant E2 transition strength is suggested from the collective character of inelastic nucleon scattering reactions.

### 3.2 PHOTOACTIVATION OF $^{89}\text{Y}^m$

The isomer yield resulting from the bremsstrahlung irradiation is shown in fig. 3 as a function of the endpoint energy. Up to 2.875 MeV no isomer activity is detected. Towards higher energies, breaks of the excitation function are clearly visible just below 3 and around 4 MeV. The solid line results from a calculation assuming IS at 2.9 and 4.0 MeV with the ICS given in table 2.

The good agreement with the energies of states excited strongly in the  $(\gamma, \gamma')$  reaction together with the model results described in sec. 4 clearly suggests that the 2.881 MeV state is the first IS. The ICS of the weakly excited 3.139 MeV level is in any case too small to explain the first break. Because of the small number of data points the energy of the second IS is more uncertain and we cannot distinguish whether the 3.992 or the 4.170 MeV level provides the isomer population.

Compared to typical values of ICS in the energy region 2 - 4 MeV observed in refs. <sup>1,2,4,5</sup>), the isomer population in  $^{89}\text{Y}$  is weak. This finding is also in qualitative agreement with the yield values at 4 and 6 MeV deduced in ref. <sup>3</sup>). While the average  $(\sigma\Gamma)_0$  strength is even slightly higher than observed for  $^{115}\text{In}$  in ref. <sup>4</sup>), , the isomeric ratio  $\Gamma_{\text{iso}}/\Gamma_0 + \Gamma_{\text{iso}}$  is about an order-of-magnitude smaller.

## 4. Quasiparticle-phonon model calculations

### 4.1 OUTLINE OF THE MODEL

To understand the structure of states observed in the present experiments microscopic calculations within the quasiparticle-phonon model (QPM) have been performed. A detailed description of treating odd nuclei within this theoretical framework can be found in ref. <sup>18</sup>). Here, we only briefly outline the major ideas of this approach.

The simplest excitation modes in odd nuclei are described in terms of quasiparticle excitations of an odd system (proton or neutron) upon the ground state of the neighbouring even-even nucleus. In this picture, the ground state of an odd nucleus is considered as the quasiparticle state with the lowest energy. More complex modes of excitations are treated as quasiparticle configurations coupled to excitations of the even-even core, called phonons. Since these modes are mixed

in real nuclei, we write the wave function  $\Psi_\nu$  of the ground or excited states with angular momentum  $J$  and projection  $M$  in the following way

$$\Psi_\nu(JM) = C_J^\nu \left\{ \alpha_{JM}^\dagger + \sum_{\lambda\mu i} D_J^{\lambda i}(J\nu) [\alpha_{jm}^\dagger Q_{\lambda\mu i}^\dagger]_{JM} \right\} \Psi_0, \quad (6)$$

where  $\alpha_{jm}^\dagger$  is a quasiparticle creation operator,  $Q_{\lambda\mu i}^\dagger$  is a phonon creation operator with the momentum  $\lambda$ , projection  $\mu$  and the RPA-root number  $i$ ,  $\Psi_0$  is the ground state wave function of the even-even core and  $\nu$  is the number within a sequence of states with given  $J^\pi$ . In principle, following this scheme we have to include in the wave function more complex configurations as  $[\alpha^\dagger Q^\dagger Q^\dagger]$  or higher terms. But for the photoexcitation of levels from the ground state, in which the quasiparticle configuration has a dominant role, more complex configurations would only produce some fragmentation of strength.

Quasiparticle operators appear as a result of standard Bogolubov transformation from particle and hole creation operators. Thus, creation of a particle or a hole is considered as the creation of a quasiparticle. For the determination of occupation numbers we solve the BCS equations.

For phonons we consider both collective, such as  $2_1^+$  or  $3_1^-$ , and pure two-quasiparticle excitations of the core, and the phonon creation operator is introduced as

$$Q_{\lambda\mu i}^\dagger = \frac{1}{2} \sum_{jj'}^{N,Z} \{ \psi_{jj'}^{\lambda i} [\alpha_{jm}^\dagger \alpha_{j'm'}^\dagger]_{\lambda\mu} + (-1)^{\lambda-\mu} \phi_{jj'}^{\lambda i} [\alpha_{jm} \alpha_{j'm'}]_{\lambda-\mu} \}. \quad (7)$$

To obtain a phonon basis we diagonalize an effective Hamiltonian which includes an average field, pairing interaction and residual interaction between quasiparticles within the set of one-phonon wave functions. For the residual interaction we use the separable form with the Bohr-Mottelson radial dependence. Solving the RPA equations for all  $\lambda^\pi$  in eq. (6) we get a spectrum of the core excitations with the corresponding RPA-root number  $i$  and the structure of these excitations, i.e. the coefficients  $\psi_{jj'}^{\lambda i}$  and  $\phi_{jj'}^{\lambda i}$  in eq. (7).

Diagonalization of the Hamiltonian with the set of wave functions of eq. (6) leads to equations for the odd nucleus. From these equations we obtain a spectrum and the contributions of quasiparticle and "quasiparticle $\otimes$ phonon" configurations to the wave function of each excited state, viz. the coefficients  $C_J^\nu$  and  $D_J^{\lambda i}$  in eq. (6).

Numerically, equations for  $^{89}\text{Y}$  have been solved by use of the computer code PHOQUS<sup>43</sup>). The average field was treated by a Woods-Saxon potential with

parameters from ref. <sup>44</sup>). For the quasiparticle spectrum we have considered all bound and quasi-bound levels with small widths resulting from this potential. Parameters of the residual interaction were adjusted to reproduce the experimental position and the  $B(E\lambda)$  values of the  $2_1^+$  and  $3_1^-$  states in  $^{90}\text{Zr}$  while dealing with hole excitations and for  $^{88}\text{Sr}$  in case of particle excitations. Natural parity phonons with  $\lambda^\pi = 1^- - 6^+$  have been included in the second term of eq. (6). We have taken into account "quasiparticle $\otimes$ phonon" configurations up to an excitation energy of 12 MeV. Nevertheless, actual calculations show that only collective 2 phonons play an important role in the description of photoexcitation of states up to 5 MeV, since the interaction between different configurations is not strong in this nucleus.

#### 4.2 COMPARISON TO NUCLEAR RESONANCE FLUORESCENCE RESULTS

The calculated  $(\gamma, \gamma')$  excitation strength is presented in fig. 4 together with the experimental  $(\sigma\Gamma)_0$  data. In the QPM only 6 sizeable transitions are found below 4.5 MeV. Due to the restriction of the model space to one-phonon coupled states the degree of fragmentation is less than indicated by the experimental results. However, since higher phonon configurations do not contribute additional photoexcitation strength, the main features of the  $(\gamma, \gamma')$  results can already be explained in the one-phonon approximation.

The two lowest states in the calculation at 1.540 and 1.838 MeV correspond to the well known lowest  $J^\pi = 3/2^-$  and  $5/2^-$  states which have been shown <sup>34</sup>) to be of dominant  $p_{3/2}$  and  $f_{5/2}$  single-hole structures, respectively. The model result for the  $3/2^-$  level  $(\sigma\Gamma)_0 = 70.2$  eVb is in excellent agreement with experiment. The somewhat larger calculated E2/M1 mixing ratio of  $|\delta| = 0.254$  compared to the experimental value  $\delta = -0.139$  is probably due to a slight overprediction of the admixture of the  $[p_{1/2} \otimes 2_1^+]_{3/2^-}$  configuration which enlarges the E2 contribution. The  $5/2^-$  state was not observed in the experiment. One can calculate from the available data <sup>17</sup>) a g.s. transition strength of  $(\sigma\Gamma)_0 = 4.67$  eVb which converted to an experimental count rate is smaller than the background fluctuation.

The next transitions are in two groups of nearly degenerate levels which result from the coupling of the g.s. configuration to the lowest collective phonons <sup>45</sup>) in the neighbouring even-even nucleus  $^{90}\text{Zr}$ , i.e. dominant  $[p_{1/2} \otimes 2_{1,3}^+]_{3/2^-, 5/2^-}$



structure. One should note that the nearly degenerate excitation energies are the result of neglecting more complex configurations and would probably be removed if one included two-phonon states.

The 3.147 MeV,  $J^\pi = 3/2^-$  model state corresponds to the experimental 2.881 MeV and probably the 3.067 MeV state. The magnitudes of ICS support this assignment. The  $5/2^-$  model state can be reasonably compared to the more fragmented experimental strength up to 3.5 MeV. The levels resulting from the  $2_3^+$  state can be identified with the experimental levels at 3.992 and 4.170 MeV.

The structure of these states implies that the phonon transitions are responsible for the  $(\gamma, \gamma')$  strength. Accordingly, the  $1/2^- \rightarrow 3/2^-$  transitions display a dominant E2 character. The lower  $3/2^-$  state has also some M1 strength because of a 8% admixture of the  $p_{1/2}$  single hole component to the wave function. The general dominance of collective E2 strength explains the close correspondence to inelastic nucleon scattering results discussed in sec. 3.

The experimental 4.582 MeV state cannot be understood within the present model space. A likely explanation could be a single particle transition. It is well established <sup>18)</sup> that in the damping substantial fragments of high-lying single particle or deep hole strength can be pushed to lower energies. Examples for <sup>89</sup>Y can be found in ref. <sup>19)</sup>. From the possible correspondence to a  $L = 2$  state in the (<sup>3</sup>He,d) reaction discussed before one could speculate this to be a  $p_{1/2} \rightarrow d_{3/2}$  E1 transition.

#### 4.3 COMPARISON TO ISOMER ACTIVATION RESULTS

Since the relevant excitation spectrum is entirely explained assuming M1 and E2 transitions, for a total M4 transfer the intermediate state decay must proceed in a two-step cascade including an E1 transition for the parity change. Figure 5 presents a selected scheme of levels from the QPM calculations which fulfill the condition. The first step in the cascade to the isomer is limited to  $5/2^+$  final states and two are found in the energy region considered.

While the g.s. partial widths are comparable for  $3/2^-$  and  $5/2^-$  states, large differences are observed in the population of the  $5/2^+$  states. The decay to the higher model state at 3.308 MeV is extremely weak due to its almost pure  $[p_{1/2} \otimes 3_1^-]_{5/2^+}$  character which restricts to a strongly suppressed  $2_1^+ \rightarrow 3_1^-$  phonon

transition. The  $3/2^-$  levels have a small, but sizeable width to the lower  $5/2^+$  state. The decay widths of the  $5/2^-$  states to the same  $5/2^+$  state are much weaker because the reduced matrix elements of the E1 transition  $\langle 5/2^+ \parallel E1 \parallel 5/2^- \rangle_{Z,N} = 0.280, 0.295$  for the proton and neutron parts, respectively, are about an order of magnitude smaller than  $\langle 5/2^+ \parallel E1 \parallel 3/2^- \rangle_{Z,N} = 2.930, 3.063$ .

Since the lowest  $5/2^+$  state is strongly coupled to the isomer via a large  $[g_{9/2} \otimes 2_1^+]$  component in the wave function, the transitions from the  $3/2^-$  states are responsible for the isomer population. This result is in full agreement with the experimental finding of only two IS with about equal strength as well as with the deduced energies. If one compares with the experimental isomer branching ratios  $b_{iso} \approx 0.05$ , the calculated widths are roughly two orders of magnitude smaller. However, these values are very sensitive to details of the calculations. One deals with E1 transitions between weak quasiparticle configurations in the wave functions of both, the  $3/2^-$  and the  $5/2^+$  states. Contrary to the process of photoexcitation, in which only the main configurations of the wave function determine the magnitude of the cross sections, for the particular case of  $3/2^- \rightarrow 5/2^+$  transitions we need a correct description of the weak amplitudes. The other critical point is that the proton and neutron parts of the total E1 transition operator practically cancel each other. We have used for the effective charge the values  $e_n^{eff}(E1) = -Z/A$  and  $e_p^{eff}(E1) = N/A$  to separate the central mass motion. Close values of the effective charges with different signs together with nearly equal values of the  $\langle 5/2^+ \parallel E1 \parallel 3/2^- \rangle_{Z,N}$  matrix elements (see above) result in a strong cancellation.

## 5. Conclusions

The photoexcitation of  $^{89}\text{Y}$  was investigated with two different methods. NRF data were measured at  $E_o = 5$  MeV and states up to excitation energies of 4.6 MeV could be identified. The  $^{89}\text{Y}^m$  excitation function for  $E_o = 2 - 5$  MeV revealed no activity up to 2.9 MeV and only two IS were found up to 5 MeV.

The  $(\gamma, \gamma')$  transitions can be explained with a QPM calculation as the coupling of collective phonons in the neighbouring  $^{90}\text{Zr}$  with the  $p_{1/2}$  hole g.s. configuration leading to groups of  $3/2^-$ ,  $5/2^-$  states. While the total electromagnetic transition strength agrees favourably, the experimental fragmentation is underestimated due to the model's restriction to one-phonon coupled states. The omis-

sion of more complex (two- and higher phonon) configurations is justified for the present problem, since they do not add additional electromagnetic strength. Besides a well known low-lying single particle M1 transition, the excitation is governed by E2 phonon transitions.

The calculations demonstrate that the cascade needed for the activation of  $^{89}\text{Y}^m$  proceeds via the lowest  $5/2^+$  state which decays almost exclusively to the isomer. The experimental finding of only two IS at about 2.9 and 4.0 MeV is verified and the coupling to the  $5/2^+$  state is of single particle E1 character. Due to the nature of the transition matrix elements, in each group of  $[p_{1/2} \otimes 2^+]_{3/2^-, 5/2^-}$  states the  $5/2^- \rightarrow 5/2^+$  transitions are suppressed by more than two orders of magnitude with respect to the  $3/2^- \rightarrow 5/2^+$  transitions. The calculated branching ratios are small compared to the experiment. However, the corresponding transitions depend critically on weak quasiparticle components of the wave function as well as a near canceling of the proton and neutron contributions to the E1 reduced matrix element.

One can conclude that up to energies of about 5 MeV the main features of the electromagnetic excitation as well the decay of the excited states to the  $^{89}\text{Y}$  isomer are now understood. The usefulness of a combination of NRF and isomer activation experiments has again been proven as a powerful tool for nuclear structure studies.

We thank H.-D. Gräf and H. Weise for their great support in operating the accelerator. We are indebted to W. Ziegler for his help in the experiment. One of us (V.Yu.P.) would like to thank the members of the S-DALINAC group for their hospitality during his stay in Darmstadt.

## References

- [1] C.B. Collins, J.J. Carroll, T.W. Sinor, M.J. Byrd, D.G. Richmond, K.N. Taylor, M. Huber, N. Huxel, P. von Neumann-Cosel, A. Richter, C. Spieler and W. Ziegler, *Phys. Rev. C* **42** (1990) R1813
- [2] J.J. Carroll, T.W. Sinor, D.G. Richmond, K.N. Taylor, C.B. Collins, M. Huber, N. Huxel, P. von Neumann-Cosel, A. Richter, C. Spieler and W. Ziegler, *Phys. Rev. C* **43** (1991) 897
- [3] J.J. Carroll, M.J. Byrd, D.G. Richmond, T.W. Sinor, K.N. Taylor, W.L. Hodge, Y. Paiss, C.D. Eberhard, J.A. Anderson, C.B. Collins, E.C. Scarbrough, P.P. Antich, F.J. Agee, D. Davis, G.A. Huttlin, K.G. Keris, M.S. Litz and D.A. Whittacker, *Phys. Rev. C* **43** (1991) 1238
- [4] P. von Neumann-Cosel, A. Richter, C. Spieler, W. Ziegler, J.J. Carroll, T.W. Sinor, D.G. Richmond, K.N. Taylor, C.B. Collins and K. Heyde, *Phys. Lett. B* **266** (1991) 9
- [5] C.B. Collins, J.J. Carroll, K.N. Taylor, D.G. Richmond, T.W. Sinor, M. Huber, P. von Neumann-Cosel, A. Richter and W. Ziegler, submitted to *Phys. Rev. C*
- [6] C.B. Collins, F.W. Lee, D.M. Shemwall, B.D. DePaola, S. Olariu and I.I. Popescu, *J. Appl. Phys.* **53** (1982) 4645
- [7] N. Klay, F. Käppeler, H. Beer and G. Schatz, *Phys. Rev C* **44** (1991) 2839;  
K.T. Lesko, E.B. Norman, R.-M. Larimer, B. Sur and C.B. Beausang, *ibid* 2850
- [8] F. Käppeler, H. Beer and K. Wisshak, *Rep. Prog. Phys.* **52** (1989) 945
- [9] J.J. Carroll, J.A. Anderson, J.W. Glesener, C.D. Eberhard and C.B. Collins, *Astroph. J.* **344** (1989) 454
- [10] E.C. Booth and J. Brownson, *Nucl. Phys. A* **98** (1967) 529
- [11] Á. Veres, *At. Energy Rev.* **18** (1980) 281

- [12] Z.M. Bigan, E.L. Lazarev, V.M. Mazur and V. Sokolnyk, Sov. J. Nucl. Phys. 49 (1989) 567
- [13] L.Z. Dzhilavyan, V.L. Kauts, V.I. Furman and A.Y. Chaprikov, Sov. J. Nucl. Phys. 51 (1990) 215
- [14] J. Sáfár, H. Kaji, K. Yoshihara, L. Lakosi and Á. Veres, Phys. Rev. C44 (1991) 1086
- [15] J.J. Carroll, C.B. Collins, P. von Neumann-Cosel, D.G. Richmond, A. Richter, T.W. Sinor and K.N. Taylor, Phys. Rev. C45 (1992) 470
- [16] K. Heyde, P. Van Isacker, M. Waroquier, J.L. Wood and R.A. Mayer, Phys. Rep. 102 (1983) 291
- [17] H. Sievers, Nucl. Data Sheets 58 (1989) 351
- [18] S. Galès, Ch. Stoyanov and A.I. Vdovin, Phys. Rep. 166 (1988) 125
- [19] A.I. Vdovin and Ch. Stoyanov, Sov. J. Nucl. Phys. 40 (1985) 725
- [20] V.Yu. Ponomarev, A.P. Dubenskij, V.P. Dubenskij and E.A. Boykova, J. Phys. G16 (1990) 1727
- [21] P. Hofstra and K. Allaart, Z. Phys. A292 (1979) 159
- [22] S.M. Abecasis, J. Davidson and M. Davidson, Phys. Rev. C22 (1980) 2237
- [23] C.A. Heras and S.M. Abecasis, Phys. Rev. C27 (1983) 1765
- [24] X. Ji and B.H. Wildenthal, Phys. Rev. C38 (1988) 2849
- [25] K. Alrutz-Ziemssen, D. Flasche, H.-D. Gräf, V. Huck, M. Knirsch, W. Lotz, A. Richter, T. Rietdorf, P. Schardt, E. Spamer, A. Staschek, W. Voigt, H. Weise and W. Ziegler, Part. Acc. 29 (1990) 53
- [26] P.M. Endt, Nucl. Phys. A521 (1990) 200
- [27] W.R. Nelson, H. Hirayama and D.W.O. Rogers, Stanford Linear Accelerator Report 265 (1985)
- [28] W. Ziegler, Dissertation, Technische Hochschule Darmstadt (1990)

- [29] N. Huxel, Diploma thesis, Technische Hochschule Darmstadt (1992)
- [30] M. Huber, Diploma thesis, Technische Hochschule Darmstadt (1992)
- [31] A. Ljubičić, M. Pisk and B.A. Logan, Phys. Rev. **C23** (1981) 2238;  
M. Krčmar, A. Ljubičić, B.A. Logan and M. Bistrovic, Phys. Rev. **C33**  
(1986) 293;  
M. Krčmar, S. Kaučić, T. Tustonić, A. Ljubičić, B.A. Logan and M.  
Bistrovic, Phys. Rev. **C41** (1990) 771
- [32] P. von Neumann-Cosel, A. Richter, J.J. Carroll and C.B. Collins, Phys.  
Rev. **C44** (1991) 554
- [33] J. Blachot and G. Marguier, Nucl. Data Sheets **52** (1987) 565
- [34] A. Stuirbank, G.J. Wagner, K.T. Knöpfle, L.K. Pao, G. Mairle, H.  
Riedesel, K. Schindler, V. Bechtold and L. Friedrich, Z. Phys. **A297**  
(1980) 307
- [35] S.P. Fivozinskij, S. Penner, J.W. Lightbody Jr. and D. Blum, Phys.  
Rev. **C9** (1974) 1533
- [36] J.E. Wise, F.W. Hersman, J.H. Heisenberg, T.E. Milliman, J.P. Con-  
nelly, J.R. Calarco and C.N. Papanicolas, Phys. Rev. **C42** (1990) 1077
- [37] W.J. Alston III, H.H. Wilson and E.C. Booth, Nucl. Phys. **A116** (1968)  
281
- [38] G. Vourvopoulos, R. Shoup and B.A. Brown, Nucl. Phys. **A174** (1971)  
581
- [39] J. Hulstman, H.P. Blok, J. Verburg, J.G. Hoogteyling, C.B. Nederveen,  
H.T. Vijlbrief, E.J. Kapstein, S.W. Milo and J. Blok, Nucl. Phys. **A251**  
(1975) 269
- [40] Y. Yiming, C.E. Brient, R.W. Finlay, G. Randers-Pehrson, A.  
Marcinkowski, R.C. Taylor and J. Rapaport, Nucl. Phys. **A390** (1982)  
449
- [41] C. Nardelli, P. Pavan and G. Tornielli, Lett. Nuovo. Cim. **38** (1983) 129

- [42] C. Budtz-Jørgensen, P. Guenther, A. Smith, J. Whalen, W.C. McMurray, M.J. Renan and I.J. van Heerden, Z. Phys. A319 (1984) 47
- [43] Ch. Stoyanov and C.Z. Khuong, Preprint JINR Dubna P-4-81-234 (1981)
- [44] V.Yu. Ponomarev, V.G. Soloviev, Ch. Stoyanov and A.I. Vdovin, Nucl. Phys. A323 (1979) 446
- [45] P.M. Endt, At. Data Nucl. Data Tables 23 (1979) 547

# Table 1

TABLE 1. Transitions in  $^{89}\text{Y}(\gamma, \gamma')$ .

$E_x$ (keV)	$(\sigma\Gamma)_0$ (eVb)	$g\Gamma_0^2/\Gamma$ (meV)	$J^\pi$ [from ref. <sup>17</sup> ]	$b_0$	$t_{1/2}$ (fs)
1507.2(1)	64.5(36)		3/2 <sup>-</sup>	1.00	23.9 <sup>+2.5</sup> <sub>-2.1</sub>
2881.6(1)	19.6(12)		3/2 <sup>-</sup>	0.96 <sup>a)</sup>	19.9 <sup>+2.1</sup> <sub>-1.9</sub>
3067.0(3)	8.2(17)		3/2 <sup>-</sup>	1.00	45.0 <sup>+1.5</sup> <sub>-1.1</sub>
3106.9(6)	4.0(22)		5/2 <sup>-</sup>	0.87	100 <sup>+130</sup> <sub>-35</sub>
3139.0(5)	2.9(11)		5/2 <sup>-</sup>	0.78	110 <sup>+70</sup> <sub>-30</sub>
3396.1(3)	11.7(19)	35(6)			
3445.3(3)	5.8(9)	18(3)			
3480.3(5)	6.8(24)	21(8)			
3515.6(6)	2.4(11)	8(4)	3/2 <sup>-</sup> , 5/2 <sup>-</sup>		
3660.0(5)	6.7(18)	23(6)			
3898.6(5)	6.1(12)	24(5)			
3991.8(3)	22.4(25)	93(10)	3/2 <sup>-</sup> , 5/2 <sup>-</sup>	0.95 <sup>b)</sup> , 1.00 <sup>c)</sup>	9.3 <sup>+1.1</sup> <sub>-1.0</sub> <sup>b)</sup> , 12.6 <sup>+1.6</sup> <sub>-1.3</sub> <sup>c)</sup>
4069.8(8)	1.0(6)	4(3)			
4170.2(4)	25.5(31)	115(14)	3/2 <sup>-</sup> , 5/2 <sup>-</sup>	0.95 <sup>b)</sup> , 1.00 <sup>c)</sup>	7.5 <sup>+1.0</sup> <sub>-0.8</sub> <sup>b)</sup> , 10.1 <sup>+1.5</sup> <sub>-1.1</sub> <sup>c)</sup>
4581.2(7)	18.5(45)	101(25)			

<sup>a)</sup> Isomeric branching ratio from sec. 3.2

<sup>b)</sup> If  $J^\pi = \frac{3}{2}^-$  with isomeric branching ratios from sec. 3.2

<sup>c)</sup> If  $J^\pi = \frac{5}{2}^-$



# Table 2

TABLE 2. Intermediate states in the photoactivation of  $^{89}\text{Y}^{\text{m}}$ .

$E_x$ (MeV)	$(\sigma\Gamma)_{\text{iso}}$ (eVb)
2.9(1)	0.8(1)
4.0(2)	1.2(5)

## Figure Captions

**Fig. 1.** Schematic, but in-scale view of the experimental area for nuclear resonance fluorescence and photoactivation studies. Note the different positions of the bremsstrahlung converter (close to the collimator for NRF) for the two types of experiments.

**Fig. 2.** Spectrum of the  $^{89}\text{Y}(\gamma, \gamma')$  reaction at an endpoint energy  $E_0 = 5$  MeV.

**Fig. 3.** The  $^{89}\text{Y}$  isomer yield as a function of the bremsstrahlung endpoint energy. The solid line results from eq. (4) using the intermediate states of table 2.

**Fig. 4.** Comparison of the experimental integrated cross sections  $(\sigma\Gamma)_0$  of g.s. transitions in the  $^{89}\text{Y}(\gamma, \gamma')$  reaction with QPM calculations. The experimental spin assignments are from ref. <sup>17</sup>).

**Fig. 5.** Selected scheme of levels and partial decay widths from the QPM results for  $^{89}\text{Y}$ . The graph is restricted to states relevant to the photoexcitation of  $^{89}\text{Y}^m$ . The levels are split in  $J^\pi = 3/2^-$  states in the left column,  $J^\pi = 5/2^-$  states in the right column and positive parity states in the middle. The decay widths are given in meV. Weak transitions are denoted by dashed lines.

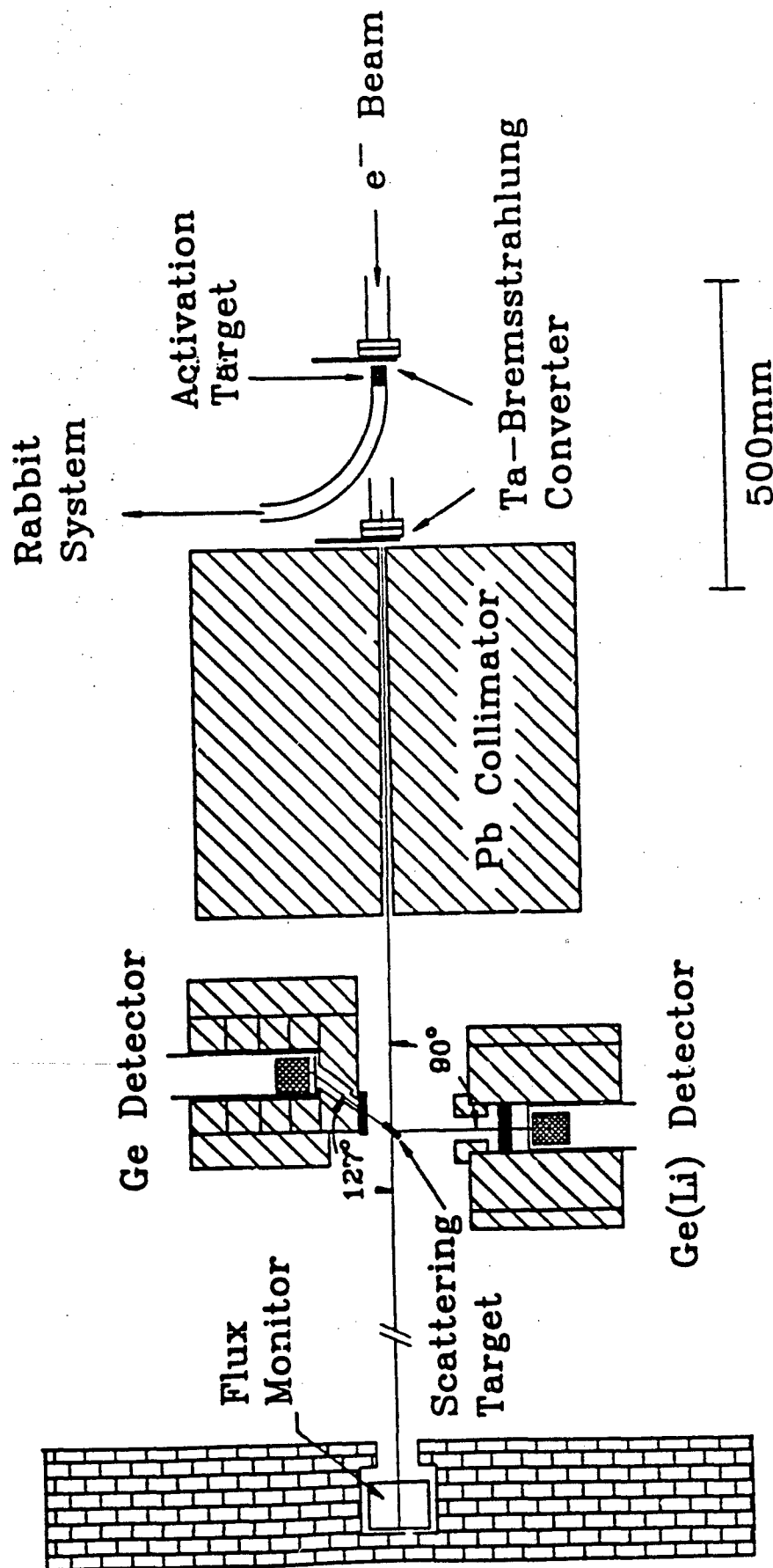


Fig. 1

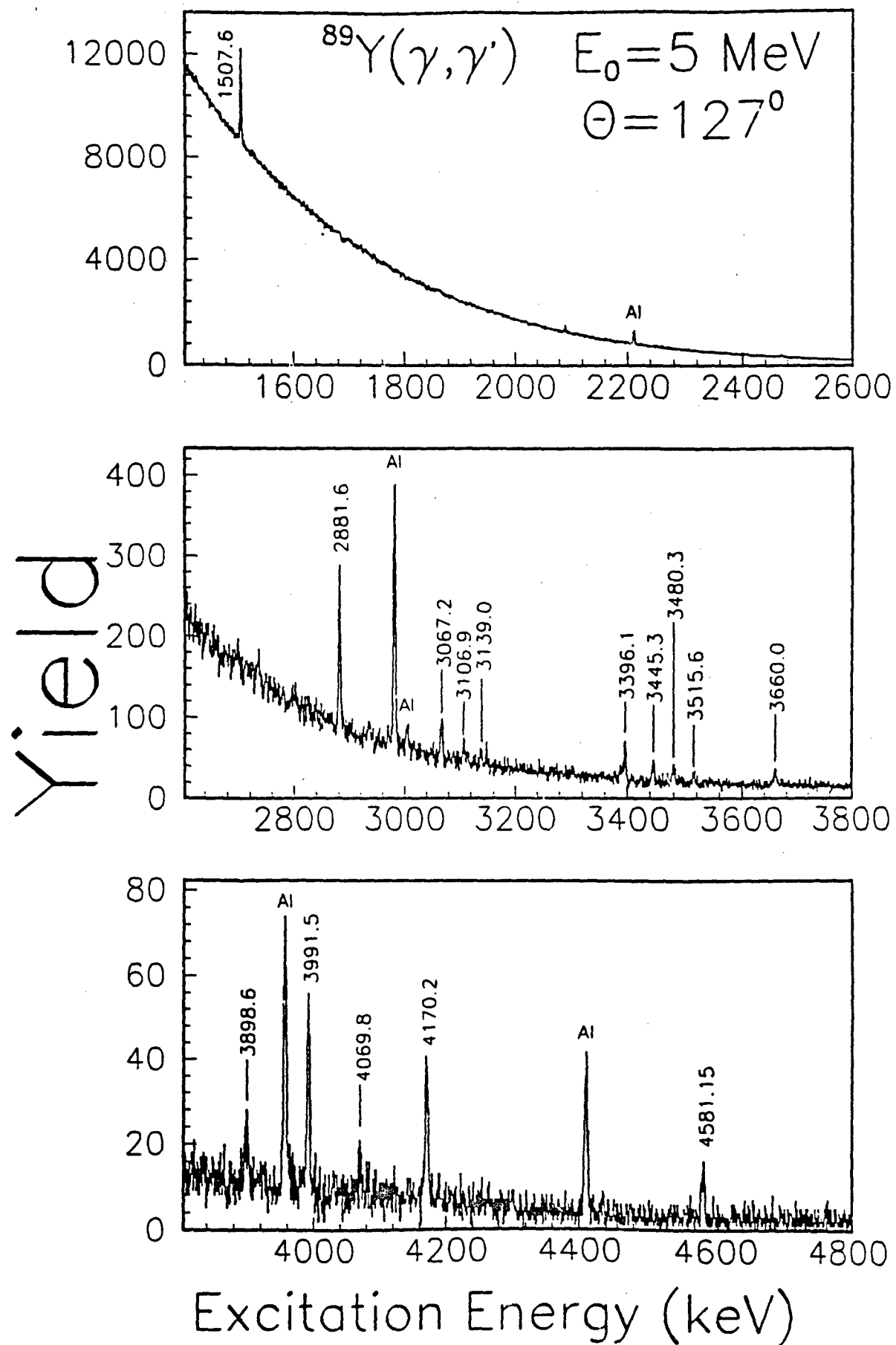


Fig. 2

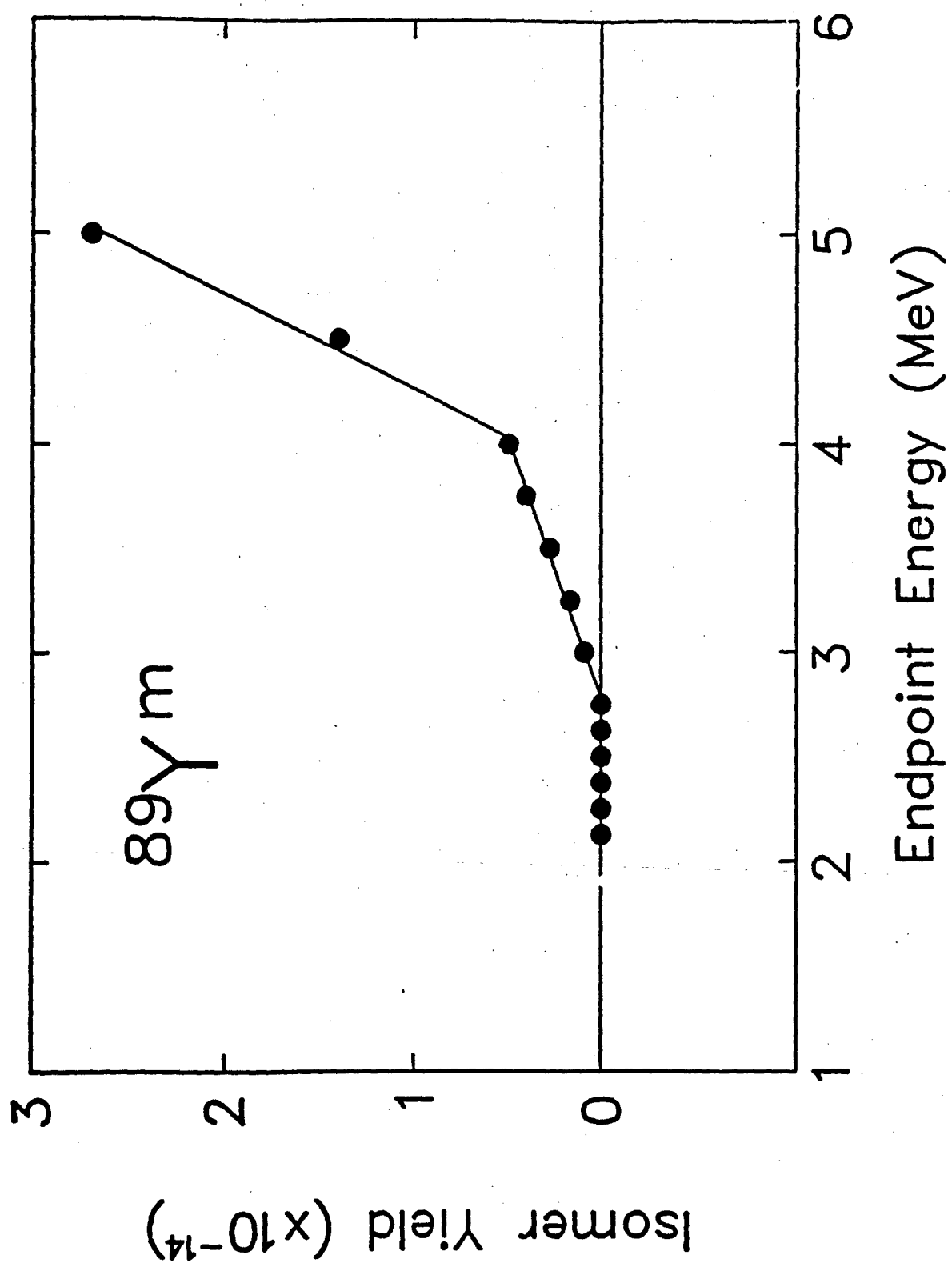


Fig. 3

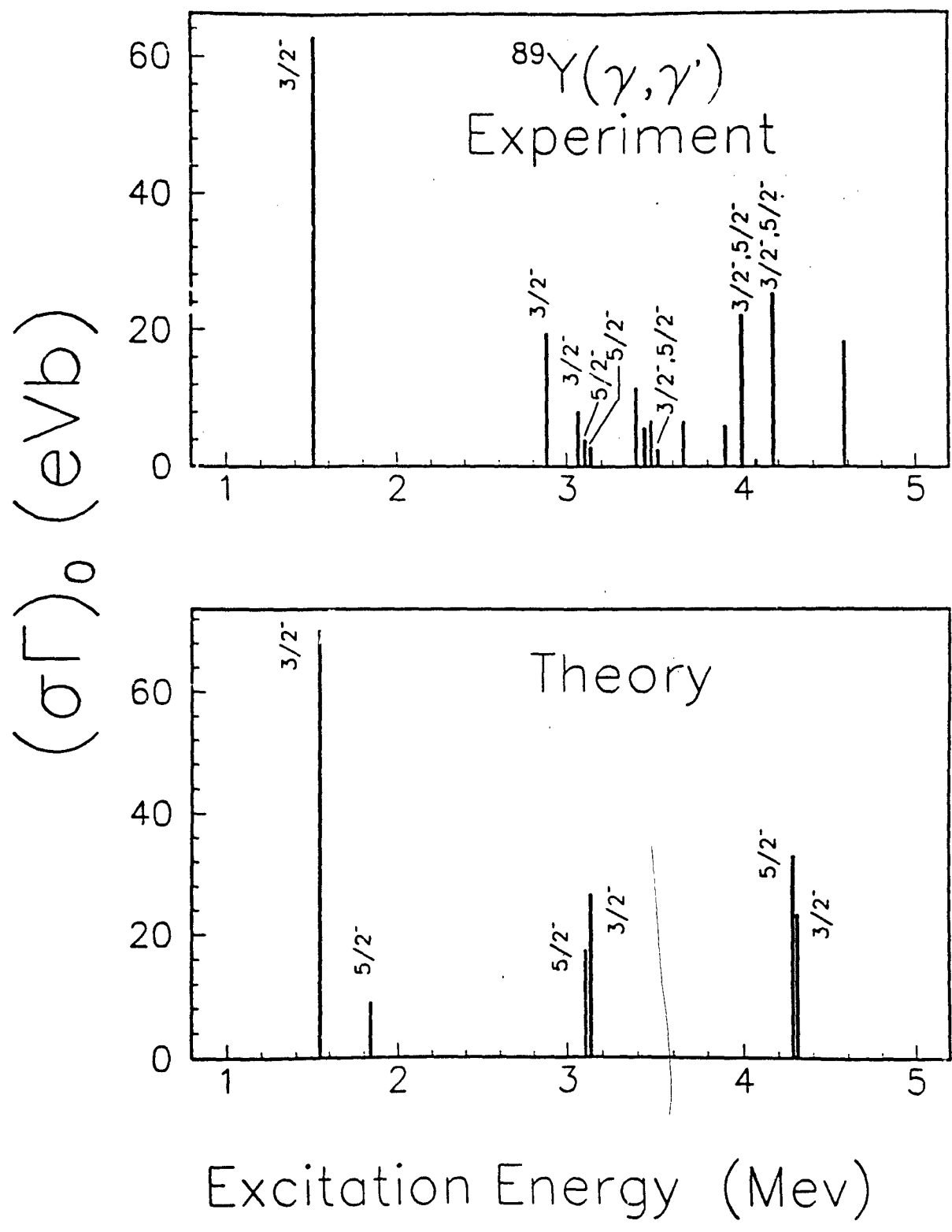


Fig. 4

**Fig. 5**

Low Energy Conversion Electron Mössbauer Spectroscopy using  
a Chevron Microchannel Plate Detector

by

T. W. Sinor, J. D. Standifird, K. N. Taylor, C. Hong,  
J. J. Carroll and C. B. Collins

Center for Quantum Electronics  
University of Texas at Dallas

P. O. Box 830688  
Richardson, TX 75083-0688  
(214) 690-2863

ABSTRACT

A detection system for conversion electron Mössbauer spectroscopy is described. A chevron microchannel plate assembly attached to a two stage electrostatic lens is used to preferentially detect electrons with energies  $\leq 15$  eV. Mössbauer spectra collected with these electrons can provide information about a variety of solid state surface phenomena.



## INTRODUCTION

Conversion electron Mössbauer spectroscopy<sup>1</sup> (CEMS) is a low noise spectroscopic technique based on the detection of conversion, Auger and secondary electrons emitted from a material as a result of the de-excitation of Mössbauer nuclei. It provides information about the environment in which these sensitive nuclei are embedded. However, the range which can be probed with the method is limited by the escape depth of the electrons in the material. If these electrons are detected with an energy selective technique, information about successively deeper layers into the absorber can be obtained. This refinement of the technique is called depth selective conversion electron Mössbauer spectroscopy<sup>2-5</sup> (DCEMS) and it exploits the energy loss of electrons as they escape from the material to probe specific regions with a resolution of about 5-10 nm thickness in iron.<sup>3</sup> It has been shown that the component with energies  $\leq 15$  eV comprises about 50% of the total signal.<sup>7-9</sup> Because the range of those electrons is so short, they can provide specific information about a variety of solid state surface phenomena and aid in the characterization of implanted layers.

Typically, high resolution electron spectrometers are required to make Mössbauer measurements using the lowest energy electrons and such devices are invariably complex and expensive.<sup>3,6</sup> In this paper we discuss the design and construction of a relatively simple spectrometer that was used to selectively and efficiently detect this low energy component. It was based upon a chevron microchannel plate (MCP) assembly with

an active diameter of 25 mm that served as the detector. A two stage electrostatic lens was used to preferentially focus and accelerate low energy electrons from the target to the electron detector. Such acceleration increased the energy of the electrons to a level more compatible with the sensitivity of the input to a microchannel plate.

The incidental detection of higher energy electrons, which escaped from deeper regions of the absorber served as a source of noise that could be reduced to negligible levels by minimizing the geometrical solid angle between the Mössbauer target and the MCP assembly. This was possible since the trajectories of the more energetic electrons were not significantly altered by the relatively weak electrostatic fields of the lens.

## EXPERIMENTAL

### Apparatus

Figure 1 shows the experimental arrangement used in these measurements. A  $^{57}\text{Co(Pd)}$  source with a nominal activity of 10 mCi, mounted on a Doppler motor external to the vacuum chamber containing the sample and electron detector, provided the 14.4 keV Mössbauer radiation. To optimize the passage of resonant  $\gamma$  rays into the target chamber a thin entrance window was constructed from titanium. It attenuated only slightly the 14.4 keV  $\gamma$  rays but efficiently filtered out a significant number of the lower energy x rays that are by products of the de-excitation process in the source. If not properly filtered these x rays could seriously degrade the performance of the detection system.

Low energy electrons emitted from the target were collected with a two stage aperture lens. The MCP, target, electrical feedthrough and the electrostatic lens were mounted as an integral unit on a six inch vacuum flange. This provided for convenient mounting and removal of the entire assembly from the vacuum chamber so that adjustment could be made to the target geometry. The angular position of the Mössbauer target with respect to the direction of the  $\gamma$  rays could be adjusted by rotating it about the vertical axis. Data were typically collected with the target at a  $45^\circ$  angle with respect to the detector axis.

The chamber was initially evacuated with an Alcatel CFF-450 turbomolecular pump (TMP) to a pressure of about  $3 \times 10^{-7}$  Torr. Vibrations from the TMP seriously degraded the resonant absorption in the absorber and could not be used to maintain the vacuum necessary to operate the chevron. To provide for vibrationless pumping, a 140 l/s Varian diode VacIon pump was used to maintain the required pressure of  $2 \times 10^{-6}$  Torr necessary to operate the MCP. It is important to note that such pumps operate by ionizing gas in a magnetically confined cold-cathode discharge. Unless proper precautions are taken neutral and charged particles, as well as hard ultraviolet radiation can escape from the VacIon pump and degrade the performance of the detector. To circumvent this problem we used a line-of-sight baffle that consisted of six successive aperture plates. This baffle was inserted between the VacIon pump and target chamber with the apertures staggered in a helical pattern.

### Lens Design

The structure and dimensions of the lens used in this work are shown in Fig. 2. The steering of the electrons was performed primarily by the potential gradients established between two annular rings mounted inside a wire cylinder. The rings had a common outer diameter of 12.7 cm and inner diameters of 2.5 and 3.2 cm, respectively. The overall length of the lens was 15 cm. With the inclusion of the endcaps on the assembly it not only served to focus and accelerate the electrons to the detector, but also served as a Faraday shield isolating the lens elements from the ground potential of the chamber walls and reduced the number of noise photoelectrons produced inside the chamber from entering the sensitive region of the detector.

The optimum potentials for the lens elements were determined using the EGN2C electron optics software package traceable to SLAC. Various electron emission configurations such as plane waves and point sources were simulated for electrons with energies  $\leq 15$  eV originating at the surface of the foil. Suitable biases were found that achieved an effective collection solid angle of  $2\pi$  steradians without putting "bright spots" on the face of the MCP. These bright spots could have caused dead time problems in the detector and localized channel deterioration. The optimum operating biases for the lens are indicated in Fig. 2 and a circuit diagram of the supporting electronics for the MCP assembly is shown in Fig. 3.

### Noise Reduction

To obtain Mössbauer spectra with large signal to noise ratios, proper collimation of the source to reduce non-resonant scattering inside the chamber was critical. Various collimator designs were used in these experiments but the one that yielded the best performance in our system was a 1.25 cm thick lead plate that had a circular aperture at its center. The aperture was tapered so that its diameter increased in the direction of propagation of the radiation. This tapering minimized the scattering from the collimator walls. With the source located at the appropriate distance in front of the aperture plate a well-defined collimation of the beam was achieved.

Radiation scattering inside the chamber was minimized by providing an exit window diametrically opposite the entrance window. This window had a diameter of 10 cm and was constructed of mylar to minimize backscattering of photons and photoelectrons. With proper collimation of the  $^{57}\text{Co}$  source, the beam size could be optimized to illuminate the target and not expand to a diameter that would impede its exit from the output window.

To further reduce scattering in the system the lens was constructed from a copper mesh which had an open area of 69% and a wire diameter of 250  $\mu\text{m}$ . Perturbations of the electric field resulting from the use of a mesh instead of a continuous sheet of metal are negligible at distances greater than the wire separation.<sup>10</sup> To increase the percentage of open area further, alternate wires were removed in the region of the lens that were

in the direct path of the input radiation.

## RESULTS

The target foil used to evaluate the effectiveness of the lens was a  $5.0 \times 5.0 \times 2 \times 10^{-4}$  cm iron foil with an enriched abundance of  $^{57}\text{Fe}$  nuclei of 93.55%. For purposes of comparison, data were collected with the electron lens operating in an "active" mode at the optimum potentials for low energy electrons and in a passive mode where there were no accelerating fields. Data collected with the lens in the focusing or active mode is shown in Fig. 4a. The total collection time for the data was 3.44 hours and the total signal counting rate was 2.47 counts per second. The data with the lens in the passive, field free mode is shown in Fig. 4b. Here the signal counting rate was 0.087 counts per second. To obtain reasonable statistics the data were collected five times longer than the corresponding data with the lens active. Operation of the lens in a passive mode helped determine the geometrical collection efficiency for the higher energy electrons. In this geometry it was concluded that the incidental detection of the higher energy electrons contributed less than 3.5% of the signal when the lens was operated in the active mode. Since the collection efficiency for higher energy electrons was defined solely by the geometrical solid angle between the target and MCP assembly this contribution to the signal counting rate could be reduced further by simply increasing the distance between the target and detector assembly.

## CONCLUSIONS

Depth selective conversion electron Mössbauer spectroscopy is a high resolution Mössbauer technique that provides a method to measure a variety of surface or depth dependent phenomena. Detection of electrons with energies  $\leq 15$  eV can provide detailed information about a variety of surface phenomena in the outermost 5 nm of a material.

In this article we have described the design of an efficient electron Mössbauer spectrometer that preferentially detects low energy electrons. It was shown that the contamination of the signal by electrons with higher energies could be minimized by choosing the appropriate geometry. Numerous computer simulations using plane-wave and point-source electron configurations showed that the electrostatic lens gave an effective solid angle of almost  $2\pi$  steradians for the signal electrons having appropriately low energies.

Although not pursued in this work, it is possible with the current design to collect virtually all the electrons emitted from the target. This could be accomplished if the potential difference between the input of the chevron and target foil is made sufficiently large. Furthermore, if a retarding field analyzer is positioned between the target and MCP the lower energy electrons can be efficiently filtered out.<sup>11</sup> In this manner it is possible to obtain energy resolved Mössbauer spectra over a wider range of electron energies.

## REFERENCES

1. For a good review see: J.A. Sawicki. Industrial Applications of the Mössbauer Effect. Ed. G.J. Long and J. G. Stevens. (Plenum Press, New York, 1986), p. 83.
2. Z. Bonchev, A. Jordanov and A. Minkova, Nucl. Instr. Methods 70, 36 (1969).
3. U. Bäverstam, T. Ekdahl, Ch. Bohm, B. Ringström, V. Stefánsson and D. Liljequist, Nucl Instr. Methods, 115, 373 (1974).
4. D. Liljequist and M. Ismail, Phys. Rev B, 31, 4131 (1985).
5. D. Liljequist and M. Ismail, Phys. Rev B, 31, 4137 (1985).
6. K. Saneyoshi, K. Bebusmann, W. Keune, R. A. Brand, and D. Liljequist in Industrial Applications of the Mössbauer Effect. Ed. G.J. Long and J. G. Stevens. (Plenum Press, New York, 1986), p. 121.
7. W. Jones, J. M. Thomas, R. K. Thorpe and M. J. Tricker, Appl. Surf. Sci 1, 388 (1978).
8. J. S. Zabinski and B. J. Tatarchuk, Nucl. Instr. Methods, 216, 501 (1983).
9. J. S. Zabinski and B. J. Tatarchuk, Nucl. Instr. Methods, B42, 379 (1989).
10. See for example, R. P. Feynman, R. B. Leighton, and M. Sands. The Feynman Lectures in Physics, Vol. II. (Addison-Wesley, Reading, Massachusetts, 1964), p. 7-10.
11. H. Sato and M. Mitsuhashi, Hyperfine Interactions 58, 2535 (1990).



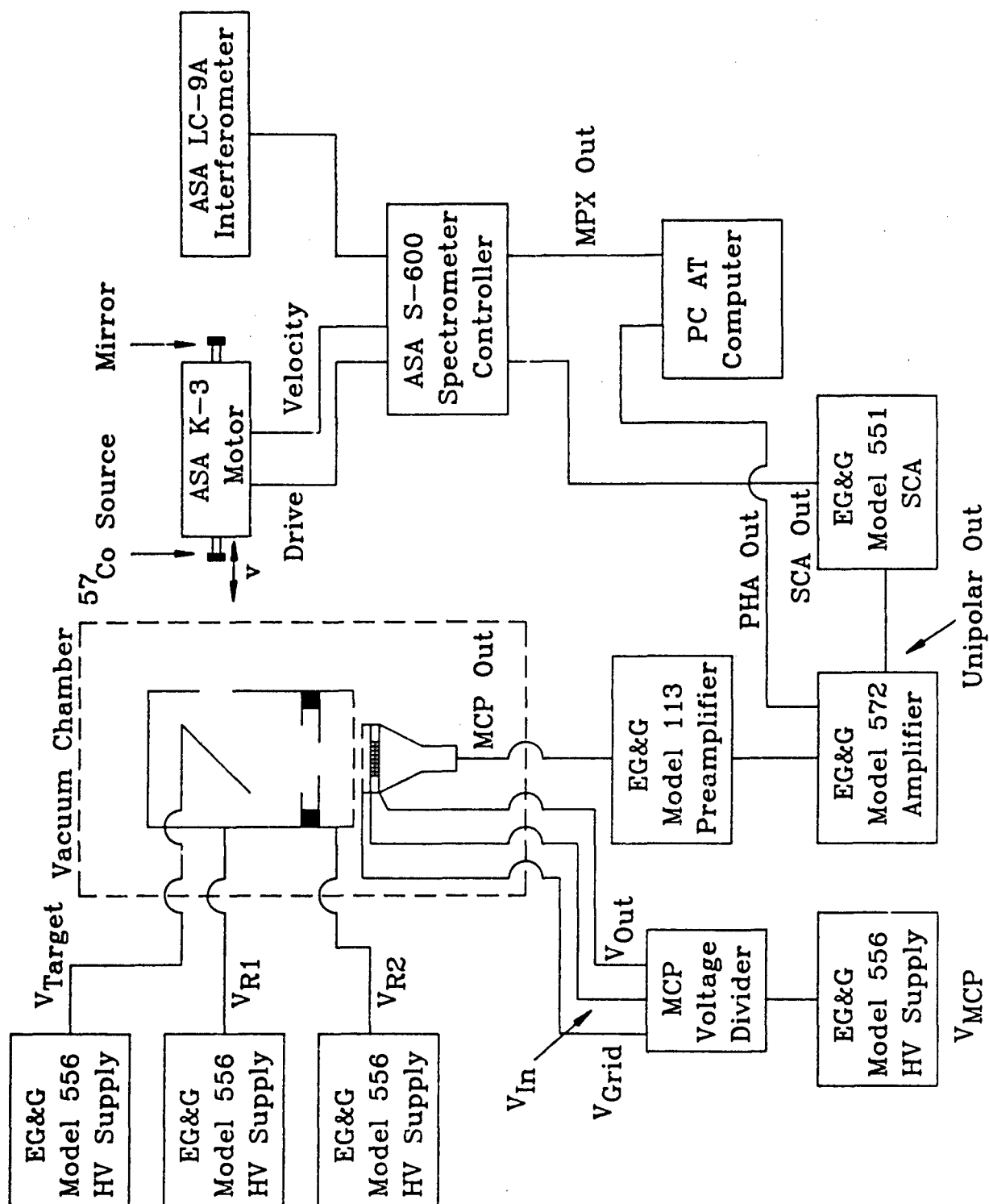
#### CAPTIONS

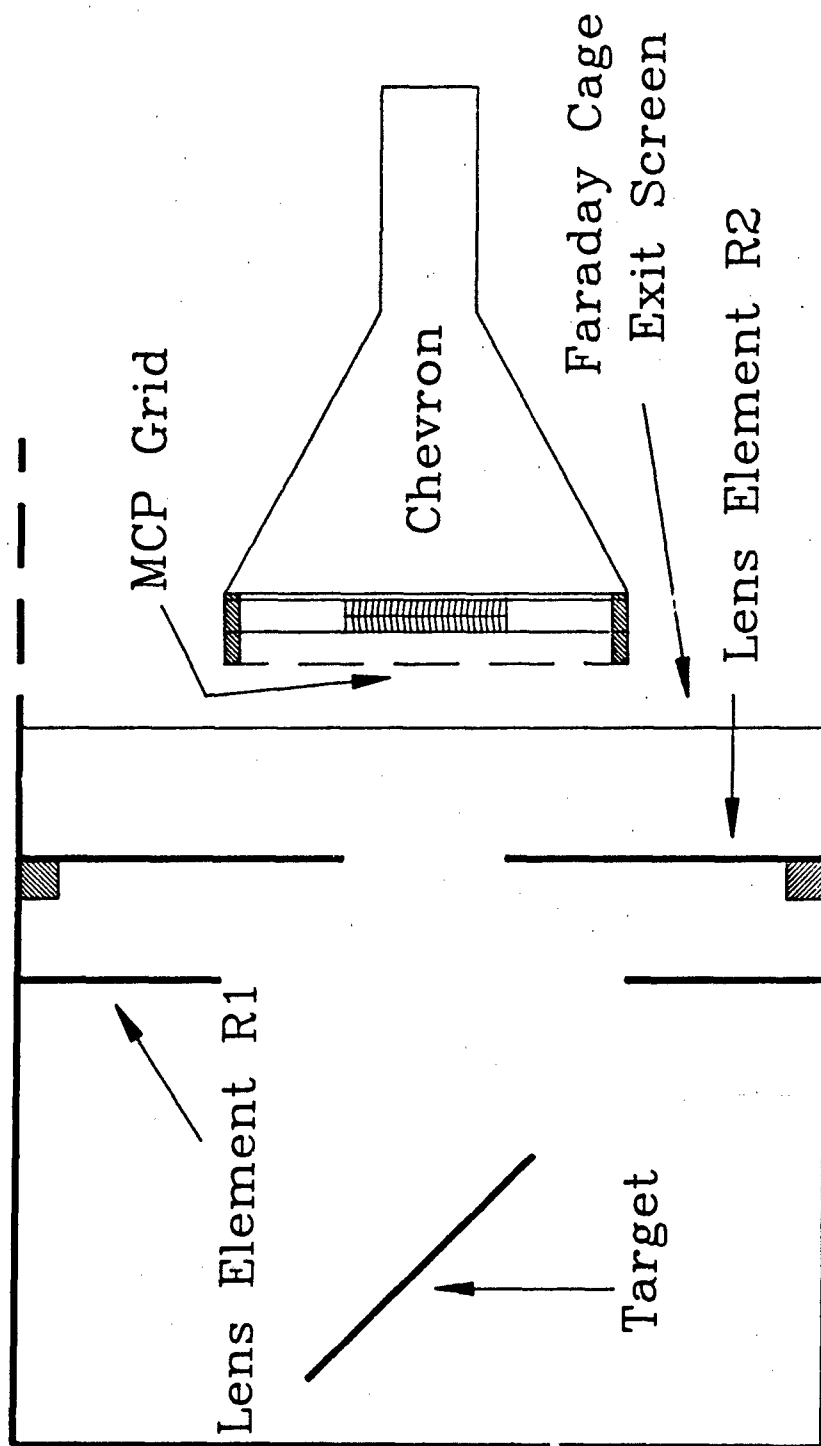
Figure 1: Block diagram of the experimental arrangement.

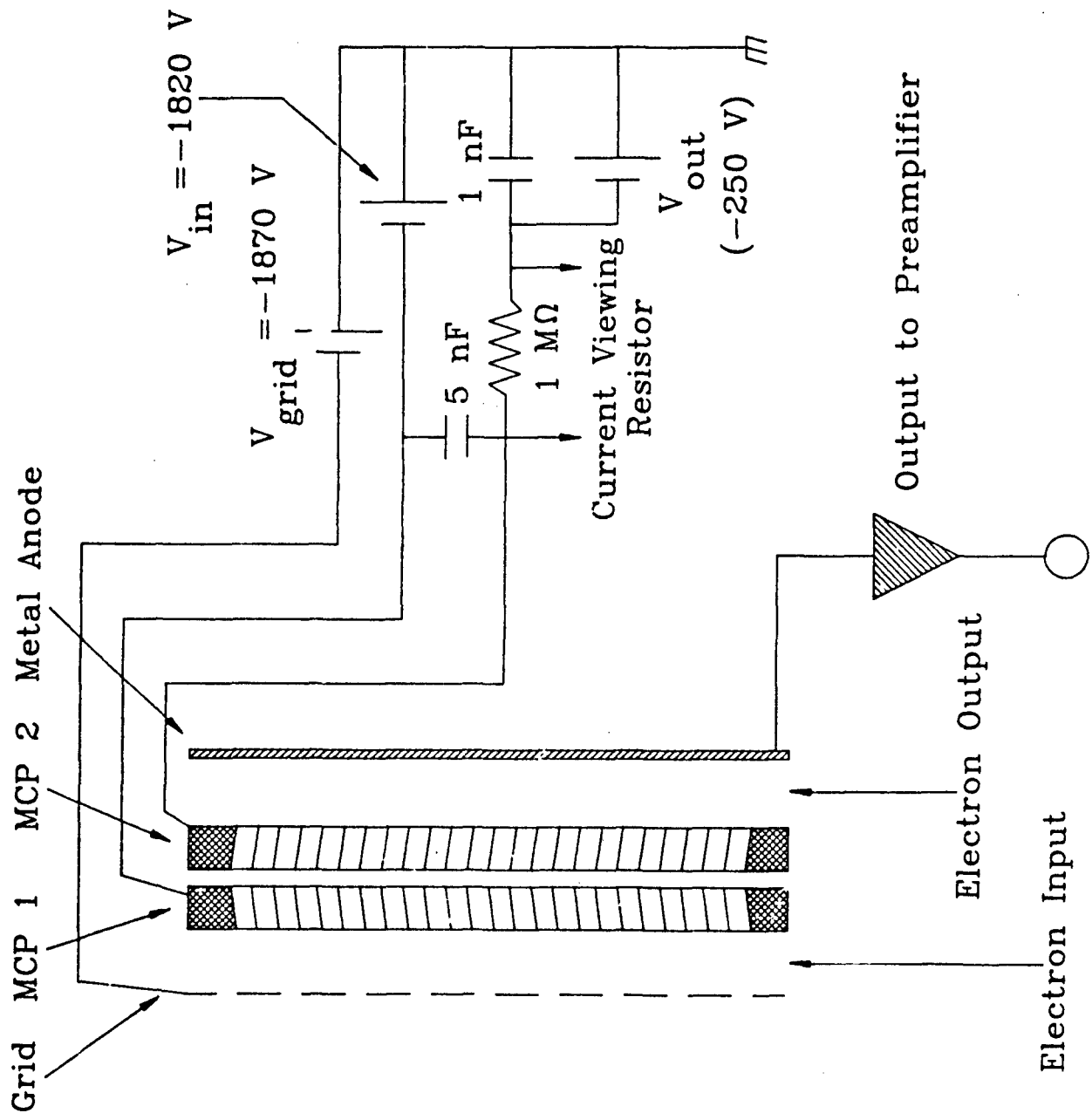
Figure 2: Drawing of the two-element electron lens designed to efficiently collect electrons having energies  $\leq 15$  eV. The steering of the electrons was performed primarily by the potential gradients established between  $R_1$  and  $R_2$ . With the inclusion of the endcaps on the assembly, the lens system not only serves to focus and accelerate electrons to the detector input plate, but also serves as a Faraday cage in shielding the lens elements from the ground potential and noise electrons of the chamber walls. The optimum operating biases for the lens were found to be  $V_{R1} = -2817$  V,  $V_{R2} = -1967$  V, and  $V_{Target} = -2757$  V when the chevron was operated at  $-1616$  V and the MCP grid at  $-1870$  V.

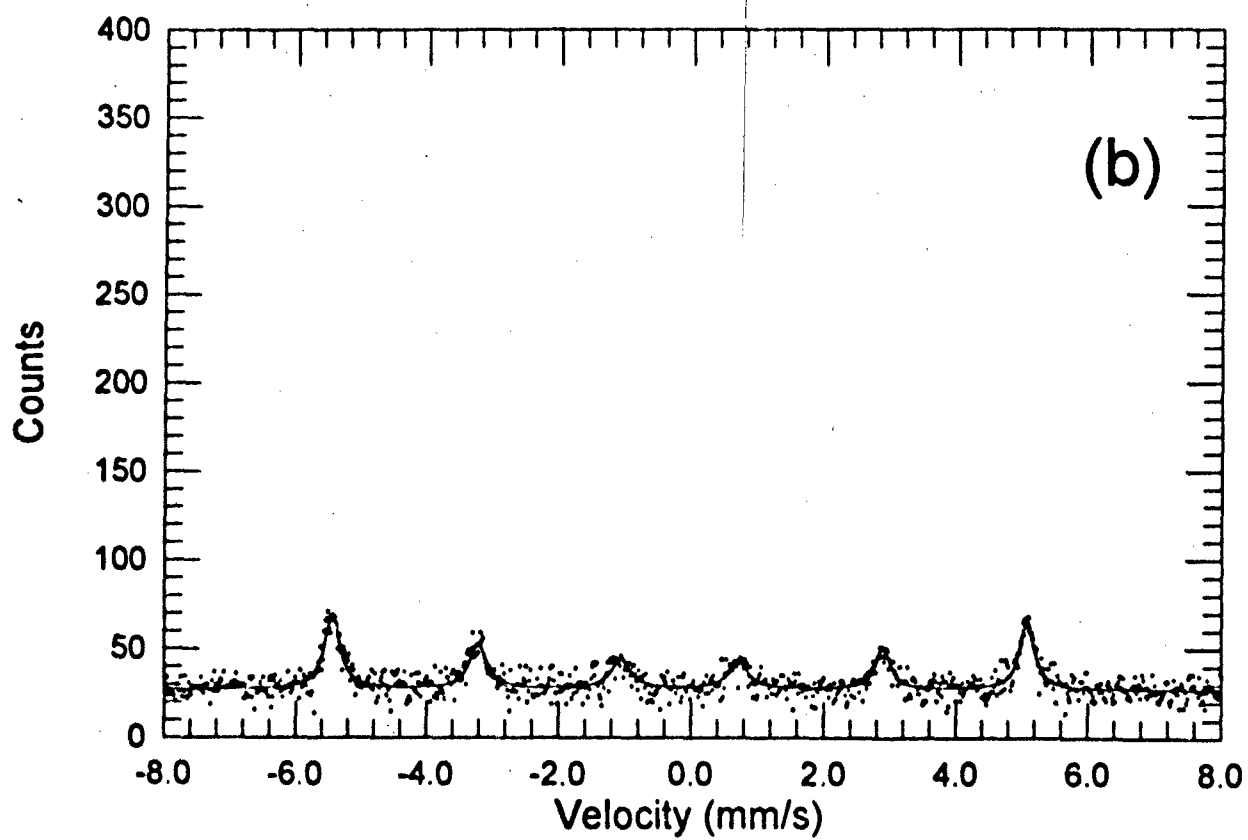
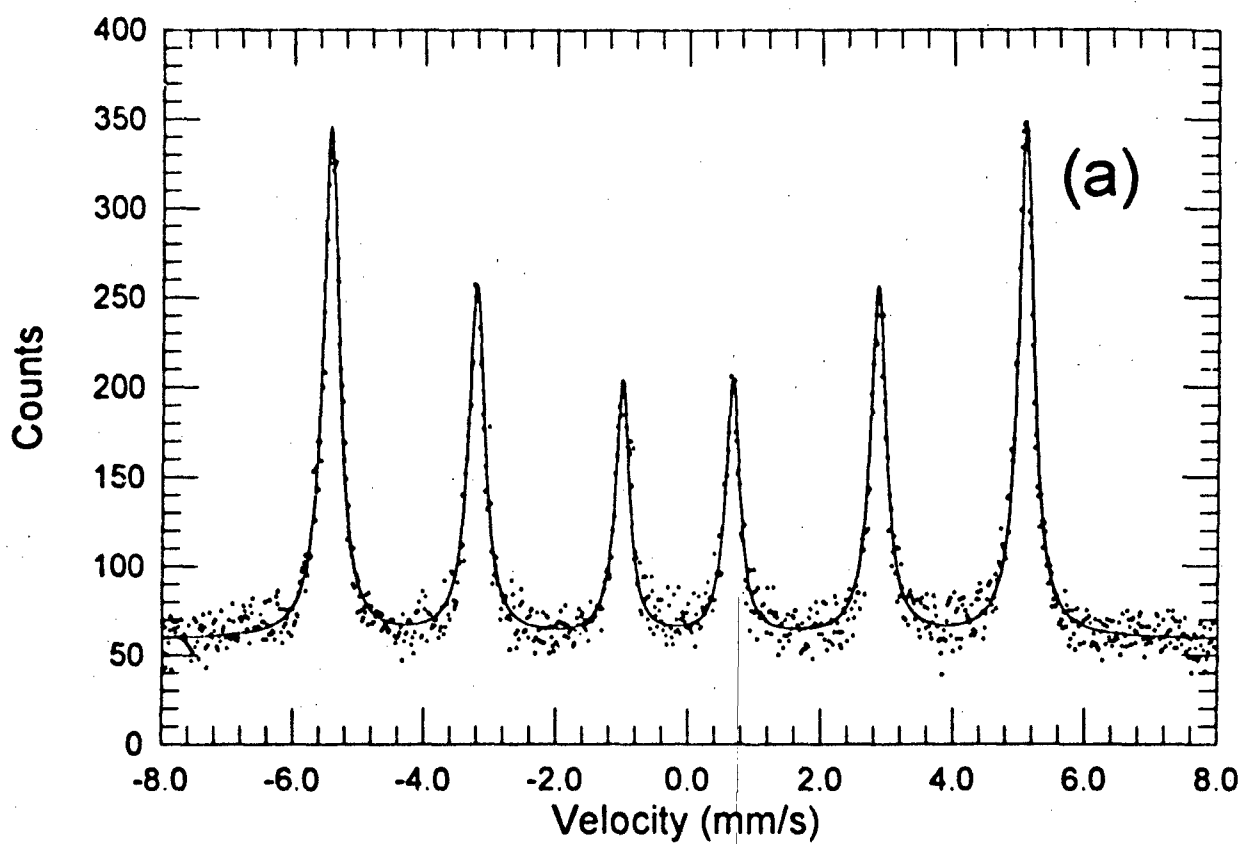
Figure 3: Circuit diagram of the supporting electronics for the Chevron microchannel plate assembly.

Figure 4: Conversion electron Mössbauer spectra for a 93.55% enriched  $^{57}\text{Fe}$  target: (a) Lens in a focusing or active mode collected for 3.4 hours and the counting rate was 2.47 cps. (b) With the lens in a passive, field free mode possessing with no focusing or accelerating properties the signal counting rate dropped to 0.087 cps. To obtain reasonable statistics the data had to be collect five times longer than in (a). The geometrical collection of higher energy electrons account for less than 3.5% of the signal when the lens is operated at optimum biases.









**END  
FILMED**

DATE:

4-93

**DTIC**